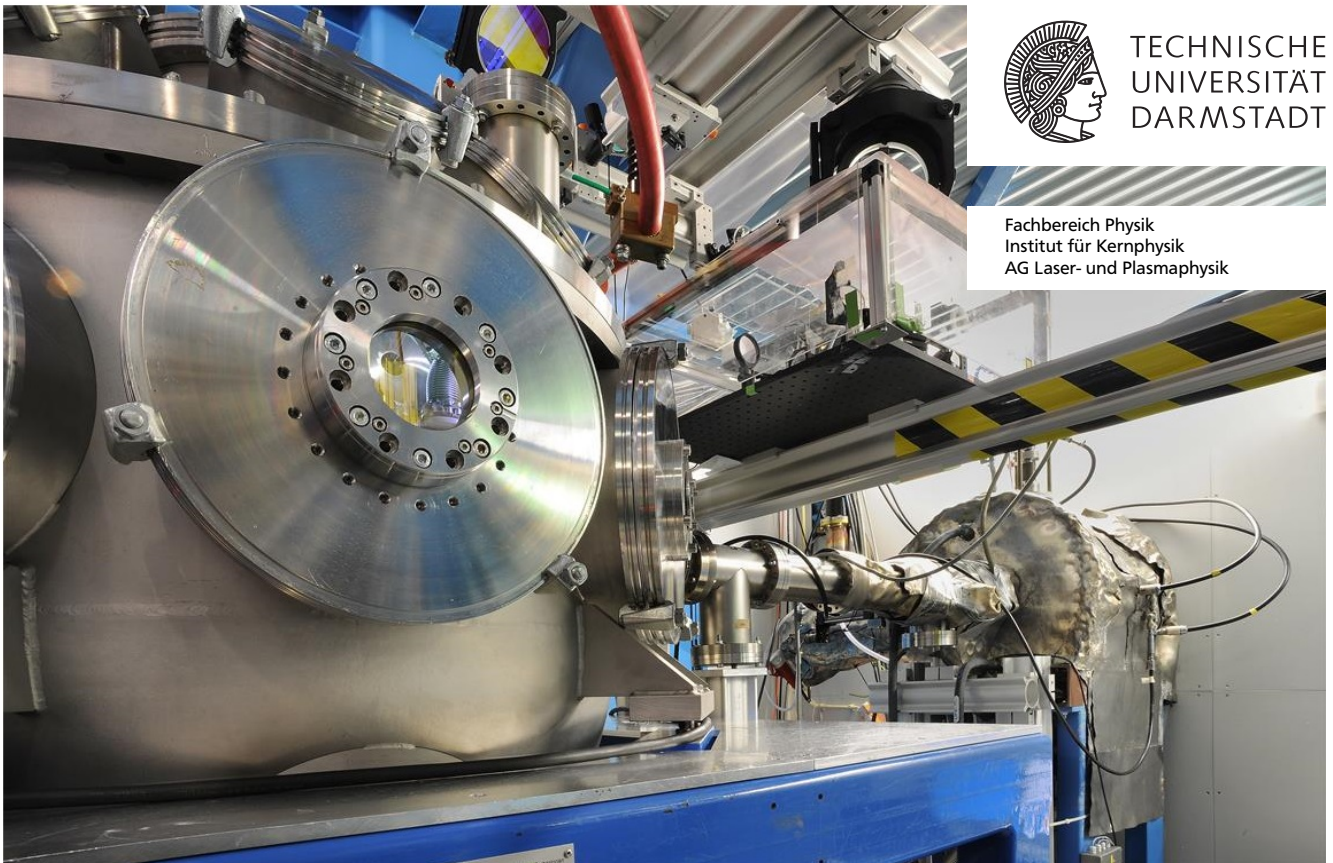

Construction and characterization of a laser-driven proton beamline at GSI

Aufbau und Charakterisierung einer lasergetriebenen Protonenstrahlführung bei GSI

Zur Erlangung des Grades eines Doktors der Naturwissenschaften (Dr. rer. nat.)

genehmigte Dissertation von M. Sc. Simon Busold aus Fulda

Mai 2014 – Darmstadt – D 17



TECHNISCHE
UNIVERSITÄT
DARMSTADT

Fachbereich Physik
Institut für Kernphysik
AG Laser- und Plasmaphysik

Construction and characterization of a laser-driven proton beamline at GSI
Aufbau und Charakterisierung einer lasergetriebenen Protonenstrahlführung bei GSI

Genehmigte Dissertation von M. Sc. Simon Busold aus Fulda

1. Gutachten: Prof. Dr. Markus Roth
2. Gutachten: Prof. Dr. Oliver Boine-Frankenheim

Tag der Einreichung: 07.02.2014

Tag der Prüfung: 16.04.2014

Darmstadt – D 17

The cover picture shows the present laser-based proton beamline at the Z6 experimental area at GSI (on the left is the Z6 target chamber). The PHELIX 100 TW laser beam enters the chamber from left, hits a thin foil target at the center of the target chamber and drives the proton acceleration via the TNSA mechanism. A pulsed solenoid for beam capture is placed close to the target within the chamber and transports the bunch through the drift tube to the buncher cavity (at the right end of the picture). At this position, the beamline leaves the Z6 area and enters the neighboring Z4 area. Beam diagnostic possibilities are at several stages of the beamline; the most important places for beam probing are inside the target chamber close behind the target for source characterization and at the current end of the beamline behind the cavity.



Contents

1	Introduction	3
1.1	Introduction to laser-driven ion acceleration and its applications	3
1.2	The LIGHT project	5
1.3	Thesis structure	7
2	The laser-driven proton source	9
2.1	Relativistic laser matter interaction and electron acceleration	9
2.2	The target normal sheath acceleration mechanism - TNSA	15
2.3	Diagnostics for laser accelerated ion beams	19
2.4	The PHELIX 100 TW beamline	23
2.5	Proton beam parameters at the Z6 experimental area	25
3	Beam transport and energy selection	29
3.1	Linear beam optics	29
3.2	Charged particles in a solenoid field	32
3.3	Characterization of the pulsed high-field solenoid	34
3.4	Experimental campaign with the solenoid	38
3.5	Discussion of the results	42
3.6	Measuring the co-moving electrons	47
4	Phase rotation and energy compression	55
4.1	Radiofrequency structures for accelerators	55
4.2	Implementing the radiofrequency cavity into the setup	57
4.3	Experimental setup and comparative beam parameters	59
4.4	Synchronization of laser and cavity	62
4.5	Experimental results on energy compression	67
5	Perspectives for the LIGHT beamline	75
5.1	Optimization of the source	75
5.2	Alternatives for beam transport and energy selection	76
5.3	Towards highest intensities	79
5.4	A unique experimental area at GSI	80
6	Conclusion	83
I	References	i
II	Publications	xi
III	Acknowledgments	xiii



1 Introduction

Since their first discovery in 1960 [Maiman, 1960], lasers evolved rapidly and are nowadays widely and essentially used in many areas of human civilization like science, technology, communication and medicine. This broad field of applications consequently results in very different types of lasers. One laser parameter that has been pushed to higher and higher values, is the accessible laser intensity. In the advance towards highest laser intensities, the electro-magnetic fields within the laser field at some point achieved values high enough to open up a novel field of applications for lasers: efficient direct and indirect particle acceleration.

The thesis at hand is settled within this new field, more precisely the laser-based acceleration of ions (typically protons), to which a brief historical introduction will be presented in the following.

1.1 Introduction to laser-driven ion acceleration and its applications

At the beginning of the 1960s, the achievable laser intensity increased rapidly due to technological advances like Q-switching [McClung and Hellwarth, 1962] and mode-locking [Hargrove et al., 1964], which soon enabled field strengths strong enough for field ionization. The next key innovation towards higher intensities followed in the mid 1980s with the introduction of the CPA technique (Chirped Pulse Amplification, [Strickland and Mourou, 1985]) and the access of laser intensities above 10^{18} W/cm². At this level, the movement of the electrons in the laser field becomes relativistic and a new area of physics could be accessed.

While already earlier laser-driven particle sources based on random plasma expansion had been proposed [Gitomer et al., 1986], accessing the relativistic laser intensities opened up completely new possibilities in the laser matter interaction. In experiments, performed in the late 1990s at petawatt-class lasers, directed, high-intensity proton bunches were observed when focusing the laser on a μ m thin flat foil. And in contrast to the earlier random plasma expansion experiments, also high particle energies of 10s of MeV were measured [Snively et al., 2000, Hatchett et al., 2000, Clark et al., 2000, Maksimchuk et al., 2000]. As driving force of the ion acceleration, a relativistic electron distribution was soon identified, which is created by the interaction of the intense laser pulse with the target. These ions originate (dominantly) from the target rear side [Fuchs et al., 2005, Fuchs et al., 2007], where the expanding electrons form a sheath and thereby the accelerating field, which is directed normal to the target surface. Therefore, the acceleration mechanism was named *target normal sheath acceleration* (TNSA, [Wilks et al., 2001]). The experimental observations triggered extensive research on the topic all around the world and significantly contributed to the quickly evolving novel field of laser-driven particle acceleration.

This new ion source proved to have excellent beam properties [Cowan et al., 2004, Roth et al., 2005, Ruhl et al., 2006] due to microscopic source size and high laminarity, while additionally providing large (single bunch) particle numbers and multi-MeV energies; $>10^{13}$ particles per bunch and energies exceeding 58 MeV have been measured for protons [Snively et al., 2000]. The efficient acceleration of heavier ions is only possible in combination with special target preparation techniques to clean the target surface from the else dominant protons, e.g. laser desorption [Flippo et al., 2006] or heating of the target [Hegelich et al., 2002, Hegelich et al., 2006], resulting in successful acceleration of mid-Z ions (carbon, oxygen, fluorine).

Theoretical models to describe the acceleration process [Mora, 2003, Passoni and Lontano, 2004, Schreiber, 2006] helped in the understanding of the underlying physics. The different models are based on different basic assumptions and a comparative study of several models can be found in [Perego et al., 2011]. The analytical models are continuously improved and many details of the complex laser matter interaction are still subject to active research.

Since their first discovery, many possible applications have been discussed for this compact source of high intensity ion beams. An overview of the main areas of proposed or already in-use applications is itemized in the following. More details may be found in recent reviews, e.g. [Daido et al., 2012].

- The high particle numbers in the MeV energy region and the short time scales (ps) enable energy deposition in secondary targets fast and powerful enough to access the physically interesting state of *warm dense matter* (WDM) via isochoric heating. Creation of such WDM states by TNSA ion beams was done in several experiments [Patel et al., 2003, Snavely et al., 2007, Dyer et al., 2008, Pelka et al., 2010] and presents an established technique nowadays.
- Due to their excellent beam quality, laser-based ion acceleration can also be used as unique diagnostic tool. Ultra-short, time-resolved proton imaging precisely resolves the evolution of strong electro-magnetic fields and particle densities [Mackinnon et al., 2004, Borghesi et al., 2001, Mackinnon et al., 2006] on time scales between picoseconds and nanoseconds. Profiting from the continuous energy spectrum, several time steps at picosecond time resolution can be recorded within one experiment.
- A specialized application has been proposed in the context of the inertial confinement fusion research. An intense particle beam can be used as a fast ignitor, reducing the requirements on fuel compression. The use of laser-accelerated protons is a promising option in this scenario [Roth et al., 2001].
- As an alternative to using the ion beam from the laser-based source directly, its key characteristics (initially short bunch duration and high particle numbers) can be transferred to a secondary beam, too. With the help of e.g. close (p,n) converter targets, a pulsed neutron source is possible [Karsch et al., 2003, Ellison and Fuchs, 2010] and neutron beams of highest brightness can be produced [Roth et al., 2013, Jung et al., 2013].
- A general advantage of the laser-based acceleration technique is its compactness and the accessibility of the necessary laser systems. This, e.g., enables the possibility for else uneconomic on-site production of isotopes [Nemoto et al., 2001, Ledingham et al., 2004].
- Such a compact source would be favored in many other scenarios, too, as it may reduce size, cost and the radiation sensitive area of the accelerator. The prospect of applications in medicine (like cancer therapy) has drawn much attention [Metzkes et al., 2011, Hofmann et al., 2012] (and references therein). However, one should mention that this is still critically discussed within the community [Linz and Alonso, 2007], as the currently achievable parameters are still far off the requirements for applications like this.

Lots of those applications can accept the initial beam properties from such a laser-based source; some even rely on it (like the ultra-fast proton imaging). But others cannot accept the huge energy spread

(continuous exponential particle spectrum) of the accelerated ions, their large initial divergence (up to 30° half envelope divergence angle) or the environment of the intense laser matter interaction in general (e.g. the occurring EMP and the X-ray flash). Often the application of an ion beam is located away from the source, thus collimation and transport of the beam is essential. Much effort was taken in dealing with these matters. Beam manipulation from target [Patel et al., 2003, Bartal et al., 2012] only improved the situation on microscopic scale and plasma-based microlenses [Toncian et al., 2006] suffered from poor efficiency and a complex setup including a second short pulse laser. Most promising results could be obtained with conventional magnetic focusing devices like solenoids [Harres et al., 2010, Burris-Mog et al., 2011] and quadrupoles [Schollmeier et al., 2008, Nishiuchi et al., 2009]. Due to their chromatic focusing, they provide for not only collimation but intrinsic energy selection as well, as particles with different energies are focused at different positions and are efficiently filtered by an acceptance of the beamline which is matched to one specific energy. Further energy compression is still necessary as well as a detailed beam characterization, to be able to use conventional beam transport systems for guiding the ions to their applications.

One possibility to further reduce the energy spread of the bunch is by using a radiofrequency (rf) buncher cavity. The first successful demonstration of such an integrated beamline to merge a novel laser source with conventional accelerator technology was accomplished by a Japanese group [Nishiuchi et al., 2009, Ikegami et al., 2009]. They were able to produce proton bunches from a TNSA source with energies up to 2.2 MeV and succeeded in shaping narrow bunches of 5% energy spread by energy selection and compression via a radiofrequency cavity (and optional quadrupole focusing for enhancing the capture efficiency). Their beamline worked at a repetition rate of 1 Hz, but could only deliver medium intensity bunches with particle numbers of 5×10^6 per single bunch.

Other groups around the world show increasing interest in the topic of specially adapted beam guiding systems for laser-driven ion sources as well [Sinigardi et al., 2013, Teng et al., 2013]. In Germany, the LIGHT collaboration was formed for this reason. The collaboration and its goals are introduced in the following.

1.2 The LIGHT project

LIGHT (**L**aser **I**on **G**eneration, **H**andling and **T**ransport) is a collaboration of several German university institutes and Helmholtz centers [Busold et al., 2014a]. Its primary goal is to build and operate a versatile testbed for connecting a novel laser-based ion source to a conventional accelerator structure. As ideal location the GSI Helmholtz center for heavy ion research (GSI) was chosen because of the unique experimental conditions: having the petawatt-class high-intensity laser PHELIX [Bagnoud et al., 2010] available as well as the existing rf infrastructure of the large conventional accelerator facility GSI and with the manifold future perspectives with the FAIR facility currently built on-site. The proposed, constructed and commissioned demonstration beamline currently consists of a TNSA proton source driven by PHELIX, a pulsed solenoid for collimation and energy-selection and a rf cavity for phase rotation, as well as multifold diagnostic possibilities.

The collaborators from Technical University of Darmstadt (TUD), GSI Helmholtz center for heavy ion research (GSI), Helmholtz-center Dresden - Rossendorf (HZDR), Johann Wolfgang Goethe University Frankfurt (JWGU), and Helmholtz Institute Jena (HIJ) cover all necessary expertise in the physics of

lasers, plasmas, accelerators and pulsed high-field magnet technology. The LIGHT beamline is located at the Z6 experimental area at GSI, which does not only include the availability of the PHELIX laser and the necessary rf power, but also beamlines of the GSI's universal linear accelerator (UNILAC), the high energy laser *nhelix* [Schaumann et al., 2005] and multiple diagnostic possibilities, which all together make for a versatile experimental area (see figure 1.1).

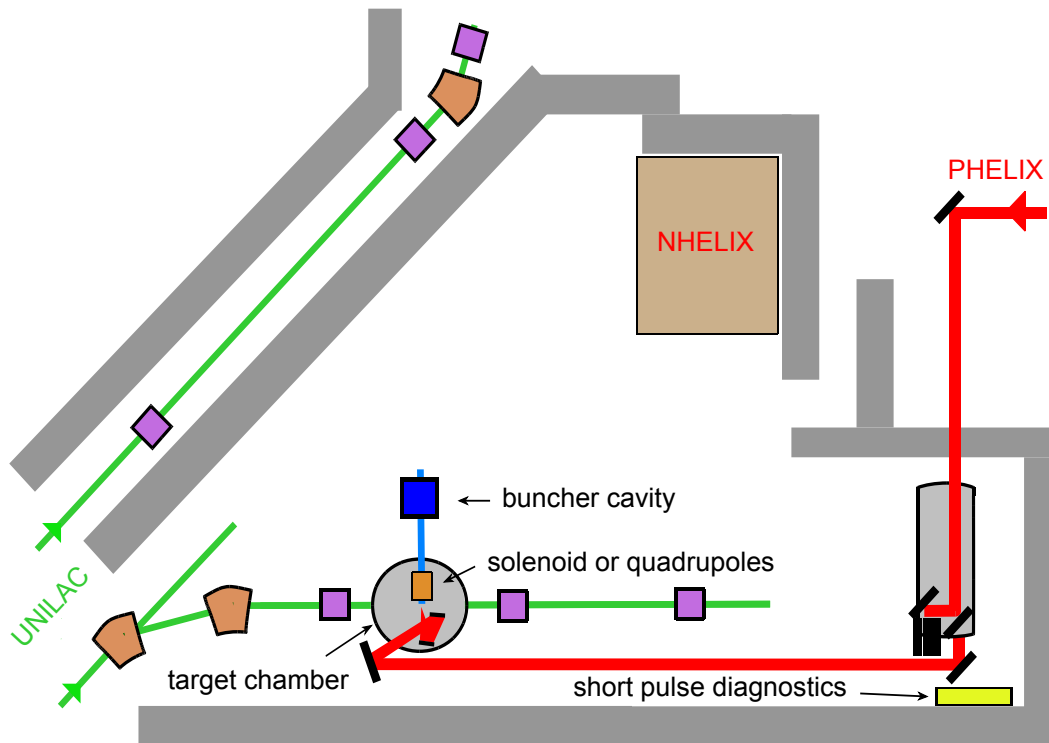


Figure 1.1: Overview of the Z6 experimental area, where the LIGHT beamline (blue) is located. Along with the PHELIX laser (red), also several UNILAC beamlines (green) and the *nhelix* laser are available for experiments.

For this beamline, it is proposed to create a collimated 10 MeV proton bunch of nanoseconds bunch length containing 10^{10} particles with an energy spread of less than 3%. The experimental studies, that can be performed at this beamline, will contribute to expand the usage of laser-driven particle sources. Major applications directly aimed for are

- the investigation of highest proton bunch intensities at MeV level,
- the conceptual study to provide an additional compact ion beamline for plasma physics experiments at FAIR¹, and
- the investigation of laser-driven ion sources as an alternative to conventional accelerators for special applications.

The experimental work is accompanied by simulation studies which cover all individual steps from source [Lecz et al., 2013] to possible injection and post-acceleration [Almmani et al., 2012]. Fur-

¹ A LIGHT-like beamline is proposed for diagnostic reasons at the APPA cave at FAIR by the HEDgeHOB collaboration, <http://hedgehob.physik.tu-darmstadt.de/>.

thermore, the collaboration investigates the optimization of laser parameters [Wagner et al., 2013, Brabetz et al., 2012], the accessing of higher particle energies via other acceleration mechanisms and the acceleration of heavier ions [Hoffmeister et al., 2013].

Within this project, the thesis at hand covers the commissioning of the dedicated experimental beamline at GSI and the first experiments on phase rotation with the rf field. Therefore, the beam transport section has been optimized, additional detection methods developed and applied to be able to fully characterize the proton bunch within the beamline, as well as accompanying simulation studies performed and compared to the experimental results.

1.3 Thesis structure

After embedding the thesis into the scientific context (this chapter 1) the description of the utilized laser-driven proton source follows in chapter 2. The necessary capture, transport and energy selection of protons from this source is achieved in the main experiments by applying a pulsed solenoid. In chapter 3 the technique of the chromatic focusing is introduced and a full experimental characterization provided. The final step of compressing the proton bunch's energy is the focus of chapter 4, thus completing the current setup of the LIGHT beamline and presenting accessible beam parameters.

Chapter 5 gives an overview of the optimization possibilities at each step of the beamline (1. source, 2. transport and energy selection, 3. phase rotation) and includes first experimental results with a permanent magnetic quadrupole doublet as alternative to the pulsed solenoid system.

Finally the achievements, that could be obtained in the scope of this thesis, are summarized in chapter 6.

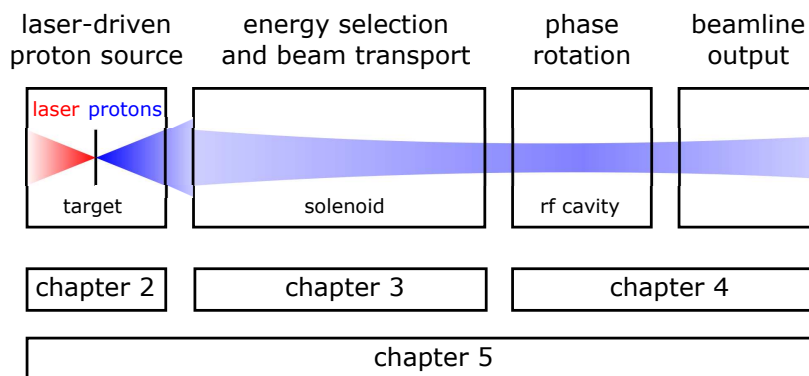
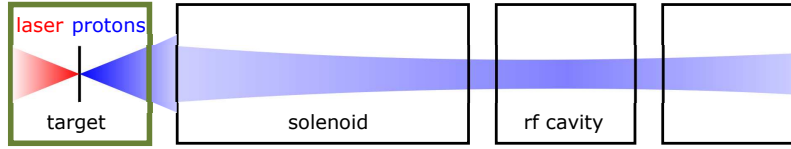


Figure 1.2: The structure of this thesis. After this introduction, the following chapters cover each one step of the beamline (2: source, 3: transport, 4: phase rotation). Chapter 5 then gives an overview of optimization and upgrade possibilities for every stage and finally the results of this work are summarized in chapter 6 (not indicated above).





2 The laser-driven proton source

In this chapter the laser-driven proton source is introduced. In the first two sections the process of laser-based ion acceleration is described, starting with the underlying relativistic laser matter interaction and fast electron acceleration, and focusing on the ion acceleration mechanism which is used in the experiments of this thesis, the *target normal sheath acceleration*. These sections serve as a general theoretical introduction to the topic. A more detailed description can be found in specialized books like [Gibbon, 2005, Schollmeier, 2008, Mulser and Bauer, 2010, Macchi, 2013]. Formulas and numbers that are not explicitly cited are taken from one of these references.

2.1 Relativistic laser matter interaction and electron acceleration

Although typically referred to as *laser-accelerated ions*, ions cannot efficiently be accelerated with today's lasers because of their high mass. Therefore, when speaking of *laser ion acceleration* (or more precisely *laser-driven ion acceleration*), always a two-stage acceleration process is implied, starting with electrons being accelerated by the laser and those energetic electrons then driving the ion acceleration via charge separation. Consequently, this theoretical introduction also starts with the laser electron interaction and the resulting electron distribution when a high-intensity laser pulse interacts with an overdense target.

2.1.1 Single electron interaction

The motion of an electron in the electro-magnetic fields \mathbf{E} and \mathbf{B} of a laser is described by the Lorentz equation,

$$\frac{d\mathbf{p}}{dt} = -e(\mathbf{E} + \mathbf{v} \times \mathbf{B}), \quad (2.1)$$

together with the energy equation

$$\frac{d}{dt} (\gamma m_e c^2) = -e(\mathbf{v} \cdot \mathbf{E}), \quad (2.2)$$

with $\mathbf{p} = \gamma m_e \mathbf{v}$ and $\gamma = (1 - v^2/c^2)^{1/2}$ the relativistic factor (and e : electron charge, m_e : electron rest mass, c : speed of light, \mathbf{p} : relativistic impulse vector, \mathbf{v} : velocity vector).

The laser, for simplicity assumed as a linear polarized electro-magnetic plane wave with the perpendicular and transverse fields \mathbf{E} and \mathbf{B} , is described below for the propagation direction z by:

$$\mathbf{E}(x, y, z, t) = E_0(t) e^{i(\omega_L t - kz)} \mathbf{e}_x \quad (2.3)$$

$$\mathbf{B}(x, y, z, t) = B_0(t)e^{i(\omega_L t - kz)}\mathbf{e}_y \quad (2.4)$$

with E_0 and B_0 the field amplitudes, ω_L the laser (angular) frequency and k the wave number. In the non-relativistic case ($v \ll c$) the \mathbf{B} field is neglected and the electron just oscillates transversely due to the electric field amplitude and the laser frequency ω_L . The oscillation velocity v_{osc} is given by:

$$v_{osc} = \frac{eE_0}{m_e \omega_L} \quad (2.5)$$

After the laser pulse passed the electron, it is again at rest at its initial position. With increasing field amplitude the velocity v_{osc} eventually approaches c and at E_0 in the order of 10^{12} V/m relativistic effects cannot be neglected further on, i.e. the magnetic field is not neglectible anymore. For practical reasons, other quantities than the electrical field ampilitude have been established to distinguish the relativistic and the non-relativistic cases. From the experimentalist's point of view, referring to the laser intensity I_0 is common, as it depends directly on the routinely measured values of the laser energy, the laser pulse duration and the focal spot size. A relation between laser intensity and electrical field amplitude is given by

$$E_0 = \sqrt{2I_0/\epsilon_0 c} \quad (2.6)$$

with ϵ_0 the electric constant. This reveals the limit for entering the relativistic regime at a laser intensity of $I_0 \approx 10^{18}$ W/cm². Another convenient quantity is the dimensionless electric field amplitude a_0 which indicates relativistic laser-electron interactions at values of $a_0 > 1$. It is defined as the relation between the parallel and the transverse component of the Lorentz force and can also be expressed via the laser intensity I_0 and the laser wavelength λ_L :

$$a_0 := \frac{eE_0}{m_e \omega_L c} = \sqrt{\frac{I_0 [W/cm^2] \lambda_L^2 [\mu m^2]}{1.37 \times 10^{18} W/cm^2 \mu m^2}} \quad (2.7)$$

Tracking an electron in such a relativistic case with $a_0 > 1$, additional to the transverse oscillation a notable longitudinal motion in laser propagation direction appears, due to the magnetic field component. The drift velocity \mathbf{v}_{drift} can be expressed as:

$$\mathbf{v}_{drift} = \frac{a_0^2}{4 + a_0^2} c \mathbf{e}_z \quad (2.8)$$

Still, as long as a plain wave is assumed for the laser pulse, no net energy gain is observed for the electron. It changes its position due to the drift motion, but is again at rest after the laser pulse passed by; this is known as the *Lawson-Woodward theorem* [Esarey et al., 1995].

2.1.2 The ponderomotive force

For realistic high-intensity laser pulses, the temporal and spatial laser profile has to be taken into account, as this significantly differs from the plain wave approximation (uniform in space and slowly varying in time) assumed above. In reality, the laser is strongly focused and of a pulse duration of only 10s to 100s of femtoseconds. The resulting - typically Gaussian-like - electric field distribution in space in all three dimensions causes the occurrence of an additional force: the ponderomotive force, leading to charge separation and (permanent) heating of the electrons.

Historically, the ponderomotive force has already been introduced in the 19th century [Drude, 1897], but is nowadays mainly used in the context of the rather young field of relativistic laser matter interaction. In the following, a purely heuristic argumentation will be performed to introduce and understand this force (as described in [Gibbon, 2005]), starting with the non-relativistic ($v \ll c$) case, in which the equation of motion (equation 2.1) is described as

$$\frac{\partial v_x}{\partial t} = -\frac{e}{m_e} E_x(\mathbf{r}). \quad (2.9)$$

As introduced above, the EM wave is propagating in $+z$ -direction and the electric field oscillates in x -direction; this time, however, with a radial intensity dependency. Taylor expansion and sorting by the orders of E_x gives the plain wave solution in lowest order and in second order a fast oscillation term of the form:

$$\frac{\partial v_x^{(2)}}{\partial t} = -\frac{e^2}{m_e^2 \omega_L^2} E_0 \frac{\partial E_0(x)}{\partial x} \cos^2(\omega_L t - kx) \quad (2.10)$$

Multiplying by m_e and taking the cycle-average yields the ponderomotive force f_p on the electron:

$$f_p = -\frac{e^2}{4m_e \omega_L^2} \frac{\partial E_0^2}{\partial x} \quad (2.11)$$

This force can be expressed as the spatial derivative of a potential $f_p = -\nabla \Phi_p$, the ponderomotive potential of the laser field $\Phi_p = \frac{m_e c^2}{4\gamma^2} \alpha_0^2$. This non-relativistic calculation still ignores the magnetic field and the electron is consequently pushed out of the laser focus under 90 deg to the laser propagation direction. An additional forward push is inserted when taking into account the magnetic field component and moving towards relativistic intensities (as described already above). The ponderomotive force gives a good estimate for the temperature of the resulting electron distribution $k_B T_e = \Phi_p$ [Wilks et al., 1992, Malka and Miquel, 1996], which is commonly used.

The relativistically correct solution was calculated by [Bauer et al., 1995] and reads:

$$\mathbf{f}_p = -m_e c^2 \nabla \bar{\gamma} \quad (2.12)$$

with $\bar{\gamma} = \sqrt{1 + a_0^2/2}$ the time-averaged (over one laser cycle) relativistic factor for linear polarized light; the solution for circularly polarized light is similar, only with just a_0^2 instead of $a_0^2/2$. While solving the equation of motion for the electron is only possible numerically, the final kinetic energy W_p and propagation angle θ (relative to the laser propagation direction) can be calculated to

$$W_p = (\bar{\gamma} - 1) m_e c^2 \quad (2.13)$$

and

$$\tan^2(\theta) = \frac{2}{\bar{\gamma} - 1} \quad (2.14)$$

This shows a direct relationship between electron angle and ejection energy. In the interaction with an overdense target as in laser-driven ion acceleration experiments, however, the electron beam is scattered while moving through the target and thus this dependency is typically not observed.

2.1.3 The laser plasma interaction

With the ponderomotive force as accelerating force for electrons in relativistic laser fields at hand, one can now explore the collective effects of the laser plasma interaction when focusing a high-power laser onto an overdense target.

Typically, sufficient laser intensity to ignite a plasma is already focused on the target before the main pulse arrives, causing an expanding plasma on the target surface. This preceding laser intensity is due to either amplified spontaneous emission (ASE) or even separate prepulses, that may occur within the laser system. While prepulses can be identified and removed, the ASE is an intrinsic effect, as the amplifiers obviously need to be fired before the main pulse passes by and switches to block the propagating beam (e.g. Faraday rotator) cannot be operated on picosecond level. Therefore, the ASE interacts with the target already up to a few nanoseconds before the main pulse. Typical contrast levels (ASE/main) are of the order of 10^{-6} to 10^{-8} . Improvement of this contrast level is possible by either reducing the ASE level - like with the *ultrafast optical parametrical amplification* stage (uOPA) at PHELIX presently [Wagner et al., 2013] - to a laser contrast of 10^{-10} to 10^{-12} or with the help of a plasma mirror [Rödel et al., 2011]. Even though the rising edge of the main laser pulse ignites a plasma on the target surface and the laser interacts then with this plasma. The parameter of interest is the time scale, which determines the scale length $l_s = c_s t$ of this so called pre-plasma. It can be estimated by the ion sound speed,

$$c_s = \sqrt{\frac{k_B Z_i T_e}{m_i}}, \quad (2.15)$$

with k_B the Boltzmann constant, Z_i the ion charge state, m_i the ion mass and T_e the electron temperature (the ion temperature is neglectable) and is in the order of magnitude of a few micrometer to a few 100s of micrometer, depending on how long before the main pulse arrival the pre-plasma is ignited. Additionally, the ablating plasma causes a shock wave traveling the opposite direction (i.e. through the target), which even may destroy the target before the main pulse arrives, if the prepulse/ASE level is too high and/or the target is too thin.

While the ions in good approximation represent a static background, the laser interacts within the pre-plasma with the electrons and excites electron oscillations with the electron plasma frequency,

$$\omega_p^2 = \frac{e^2 n_e}{\epsilon_0 \bar{\gamma} m_e}, \quad (2.16)$$

with n_e the electron density. For the case of $\omega_p > \omega_L$ the plasma is called overdense; penetration of the laser in the plasma is only possible up to the critical density n_c , where $\omega_p = \omega_L$. Beyond this limit, the plasma refractive index,

$$\eta = \sqrt{1 - \frac{\omega_p^2}{\omega_L^2}}, \quad (2.17)$$

becomes imaginary: the laser gets reflected and only evanescent penetration is possible.

The next section introduces the interaction mechanisms of the laser with the electronic system in the pre-plasma up to the critical density.

2.1.4 Electron acceleration and spectrum

The laser matter interaction is (almost completely) reduced to the interaction between laser and electrons and can be assumed collisionless for intensities $> 10^{16}$ W/cm² as the collision probability is decreasing with increasing electron temperature. Several collisionless absorption mechanisms are possible and an overview of these and their contribution to the electron heating will be given in the following.

If the laser is propagating through a thin underdense plasma with a low density gradient, the continuous ponderomotive electron depletion from the intense laser focal region causes an electron density modulation in the wake of the laser pulse. Electrons trapped in this wake are efficiently accelerated and narrow-bandwidth, high-energy electron bunches can be created. This *laser wakefield acceleration* [Tajima and Dawson, 1979] can be used for efficient electron acceleration in thin plasmas and on comparatively large scale lengths. This, however, is normally not the case for laser-driven ion acceleration experiments, where the laser interacts with an overdense target and steeper density gradients. Here, other mechanisms are predominant.

The main absorption occurs when approaching the critical density and shows a dependency on the plasma scale length (l_s/λ_D), the laser incidence angle and the laser polarization. For still rather flat density gradients (with a defined local plasma frequency), *resonance absorption* is observed. A p-polarized laser pulse with non-zero angle of incidence tunnels through to the critical surface and drives a static electron plasma wave at the laser frequency ($\omega_{es} = \omega_L$). At an optimum angle of incidence this mechanism is able to transfer a large fraction of energy from the laser into the electron system.

At steeper density gradients the resonant absorption breaks down as no local plasma frequency can be defined anymore and the related *Brunel heating* (also called *vacuum heating* or *not so resonant absorption*) gets dominant. It is also depending on p-polarization of the laser and an optimum angle of incidence. The descriptive picture of the mechanism is given by electrons being accelerated within half a laser cycle by the laser's electric field and then crossing the critical density, which represents a barrier for the field. In this way, the electron is not decelerated again with the field screened behind the critical density.

Measurements for the combined absorption efficiency (dominantly resonance absorption and Brunel) reach up to 80%. A calculation result for (solely) the Brunel efficiency and experimental measurements of the overall absorption are shown in figure 2.1.

However, the polarization and angle dependency would result in a complete suppression of the mechanism (as well as the resonance absorption) if e.g. s-polarized light is used. Still efficient electron heating can be observed without p-polarization in experiments and simulations. One explanation is that the critical surface is bent due to the transverse laser intensity profile and thus an effective p-polarization is present in any case. Alternatively, another electron acceleration mechanism is possible, which is also in discussion for being the dominant absorption mechanism: the *relativistic $j \times B$ heating*.

The main differences are that this one is driven by the $v \times B$ term of the Lorentz force (instead of solely the electric field), that it works for any linear polarized light and that it is most efficient at zero degree incidence. For the $v \times B$ term to give a significant contribution, relativistic oscillation velocities of the electrons have to be reached. The resulting longitudinal force is described by:

$$f_x(t) = -\frac{m}{4} \frac{\partial v_{os}^2(x)}{\partial x} (1 - \cos 2\omega_L t) \quad (2.18)$$

with the electron mass m , the electron oscillation frequency ν_{os} and the laser frequency ω_L . The non-oscillating part can be identified as the ponderomotive force and the oscillating contribution leads to heating, similar to the electric field component parallel to a density gradient in the Brunel mechanism. Finally, additional other effects of electron heating may occur, e.g. caused by the *anomalous skin effect*. However, they typically give only a minor contribution to the overall process.

Due to the random nature of the hot electron generation, a continuous spectrum is created. A Boltzmann distributed hot electron density $n_{e,hot}$ is obtained by simulations and measurements and therefore assumed further on as

$$n_{e,hot} = n_{e,0} \cdot \exp\left(-\frac{E}{k_B T_{e,hot}}\right) \quad (2.19)$$

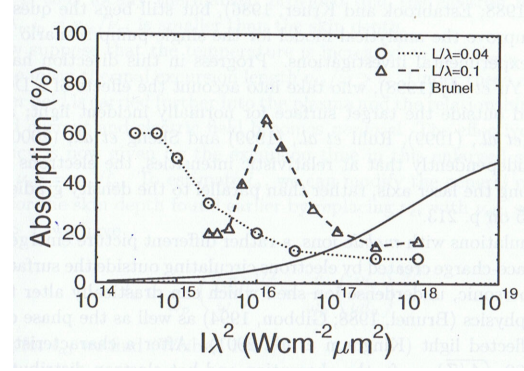


Figure 2.1: Absorption of laser light in dependency of laser intensity. In dashed lines experimental results are shown for two different plasma scale lengths and the solid line represents the calculated absorption by Brunel heating (taken from [Gibbon, 2005]).

with the parameters $n_{e,0}$ and $k_B T_{e,hot}$, where the later is often assumed to be equal to the ponderomotive potential [Wilks et al., 1992, Malka and Miquel, 1996],

$$\Phi_p = k_B T_{e,hot} = m_e c^2 \left(\sqrt{1 + \frac{a_0^2}{2}} - 1 \right), \quad (2.20)$$

and is in the order of a few MeV for laser intensities reached at PHELIX and comparable facilities today. The absolute number of electrons per unit volume $n_{e,0}$ can also be estimated, assuming that the electrons are produced in the volume of the laser focal spot and knowing the laser energy and laser-to-electron conversion efficiency. The latter shows an intensity dependency and can be simulated [Wilks et al., 1992] and measured [Key et al., 1998]. Summing up for the available parameters at PHELIX, this yields a conversion efficiency of a few 10s of percent of laser energy to hot electrons and a total number of hot electrons of more than 10^{13} .

These generated hot electrons, that are pushed into the target, represent an electric current. The large numbers and short time scales involved (sub-ps laser pulse duration) result in electrical currents of several MA and therefore violate the Alfvén limit $I_{max} = 1.4 \times 10^4 \beta \gamma$ [Davies, 2006], which only allows maximum currents in the kA region. As a consequence, a counter-directed return current has to exist for current compensation and a resulting net current below the Alfvén limit.

The hot electrons' initial angular distribution is further broadened by multiple small angle scattering when entering the solid density region of the bulk target material. Therefore, the target thickness plays an important role, as the electron beam size and intensity, when reaching the target's rear side, are directly linked to the resulting beam parameters in the TNSA acceleration scheme. Also, electrons leaving the target on the rear side into the vacuum, are no longer space charge compensated and get pulled back. Such electrons may propagate through the target once more and again be accelerated at the front side by the laser, if the ratio between laser pulse length and target thickness is sufficient. This effect is called recirculation and leads to a higher electron temperature, thus improved ion acceleration [Mackinnon et al., 2002].

2.2 The target normal sheath acceleration mechanism - TNSA

The dynamics of the ions have been neglected so far, as they are much heavier than the electrons and are therefore not able to contribute within shortest time scales like the electrons. Instead, the ions respond to slowly varying electric fields. Such fields are created by the charge separation due to the expansion of the hot electrons. After propagating through the target, the electrons enter into vacuum at the rear side and form an intense electron sheath on the target surface, which causes an electric field with the Debye length λ_D as scale length:

$$\lambda_D = \sqrt{\frac{\epsilon_0 k_B T_{e,hot}}{e n_{e,0}}} \quad (2.21)$$

The Debye length indicates the characteristic screening length of electric fields within a plasma and is of the order of $1 \mu\text{m}$ for the discussed case. The resulting electric fields reach TV's/m and ions on the target rear side get field ionized and accelerated. In the typical experimental setup, impurities and contamina-

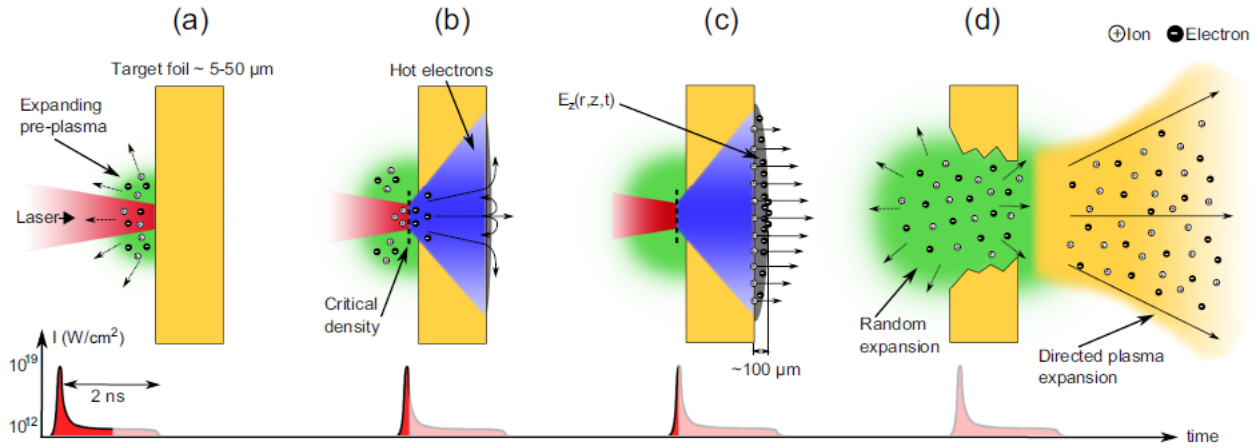


Figure 2.2: Schematic of the TNSA mechanism (picture taken from [Nürnberg, 2010]). (a) Typically, a plasma is ignited on the target front surface already before the main pulse arrives. (b) The main pulse then interacts with this plasma, propagates up to the critical density and accelerates electrons, which then expand through the target and enter the vacuum on the rear side. Due to the charge separation, electrons are pulled back and can recirculate if the laser pulse duration is long enough. (c) The charge separation also causes field ionization at the rear surface and ions get accelerated in the electric field in target normal direction, which (d) results in a directed plasma expansion from the rear surface. Also observed is an undirected plasma expansion from the target front side. As long as the laser lasts, energy transfer to the electrons is possible and the ion acceleration process is sustained. Afterwards the quasi-neutral plasma expands freely into the vacuum and at later time scales (nanoseconds) the target typically disassembles.

tions are present at the target rear side, containing protons and other light ions. The protons are most efficiently accelerated due to their larger charge-to-mass ratio and screen the field for heavier ions. The accelerating field is (nearly) perpendicular to the target surface. Additionally, the accelerated ions are still 'cold' at the beginning of the acceleration process and therefore the resulting ion beams show unique qualities (e.g. ultra-low emittance) and high particle numbers due to the presence of space charge compensating electrons in the quasi-neutral plasma expansion. Most of today's laser-driven ion acceleration experiments are working in this regime, described by the TNSA model, which was introduced first by [Wilks et al., 2001] and is depicted in figure 2.2.

The theoretical description of the ion acceleration is completely decoupled from the laser-matter-interaction dynamics. The hot electron distribution is assumed to be produced by the laser independently and taken as input parameter for further calculations. The typical values of the parameters $n_{e,0}$ and $T_{e,hot}$ in the distribution function (equation 2.19) are estimated by direct measurements of electron spectra or obtained by scaling laws and absorption models for the laser matter interaction.

Several different models evolved after the first observation of these beams [Clark et al., 2000, Maksimchuk et al., 2000, Snavely et al., 2000]. They range from quasi-static to full fluid approaches and a comprehensive overview can be obtained from [Perego et al., 2011] and references within. Two complementary prominent models will be described shortly in the following.

2.2.1 The quasi-static model by Passoni

In the quasi-static model, a test particle (positive ion) is investigated in the potential of the (static) electron sheath. With a sharp density profile at the target rear side and a hot electron distribution of the shape of equation 2.19, an electric potential and corresponding electric field can be calculated. In the 1D case, the resulting electric field on the surface is given by:

$$E_x = \sqrt{2/e}E_0 \quad (2.22)$$

with e here being Euler's constant and $E_0 = \sqrt{4\pi n_{e,0} T_{e,hot}}$. The field evolution towards $x > 0$ (expansion into the vacuum) can be calculated analytically and the results were published already in [Crow et al., 1975]. The immediate observation is the acceleration of the test particle to infinite energy, which is obviously wrong in the realistic case. This infinite acceleration is an artefact of the Boltzmann distributed electrons as the electric field is not vanishing for $x \rightarrow \infty$. A simple way to remove this effect is to define a maximum electron energy $E_{e,max} = uT_{e,hot}$. A thus 'truncated' electron distribution now leads to a finite energy of the test particle when passing the potential. A calculation of that case is presented in [Passoni and Lontano, 2004] and the difference between the 'truncated' and standard Boltzmann distribution is illustrated in figure 2.3: the electric field becomes zero at a defined position ξ_r , depending on the parameter u .

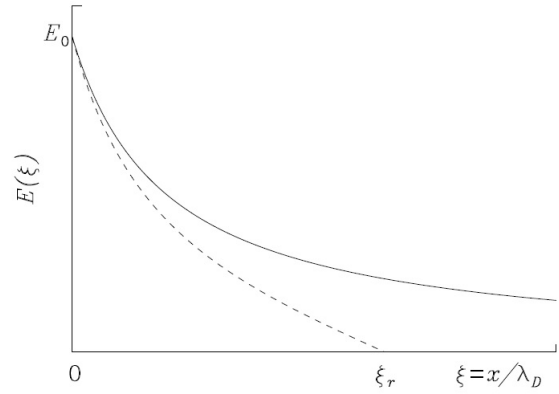


Figure 2.3: The sheath field in the vacuum region ($x > 0$), assuming a standard Boltzmann distribution for the hot electrons (solid line) and a 'truncated' distribution (dashed line) with maximum electron energy $E_{e,max} = uT_e = 3T_e$. (taken from [Macchi, 2013])

With this simple model, the scaling of the maximum proton energies can be reproduced quite precisely (compare [Perego et al., 2011]) and further improvements have been added continuously [Passoni et al., 2010]. Of major importance is the steep density gradient on the target back side in the initial density profile. If this gradient is flattened (e.g. by a pre-pulse-induced shockwave, that travels through the target and reaches the back side before the main pulse drives the acceleration process), the acceleration mechanism breaks down [Mackinnon et al., 2001]. With ultra-high contrast lasers on the other hand, also the plasma scale length at the target front side can be very short (high density gradient) and TNSA is observed to both sides [Ceccotti et al., 2007].

2.2.2 The plasma expansion model by Mora

Another theoretical approach uses a fluid model and is presented in [Mora, 2003]. It describes the acceleration process by a simplified plasma expansion driven by the hot electron distribution. As it

permits a good access to the theoretical understanding and also predicts a full proton spectrum instead of only maximum energies, it will be outlined in this section shortly.

The model is purely in 1D and the initial setup is an infinite quasi-neutral plasma slab for $x < 0$ and vacuum for $x > 0$ to represent the 1D case at the target rear side. Assuming a quasi-neutral isothermal plasma expansion into the vacuum, the equations of motion can be solved and a self-similar solution obtained for the electron and ion density distributions n_e and n_i :

$$n_e(x, t) = Zn_i(x, t) = n_{e,0} \cdot \exp\left(-\frac{v}{v - \zeta}\right) = n_{e,0} \cdot \exp\left(-\frac{x}{c_s t} - 1\right) \quad (2.23)$$

with Z being the ion charge state, $v = c_s + x/t$ the bulk velocity and $\zeta = x/t$ the self-similarity parameter. $c_s^2 = Zk_B T_e/m_i$, the ion speed of sound in the plasma, denotes the expansion velocity of this rarefaction wave. From this model, formulars for the energy distribution function and maximum energy of the ions can be derived; in the case of protons they read:

$$\frac{dN}{dE_p} = \frac{n_{e,0} c_s t_{acc}}{\sqrt{2k_B T_e E_p}} \exp\left(-\sqrt{\frac{2E_p}{k_b T_e}}\right) \quad (2.24)$$

$$E_{p,max} = 2k_B T_e \ln^2\left(\tau + \sqrt{\tau^2 + 1}\right) \quad (2.25)$$

Here, t_{acc} denotes the acceleration time, which can be estimated by the laser pulse duration τ_L via $t_{acc} \approx 1.3 \times \tau_L$, and τ is the normalized acceleration time with respect to the proton plasma frequency ω_{pp} : $\tau = \omega_{pp} t_{acc} / \sqrt{2e}$ (here e again denotes the Euler's number). The presented scaling has also been fitted successfully to experimental data [Fuchs et al., 2006]. The introduction of a maximum acceleration time is necessary similar to the introduction of a maximum hot electron energy in the previous presented model. Otherwise the acceleration would be infinite. Figure 2.4 illustrates the situation for both, the 'corrected' and 'uncorrected' solution. This model by Mora yields a good prediction of the expected exponential shape of the proton spectrum.

However, the Mora model has several limits: The 1D model cannot obtain intrinsic 2D results like the divergence of the beam. Furthermore, the initial assumption of electrons and ions in thermal equilibrium as well as the strict quasi-neutrality is wrong, as the TNSA is driven by *hot* electrons (while the ions are *cold*) and huge accelerating fields occur. Consequent extension of the model

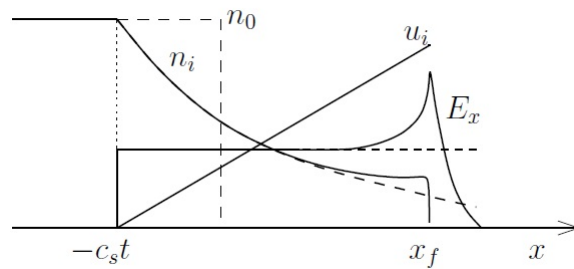


Figure 2.4: Sketch of the ion density (n_i), velocity (u_i) and electric field (E_x) in the case of a 1D isothermal expansion. Dashed and solid lines show the self-similar and 'corrected' profiles, respectively. (taken from [Macchi, 2013])

[Mora, 2005] step by step faced the later limitations and today a more sophisticated model is available [Diaw and Mora, 2011, Diaw and Mora, 2012], which shall not be discussed here, but recommended for further reading.

Consistent measurements of the dynamic field evolution during the expansion could be performed experimentally [Romagnani et al., 2005]. Finally, for the maximum proton energy, also another (empirically) formula gives a good estimate for today's laser parameters [Tampo et al., 2010] and shall be given additionally as an experimentalist's useful rule of thumb here:

$$E_{p,max} = 10T_e \quad (2.26)$$

Measurements of hot electron spectra at PHELIX have been performed during this thesis and the results are found to be in good agreement with this simple estimate: e.g. a hot electron temperature of 3.3 MeV was measured in a TNSA experiment and simultaneously a maximum proton energy of 34.6 MeV observed; details can be found in [Jahn, 2013].

Conclusively, the TNSA mechanism represents a robust, well understood and with today's available laser systems easy-to-access ion source for short and intense ion bunches (typically protons). These are the necessary qualities for a reliable source for a novel laser-driven beamline concept like the *LIGHT beamline*.

2.3 Diagnostics for laser accelerated ion beams

After the description of the generation of a TNSA ion beam, now the experimental characterization of those beams will be discussed. To take into account for the special beam qualities from a TNSA ion source (e.g. large energy spread and envelope divergence), compatible detection methods have been developed. This section provides an overview of existing methods, their possibilities and limitations.

For diagnosing ion beams that originate from an intense laser matter interaction, passive detectors proved to be most reliable, because any electrical device needs to be able to withstand the occurring massive radiation background (EMP, X-rays, γ -radiation). Furthermore, resolving the energy spectrum and handling the large envelope divergence of the beam is a challenge for possible diagnostics. Established detection techniques are introduced in the following section with a focus on the *Radiochromic Imaging Spectroscopy*, which serves as a major diagnostic method in this thesis. Further detector development and improvement had been necessary, which is why a short review on existing techniques serves as motivation for the additional methods that will be introduced later on at the appropriate stages.

2.3.1 Detectors based on dispersion in EM fields

For a full spectral measurement of a laser accelerated ion beam, dispersion in static magnetic and/or electric fields can be used. The most common devices are the Thomson parabola [Mori et al., 2006] and the ion wide angle spectrometer [Jung et al., 2011], typically with image plates (IPs, [Izumi et al., 2006]) or CR39 as detectors. At greater distances to the laser target, also electrical detection systems (e.g. a multi-channel-plate in connection with a scintillating phosphor screen [Harres et al., 2008, Carroll et al., 2010]) are possible.

A *Thomson parabola* (TP) disperses the ions in parallel electric and magnetic fields due to their charge-

to-mass (q/m) ratio. For each q/m value a separate ion trace in the shape of a parabola is detectable behind the fields. With the knowledge of the deflecting fields the dispersion relation is accessible: the traces can be connected to specific ions (q/m values) and a relation between ion energy and position on the parabolic trace is obtained. For protons with $q/m=1$ a unique trace identification is possible. For other ions this is not always the case, as e.g. C^{6+} and O^{8+} have the same q/m value and thus overlapping traces on the detector. Still, much information is obtained about different ion species and charge states within the beam.

A more important drawback of the method is the necessity of a very small (sub-mm) entrance pinhole to the dispersing EM fields to provide an acceptable energy resolution within the trace. As a consequence, a TP covers only a very small solid angle of the initial beam. Positioning of several TPs at different angles to the beam helps for characterizing the angular distribution, but still results in losing a lot of information.

An *ion wide angle spectrometer* (iWASP) represents the attempt of a dispersion-based spectrometer in combination with a large angle coverage. Therefore solely a transverse magnetic field is applied and instead of a pinhole a wide slit is used. This allows for measuring the correct angle dependency (at least to some extent) at the expense of different particle species and charge states being more difficult to distinguish. Still an angular-resolved continuous spectrum is recorded, which is especially helpful for experiments that aim at a modulation of the spectral shape.

In most laser-driven ion acceleration experiments, the focus is on the dominantly and most effectively accelerated protons. The iWASP is easily modified to detect only protons by placing an absorption foil in front of the detector. Heavier ions show a significantly reduced penetration depth in comparison to the protons and are efficiently removed from the beam by this absorption layer.

2.3.2 The radiochromic imaging spectroscopy

The most powerful detection method for laser-accelerated protons is the *Radiochromic Imaging Spectroscopy* (RIS, [Nürnberg et al., 2009]). Again, the particle beam is stripped of the heavier ions by a first absorption foil and the protons are then analyzed spectrally and spatially, covering the full envelope beam profile. This technique is based on the proton's energy deposition in radiochromic films (RCFs). These films consist basically of a radiation sensitive layer on a plastic substrate and are commercially available in several types with different sensitivities. Figure 2.5 shows the schematic structure of the RCF types used in this thesis: HD-810, HD-V2, MD-V2 and EBT3 (in order of increasing sensitivity). Further details on the films, their absolute calibration and the methodology in general in the current form can be found in [Schreiber, 2012].

Adding several RCFs to a stack and placing it close (few cm) to the TNSA source is the basic principle of the RIS. Heavier ions like the typically also present carbon, oxygen or target ions have a much shorter penetration depth than the protons and are easily stopped with a first layer of several 10s of μm of a dense material (such as copper or nickel). This also blocks low energetic electrons and soft X-rays. The protons penetrate the stack and deposit energy according to their well known Bragg curve. This results in a blueish coloring of the RCFs. Due to the Bragg behavior and the exponential decreasing energy spectrum, the permanent imprint in each RCF can be connected mainly to protons of the corresponding *Bragg energy* of the position in the stack. As *Bragg energy* we define here the (initial) proton energy with

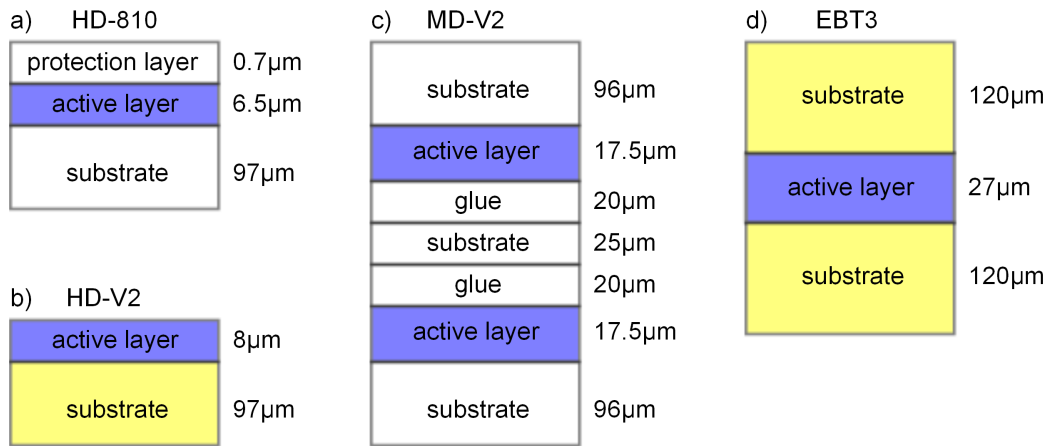


Figure 2.5: Structure of the different RCF types a) HD-810, b) HD-V2, c) MD-V2 and d) EBT3. The HD films show the lowest sensitivity (and best energy resolution due to the single thin active layer). MDs are used in the medium sensitivity range and have the disadvantage of two separate active layers, which lowers the maximum possible energy resolution. The highest sensitivity is provided by the EBT films. The composition of the different layers can be different for different film types.

the highest energy loss within the sensitive layer of the specific RCF; this is the particle that is stopped exactly at the end of this layer within the stack. In figure 2.6 a typical RCF stack configuration from a TNSA experiment is shown. The aluminium, copper or nickel spacers between the RCFs on the one hand save expansive RCFs and on the other hand provide for a parallel measurement with a similar detection method (NAIS, see section 2.3.3).

Based on SRIM [Ziegler, 2013] energy loss tables a MATLAB routine calculates for each proton energy the corresponding energy loss within each active layer. Figure 2.7 shows the results of such a calculation together with a real example of the radiated films of a stack. Each active layer is connected with a Bragg energy corresponding to the depth of the layer within the stack. Protons below this energy do not contribute to the energy deposition as they cannot penetrate up to this layer. Contrary, higher energetic particles do contribute. However, on the one hand their contribution is weaker and on the other hand (due to the exponential shape of a TNSA spectrum) their particle numbers are lower. This consequently results in a transverse beam image in each RCF, that is dominated by the protons with the corresponding Bragg energy. In this way, assuming a point source and knowing the distance from source to the detector, a good estimate of the energy-dependend envelope divergency and the maximum proton energy is accessible shortly after the experiment. One also notices that a minimum step size in energy resolution

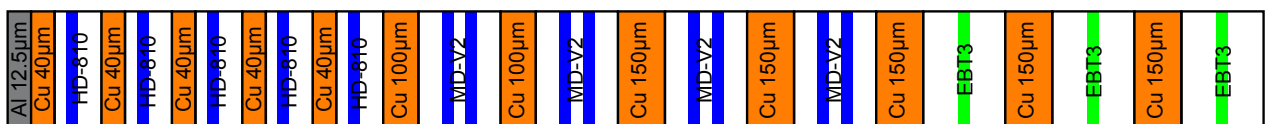


Figure 2.6: Example of a RCF stack configuration. As the particle numbers decrease towards higher energies (i.e. higher penetration depths), the more sensitive MD-V2 films are used in the central part of the stack and the most sensitive EBT3 films at the end.

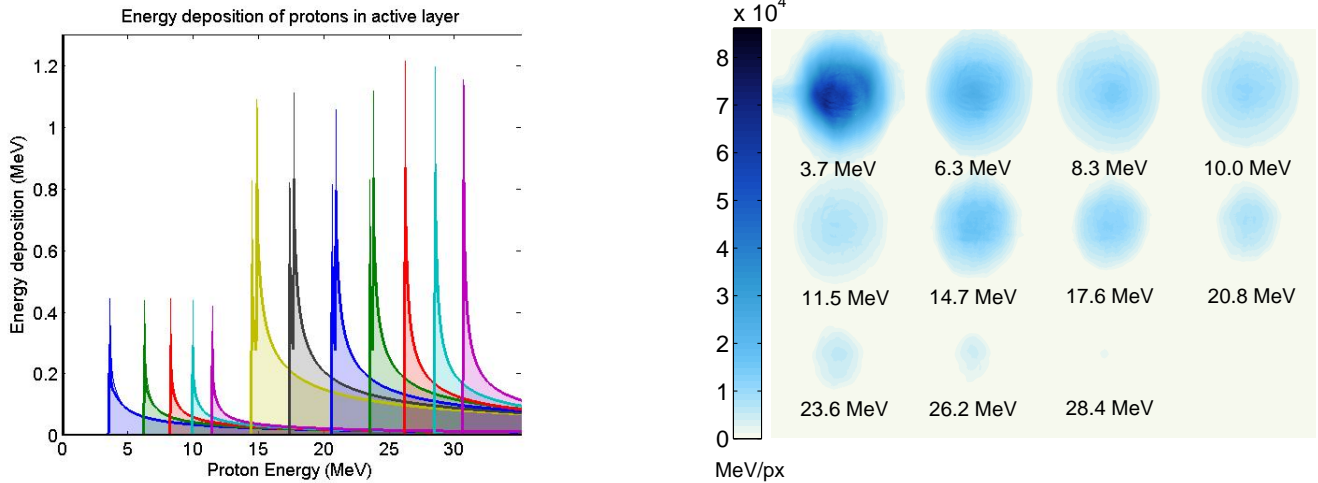


Figure 2.7: Example of the energy-depended deposited energy distribution in each active layer of a RCF for the stack configuration shown in figure 2.6 (left) and corresponding real deposited energy profile in each film after irradiation with a typical TNSA beam (right). The double-peak feature in the energy deposition of the energies E_{6-9} result from the double-layer configuration of the MD type RCFs.

results intrinsically from the structure of the RCFs with a thin sensitive layer and the thicker plastic substrate. This energy resolution is depending on the RCF type and the proton energy. It is typically highly sufficient and needs to be taken into account in special cases only (see section 4.5.1).

For the calculation of the precise energy spectrum and absolute particle numbers, a calibration of the sensitivity of the RCFs to protons is necessary. The calibration, on which the RCF results of this thesis are based on, was obtained in a dedicated beamtime at the tandem acclerator at *Helmholtz-Zentrum Dresden - Rossendorf* and the details can be found in [Schreiber, 2012]. It involves a three color RGB calibration and includes quenching effects, which were observed. As a result, the deposited energy in each RCF can be determined to a precision of about 5%.

The correct detailed analysis of the RCFs is possible 48 h after irradiation, because the films show only about 90% of their color change directly after irradiating them and continue darkening for several hours. This is due to the underlying slow chemical reaction (polimerization) that is causing the color change. Also, permanent direct exposure to sunlight and temperatures above 25 °C have to be avoided. For further analysis, the RCFs are digitalized with the calibrated scanner and processed by a MATLAB routine to obtain the beam parameters (like the absolute particle numbers by deconvolution technique).

As described in [Nürnberg et al., 2009], also the source size can be measured, if using special designed targets. Scretching microstructures into the target rear side results in micro-focusing due to the acceleration in target normal direction and causes a visible imprint in the RCFs. Scretching parallel lines with known distance into the target rear side enables a direct measurement of the (energy-dependend) source size (compare also [Cowan et al., 2004]).

2.3.3 The nuclear activation imaging spectroscopy

Somewhat similar to the RIS, induced nuclear activation by the ion beam can be exploited as a detection method, too. This was demonstrated for characterization of a TNSA proton beam and is described in

[Gunther et al., 2013]. In this case, the protons penetrate a stack of copper foils and induce nuclear reactions due to their cross sections. For protons in the relevant MeV energy range two reactions are dominant in copper: the $^{63}\text{Cu}(p,n)^{63}\text{Zn}$ reaction with a threshold of 4 MeV and a maximum cross section at 13 MeV and the weaker $^{63}\text{Cu}(p,2n)^{62}\text{Zn}$ reaction with 13 MeV threshold and a maximum around 23 MeV. Both resulting zinc nuclei are radioactive with half lives of 40 min and 9 h respectively. Measuring the activation a few minutes after the radiation with the proton bunch results in a large contribution of the ^{63}Zn , which is a $\beta+$ emitter and radiates annihilation radiation. This is measured then by placing the activated copper foils on an IP for a few minutes and analyzing the IP afterwards.

This technique has several advantages: First, the activation in the foils will decay with time, which makes them re-useable (thus cost-efficient). Furthermore, they (practically) cannot run into saturation, are not as sensitive to background radiation as the RCFs and do not inherit their intrinsic energy resolution, as the copper foils can be used in the proper thickness adapted to the experimental conditions. Finally, the technique is suitable for a comparative parallel measurement with RCFs as the RCF stacks typically have additional metal spacers included anyway.

2.3.4 Scintillator-based detector concepts and future developments

All presented detectors so far have the disadvantage that they cannot serve as an online diagnostic (except for the TP in combination with an electrical read-out). Especially the RIS and NAIS technique suffer from a complex analysis. For higher repetition rate laser systems this needs to be optimized and the development of scintillator-based online measurement techniques gained increased attention [Metzkes et al., 2012, Kroll et al., 2013].

Apart from the application at high repetition rates, a fast detection method to monitor the beam characteristics of the laser-driven source without the need to break the vacuum of the target chamber is also very helpful in many other concepts, as the ion production in such a source suffers rather large fluctuations. For this reason, a compact scintillator-based detection system for online spectral and spatial beam monitoring is currently also being developed at TU Darmstadt, using half of the beam for the measurement and providing the other half undisturbed for further applications like the transport and energy compression foreseen in this thesis. These developments are crucially necessary as with the advances in laser technology soon the detectors might represent the bottle neck for accessing higher repetition rates.

2.4 The PHELIX 100 TW beamline

Finally, in the last two sections of this chapter, the specific source characterization for the experiments performed within this thesis is provided, starting with the introduction of the PHELIX laser of GSI (Petawatt High Energy Laser for Ion eXperiments, [Bagnoud et al., 2010]) as the driver of the TNSA proton source. A new beamline (PHELIX 100 TW) has even be built to be able to perform short pulse laser experiments at the Z6 area. Both PHELIX in general and the new beamline in specific will be described.

PHELIX is an international user facility and able to meet many different demands on laser parameters at various experimental areas. The flashlamp-pumped *Nd:glass* laser has a repetition rate for the main amplification stage of one shot every 90 min at the moment. Higher repetition rates are possible if using only the pre-amplification stage, thus limiting the energy of the beam to 10 J. Such

experiments are done at a dedicated experimental area (X-ray Lab). In principle two laser frontends are available, one for pulses on femtosecond (fs) level and the other for pulses of a few nanoseconds (ns). Experiments with the ns frontend are typically performed at the Z6 area where the beam is first converted to the second harmonic before being focused into the Z6 target chamber. For laser-based ion acceleration experiments, the fs frontend is used. The fs laser pulse with a central wave length of 1053 nm is stretched to ns right behind the oscillator for *chirped pulse amplification* (CPA) and amplified within a regenerative pre-amplification stage and a double-pass main amplification stage. Then the pulse is lead to one of the two possible experimental areas for this beam, the PW target chamber in the laserbay or the Z6 area of GSI's experimental hall, both containing their own pulse compressor for re-compression to fs pulse duration. A schematic of the PHELIX laser facility is shown in figure 2.8 and possible (on-target) beam parameters at the two different experimental areas in table 2.1. The achievable laser intensity also depends on the final focusing. With a f/1.7 and a f/5 off-axis copper parabola, the laserbay hold options for both, weak and steep focusing.

	laserbay	Z6
$E_{max,laser}$ [J]	200	15
τ_{laser} [fs]	650	650
I [W/cm^2]	$>10^{20}$	$>10^{19}$

Table 2.1: Available laser parameters at PHELIX for fs pulses.

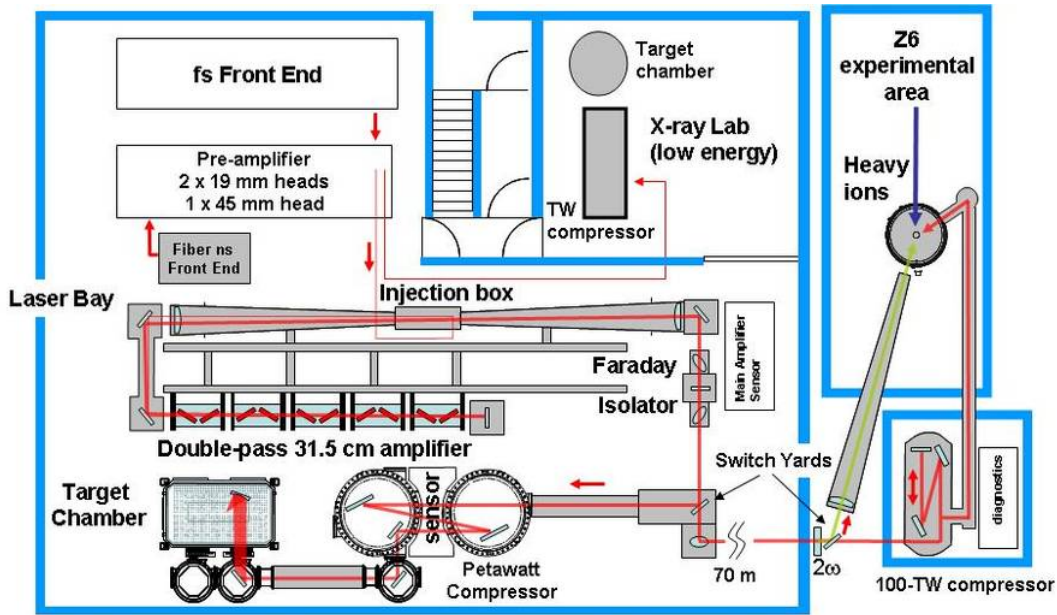


Figure 2.8: Schematic view of the PHELIX laser facility². Available are two different frontends (fs and ns), one experimental area for medium laser energies (X-ray lab) and two different areas for high laser energies (laserbay and Z6).

Although contributing experiments to this thesis were also performed in the laserbay, the major campaigns took place at the Z6 area. For short pulse laser experiments, here a 12 cm laser beamline is available (which is only a sub-aperture beam of PHELIX, thus less energy can be provided within the pulse than in the laserbay with the fs frontend). To avoid the necessity of complex re-arrangement when

² picture taken from <http://www.gsi.de/phelix> (Jan. 2014)

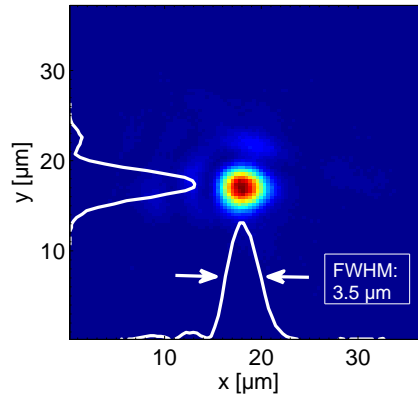


Figure 2.9: Laser focal spot of the PHELIX 100 TW beamline in the Z6 target chamber. 40% of the laser energy are within the FWHM.

working with the full aperture, frequency-doubled long pulse option at Z6, a pick-off mirror after a dichroic mirror in the (vacuum) main beamline is inserted, thus ns and fs pulses can use the same beamline (and setup) up to this separating mirror. Behind this mirror a double-pass pulse compressor is placed, which is enclosed in a vacuum vessel. The compressor gratings are capable of handling up to 50 J of laser energy at the 12 cm beam diameter, but are operated below that limit to avoid damage. Finally, the laser pulse is transported through a vacuum beamline to the Z6 target chamber. The laser pulse, compressed to 650 fs, is focused down to $3.5 \mu\text{m}$ diameter (FWHM, see figure 2.9) beam size within the target chamber by a 6 inch silver coated off-axis glass parabola, therefore allowing for intensities exceeding 10^{19} W/cm^2 . The parabola has a focal length of 300 mm and a full angle of deflection of 22.5 deg. Several important laser beam parameters are routinely measured on-shot, e.g. laser energy, pulse duration, as well as near and far field images of the transverse laser beam profile at several stages along the laser beamline (the last one being directly behind the compressor). Other parameters, like contrast and focal spot size on target, are usually measured separately with the frontend oscillator only. The experiments contributing to this thesis used the PHELIX standard contrast level of 10^{-6} (high contrast option up to 10^{-10} is currently possible).

2.5 Proton beam parameters at the Z6 experimental area

Finally, the accessible proton beam parameters at the Z6 experimental area at GSI will be presented. This defines the beam parameters from the source and therefore the important basic input for the consecutive transport and phase rotation stages.

With the PHELIX 100 TW laser beam to drive a TNSA experiment and the introduced RIS technique at hand, intense proton bunches can be created and characterized at the Z6 experimental area. 5-10 μm thin gold foils serve as laser targets for the experiments presented in this thesis. Typically flat foils are used. Structured targets are also available for a possible complete RIS analysis (including a source size measurement). These targets have parallel lines scratched into the surface of their back sides. The lines are 1 μm deep and 10 μm (or alternatively 20 μm) apart. As described above in section 2.3.2, imprints of these scratches appear then in the RCF and enable an energy-dependent source size measurement. In the following, a fully characterized proton beam from an experimental run at Z6 is presented; the

corresponding stack configuration and resulting energy deposition are identical to the already shown examples (see figure 2.6 and 2.7).

Figure 2.10a shows the deposited energy profile in the RCF layer corresponding to a Bragg energy of 10 MeV. In the large central area, five horizontal lines can be identified. A structured target of $10\ \mu\text{m}$ line spacing was used and therefore the source size of this central region is $40\ \mu\text{m}$. This value is well in the expectations for the used laser and target parameters (compare with the results given in [Nürnberg et al., 2009]). Also shown is the envelope divergence θ of the beam (figure 2.10b) with the corresponding second order polynomial fit of the form:

$$\theta(E) = a_2 \cdot E^2 + a_1 \cdot E + a_0 \quad (2.27)$$

with E in units of MeV, θ in units of degrees and the fit parameters as following: $a_2 = -0.04\ \text{deg}/\text{MeV}^2$, $a_1 = -0.41\ \text{deg}/\text{MeV}$ and $a_0 = 26.47\ \text{deg}$. Finally, figure 2.10c and 2.10d illustrate the measured energy deposition in the single RCF films and the deconvoluted proton energy spectrum:

$$\frac{dN}{dE} = \frac{N_0}{E} \cdot \exp\left(-\frac{E}{k_B T}\right) \quad (2.28)$$

with again E in units of MeV and the fit parameters $N_0 = (5.20 \pm 0.38) \cdot 10^{11}$ and $k_B T = (6.94 \pm 0.46)\ \text{MeV}$. The peak in deposited energy (figure 2.10c) is due to the fact that starting with the sixth film the more sensitive RCF type MD-V2 was used. The last proton irradiated layer in the stack at 28.4 MeV matches very well the fitted cut-off energy of $E_{cut} = 28.43\ \text{MeV}$. The proton spectra always show the same basic spectral shape and only the fit parameters vary due to different laser parameters, target parameters or simply the occurring shot-to-shot fluctuations.

The energy in the laser pulse for this shot was 45 J at the PHELIX main amplifier exit sensor (MAS). A measurement of the transmission efficiency along the 100 TW beamline at Z6 revealed, that due to losses within the beamline the expected energy on target is only one third of this value; the largest single contribution to the losses originates from the compressor, but also from the large transport beamline and the dichroic mirror.

The obtained results demonstrate quite efficient proton acceleration with particle numbers in the region of interest ($(10 \pm 0.5)\ \text{MeV}$ proton energy) of 1.3×10^{10} ($\pm 15\%$). For technical reasons, the regular shots are done with energies between 30 and 35 J (MAS) at the moment, meaning that the expected particle numbers and cut-off energies are lower in most of the results presented in this thesis. The routinely used proton beam spectra showed a cut-off energy around 20 MeV and a spectral shape according to equation 2.28 with $N_0 \approx 4 \cdot 10^{11}$ and $k_B T \approx 4\ \text{MeV}$. For this case, the particle numbers at $(10 \pm 0.5)\ \text{MeV}$ proton energy still exceed 10^9 .

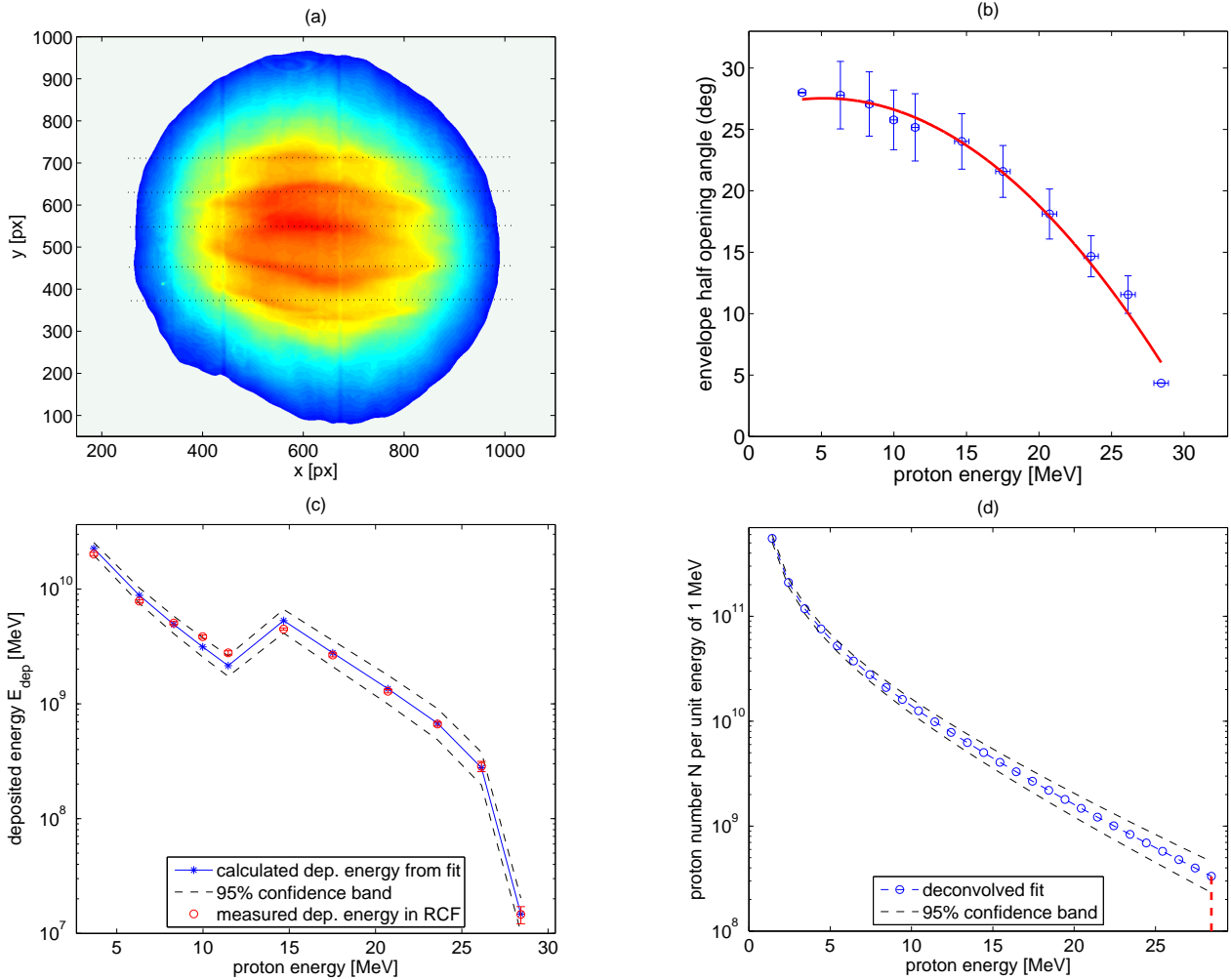
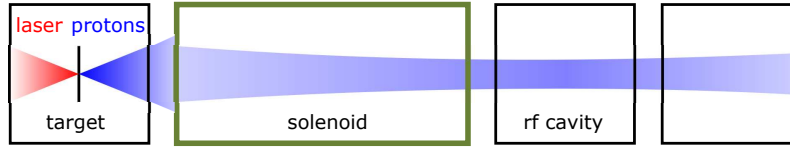


Figure 2.10: Results of the proton beam characterization via the RIS technique. (a) The deposited energy profile in the 10 MeV RCF layer. Visible are the horizontal lines, originating from the structure on the target's rear surface. A source size for the central region of protons around 10 MeV of $40 \mu\text{m}$ is measured. (b) The energy-dependent envelope divergence of the full beam, including a second order polynomial fit [$\theta(E) = -0.04 \cdot E^2 - 0.41 \cdot E + 26.47$]. (c) The measured deposited energy in each RCF with the calculated deposited energy from the deconvoluting fit [$\frac{dN}{dE}(E) = \frac{(5.20 \pm 0.38) \cdot 10^{11}}{E} \cdot \exp\left(-\frac{E}{(6.94 \pm 0.46)}\right)$] and (d) the proton spectrum from source as fitted via the RIS numerical deconvolution method.





3 Beam transport and energy selection

The goal of this thesis is merging a laser-driven TNSA proton source with conventional accelerator technology. Beam transport in accelerators is typically performed with quadrupoles and solenoids. In this work, both methods have been applied (with the main experiments being based on a pulsed solenoid). Hence, their working principles and some basic definitions in accelerator physics are introduced in the following. Further details can be found in many books, specialized on accelerator physics, e.g. [Wille, 1996, Hinterberger, 2008, Reiser, 2008].

3.1 Linear beam optics

Each transport system for a charged particle beam has a defined nominal particle trajectory and the individual particle motion is described relative to this trajectory. Basically, the particles with charge q and velocity v are led on this path via application of electrical or magnetical fields through the Lorentz force. With increasing velocity, the relative effectiveness of electric fields is much lower than of magnetic fields and consequently the particle guiding is typically done by magnetic fields.

A simple categorization is possible, assuming a) a Cartesian coordinate system $K = (x, y, s)$, whose origin moves along the nominal beam trajectory s , b) the particles moving essentially in s direction and c) the guiding magnetic fields only having transverse components (x, y) . With the Lorentz force balancing the centrifugal force $F_r = mv_s^2/R$, this directly leads to

$$\frac{1}{R(x, y, s)} = \frac{q}{mv_s} B_y(x, y, s) \quad (3.1)$$

with R the radius of the curvature of the trajectory. Since the transverse dimensions of the beam are small compared to R , expansion of the magnetic field in the vicinity of the nominal trajectory is possible and leads to the common multipole expansion:

$$\begin{aligned} \frac{q}{mv_s} B_y(x) &= \frac{q}{mv_s} B_{y0} + \frac{q}{mv_s} \frac{dB_y}{dx} x + \frac{1}{2} \frac{q}{mv_s} \frac{d^2 B_y}{dx^2} x^2 + \dots \\ &= \frac{1}{R} + kx + \frac{1}{2} mx^2 + \dots \\ &= \text{dipole} + \text{quadrupole} + \text{sextupole} + \dots \end{aligned} \quad (3.2)$$

Each multipole component has a different effect on the particle. Dipoles are for steering of the beam and quadrupoles for transverse focusing (with k describing the strength of the focusing field). As long as only these two are considered, one speaks of *linear beam optics*. The non-linear components are used for higher order field compensation (e.g. chromaticity compensation with sextupoles) and are neglected in the linear approximation.

For this only linear case, the equations of motion of a particle propagating along the nominal path s can be solved to:

$$x''(s) + \left(\frac{1}{R^2(s)} - k(s) \right) x(s) = \frac{1}{R(s)} \frac{\Delta p}{p} \quad (3.3)$$

$$y''(s) + k(s)y(s) = 0$$

with the relative momentum deviation $\Delta p/p$ from the nominal momentum $p = mv_s$. x and y are the relative deviations to the nominal path s in transverse propagation direction and dipole fields are assumed to be only in vertical direction x , which results in only horizontal bending of the beam. $x''(s)$ and $y''(s)$ are the second derivatives with respect to the spatial coordinate s . The particle motion described by these equations is decoupled for the transverse components.

In a simplified picture the beam transport system of an accelerator consists of drift sections, dipole magnets and quadrupole magnets only. Based on the linear beam optics, the particle trajectories along the nominal path can be described by matrix operations on the transverse beam vector $\mathbf{X} = (x, x', y, y')$ and in sole dependency of the longitudinal position s , the dipole-defining bending radius R and the quadrupole-defining field gradient k with a typical transformation matrix for each element (drift, dipole, quadrupole). These transfer matrices provide a fast and easy calculation possibility for the beam transport.

3.1.1 Beta function, emittance and acceptance

The technique introduced in the previous section only describes single particle motion. In reality, however, the collective behavior of a full particle distribution needs to be described. Therefore, the equations of motion (equations 3.3) are simplified further by $1/R = \Delta p/p = 0$ to obtain:

$$x''(s) - k(s)x(s) = 0 \quad (3.4)$$

This differential equation describes a transverse oscillation about the orbit, known as betatron oscillation. A solution is given with the ansatz

$$x(s) = \sqrt{\epsilon \beta(s)} \cos(\Psi(s) + \phi) \quad (3.5)$$

introducing the beta function $\beta(s)$, which is a measure of the transverse beam displacement, and with the integration constants ϕ and the as emittance known ϵ , which is an amplitude factor, as well as the

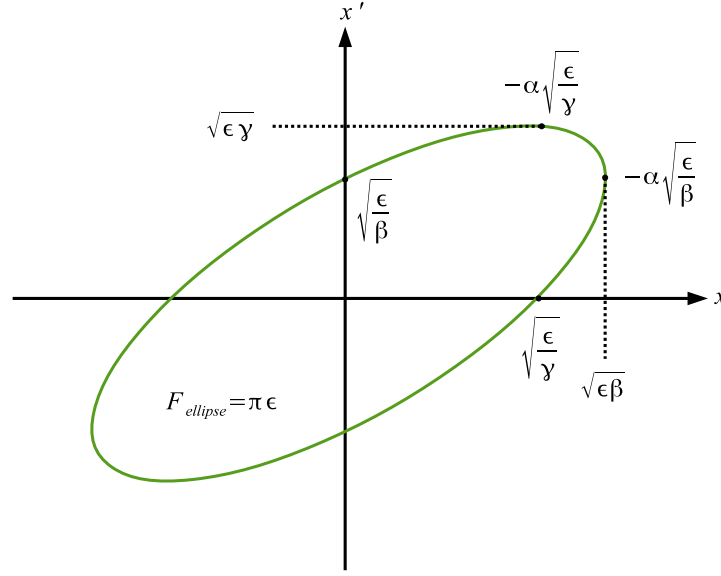


Figure 3.1: Illustration of the emittance ellipse in x - x' phase space. Its area is an invariant of the particle motion and a measure of the quality of the beam.

phase $\Psi(s) = \int_0^s d\sigma / \beta(\sigma)$. For a bunch of many particles this describes a transverse oscillation of each particle along the trajectory s (depending on its position) with the amplitude $E(s) = \sqrt{\epsilon \beta(s)}$. For a complete description of the movement, the derivative of equation 3.5 with respect to s is performed and both equations (3.5 and its derivative) are combined to eliminate the phase $\Psi(s)$. Additionally defining $\alpha(s) = -\frac{\beta'(s)}{2}$ (again derivative with respect to s) and $\gamma(s) = \frac{1+\alpha^2(s)}{\beta(s)}$, this leads to:

$$\gamma(s)x^2(s) + 2\alpha(s)x(s)x'(s) + \beta(s)x'^2(s) = \epsilon. \quad (3.6)$$

This is the general equation of an ellipse in x - x' -plane. Also now the emittance ϵ gains a descriptive meaning, as it is directly linked to the area of this ellipse by $\epsilon = F_{ellipse} / \pi$ (see figure 3.1). Including Liouville's theorem, which states fundamentally that every volume element in phase space is constant in time if the particles obey the canonical equations of motion, this holds important consequences for the calculations with the emittance as basic invariant of the beam transport.

Another important parameter, linked to the transverse dimensions of the beam, is the transverse acceptance A_{trans} of the accelerator, which is defined by

$$A_{trans} = \left(\frac{d^2}{\beta} \right)_{min} \quad (3.7)$$

at the minimum position for the relation between the inner dimension of the accelerator d and the transverse beam dimension β . To avoid beam losses and other distortions through particles hitting the inner wall of the vacuum chamber, in reality up to $A_{trans} > 50\epsilon$ is typically chosen in the design of an accelerator. In the case of this thesis, however, this is violated drastically instead, to use the

limited acceptance in combination with chromatic focusing to select a specific energy interval from the continuous source and suppress the other energies (i.e. removing the particles from the beam by absorbing them in the inner wall of the beamline).

3.2 Charged particles in a solenoid field

While the focusing by quadrupole magnets is the standard method for accelerators and can be well described by the linear beam optics, solenoidal focusing needs separate explanation. A precise formal description is found in several books, e.g. [Reiser, 2008]. The following section, however, will concentrate on the basic understanding of the focusing mechanism and one specific paper on the topic turned out especially helpful [Kumar, 2009]. Its argumentation is sketched in the following.

First, the field of a solenoid is given by the general equations for an axis-symmetric magnetic field in cylindrical coordinates:

$$B_z(r, z) = B(z) - \frac{r^2}{4}B''(z) + \dots \quad (3.8)$$

$$B_r(r, z) = -\frac{r}{2}B'(z) + \frac{r^3}{16}B'''(z) + \dots \quad (3.9)$$

with z being the distance along the solenoid axis and r the radial direction. For simplification, space charge effects are ignored and a parallel cylindrical beam ($\mathbf{v} = v_z \hat{z}$) is assumed. The solenoid of length L is placed at $0 < z < L$ and only the leading terms of equations 3.8 and 3.9 are considered; with inside the solenoid only the longitudinal magnetic field and an infinitely small fringe field region of only a transverse magnetic field at entrance and exit of the solenoid. This simplifies the equations for the magnetic field to

$$B_z = B_0 [u(z) - u(z - L)] \quad (3.10)$$

$$B_r = -\frac{r}{2}B_0 [\delta(z) - \delta(z - L)] \quad (3.11)$$

with $\delta(z)$ being the Dirac delta function, $u(z) = 1$ for $z > 0$ and $u(z) = 0$ else. A charged particle with velocity v_z , which enters the solenoid, gets an azimuthal kick due to the Lorentz force when passing the fringe field region. The resulting velocity Δv_θ is in azimuthal direction, as the particle velocity is only in z direction initially and the fringe field has only a radial component B_r .

$$\Delta v_\theta = \frac{r_0}{2} \frac{eB_0}{\gamma m} \quad (3.12)$$

with r_0 the particles initial radial distance to the solenoid axis and γ the relativistic factor. Introducing the cyclotron frequency $\omega_c = eB_0/\gamma m$ and the Larmour frequency $\omega_L = eB_0/2\gamma m$, the azimuthal velocity increment can be written $\Delta v_\theta = r_0 \omega_L = 2r_0 \omega_c$.

Now inside the solenoid, with the magnetic field in z direction and a velocity component in azimuthal

direction, a radial force occurs and the particles are moving on helical trajectories along z on a radius R_c given by

$$R_c = \frac{\gamma m v_\theta}{e B_0} = \frac{r_0}{2} \quad (3.13)$$

This equation for the radius R_c illustrates the particle motion inside the solenoid: Each off-axis particle, entering the solenoid, propagates on a helical trajectory with a radius half the distance of their initial distance to the center-axis, i.e. around a center at $r_0/2$, rotating from r_0 to the solenoid center and back again to the initial radial distance. The frequency of this rotation is the cyclotron frequency, which is the same for monoenergetic particles regardless of their initial radial component when entering the solenoid. Thus, inside the solenoid, all particles collectively move towards the center of the solenoid within half a period of the cyclotron frequency and back again within the other half. This is illustrated in figure 3.2. An oscillation of the transverse beam size is observed within the solenoid. And to clarify the dependency between cyclotron and Larmour frequencies: Each particle rotates around its individual center of the transverse motion with the cyclotron frequency, but with respect to the center of the solenoid with only half the cyclotron frequency, which is the Larmour frequency. In figure 3.2 this is clarified by the particle covering an angle 2θ with respect to its center of motion and at the same time only an angle θ with respect to the solenoid center.

This transverse particle motion can be described by a radial and an azimuthal velocity component:

$$v_r = -r \omega_L \tan\left(\frac{\omega_L z}{v_z}\right) \quad (3.14)$$

$$v_\theta = r \omega_L \quad (3.15)$$

As soon as the particle now exits the solenoid, it again experiences a kick due to the fringe field, this time in opposite direction and depending on the current radius, $\Delta v_\theta = -r_1 \omega_L$, which cancels the azimuthal velocity to zero. However, the current radial velocity component remains and causes the focusing (defo-

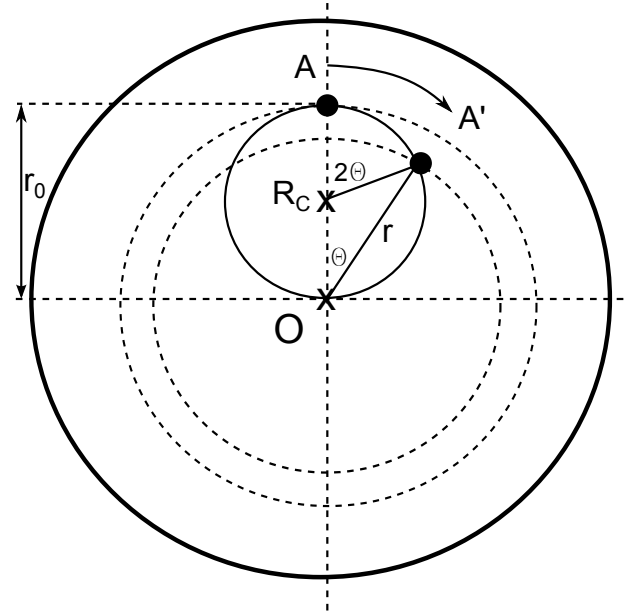


Figure 3.2: Particle motion within the solenoid. The particle enters the solenoid at a distance r_0 to the solenoid center O and rotates around its center of motion $R_c = r_0/2$. Due to this motion, the radius of the beam is reduced ($A \rightarrow A'$).

cusing) behind the solenoid.

In the situation of this thesis, the solenoid can be approximated as a thin lense, i.e. $L \ll v_z/\omega_L$ (or in the above described picture: the solenoid is too short for the particles to be focused already inside a first time). This allows for a small angle approximation of the *tangent* in equation 3.14 and leads to

$$v_r = -\frac{r_0 e^2}{4\gamma^2 m^2 v_z} B_0^2 L \quad (3.16)$$

Now approximating the realistic solenoid field by an infinite sum of those piecewise definitions of the magnetic field (equations 3.10 and 3.11), one can obtain a generalized expression of the focal length f of a thin solenoid:

$$\frac{1}{f} = \frac{e^2}{4\gamma^2 m^2 v_z^2} \int B^2 dz \quad (3.17)$$

This is the final formular for solenoidal focusing, also obtained by other approaches. The integration of the magnetic field is done over the whole length of the solenoid. One should be aware that the particles may already be created inside the fringe field, too. In this case, the azimuthal velocity does not cancel out completely at the exit of the solenoid. The remaining v_θ leads to an increase in emittance (known as *Busch emittance*).

3.3 Characterization of the pulsed high-field solenoid

The pulsed high-field solenoid, which is used in this work, was designed and constructed by the High-field laboratory at HZDR on the basis of the results that have been obtained with the first two prototype solenoids [Harres et al., 2010, Harres, 2010]. It was adapted to the operation at the Z6 experimental area and delivered with a stand-alone pulsed-power supply unit. Commissioning and first experiments of this system are published in [Burris-Mog et al., 2011, Burris-Mog, 2012].

The solenoid itself is 150 mm long and consists of four layers of copper windings around a central stainless steel drift tube. The copper wire has a cross-section of $3 \times 5 \text{ mm}^2$ and the four layers are spatially fixed by enclosing the whole structure in epoxy resin. Furthermore, the coil is inside a stainless steel vessel and kept in air at atmosphere pressure while placed in the Z6 vacuum target chamber (the connectors have appropriate feed-throughs). During experiments this vessel is on electrically floating potential (instead of being grounded) as precaution against high-voltage breakdowns when pulsing the system. Figure 3.3 shows a technical drawing of the design; the connectors are lead directly upwards in the current version instead of entering the vessel from back and causing disturbing magnetic fields at the rear side of the solenoid.

The solenoid is powered by a specially designed pulser. The capacity of the pulser is $180 \mu\text{F}$ and the inductivity of the coil is $250 \mu\text{H}$. Charging the capacity and short-circuiting the condensator-coil-system with a thyatron, that is used as switch, results in a high current building up through the coil. To prevent the typical oscillation of such a LC circuit, it is critically damped with a crowbar diode array. Additionally, a parallel resistance is necessary to damp high-frequency oscillations within the power cable. Such oscillations caused severe electrical breakdowns in an earlier prototype.

The combined pulsed power system can still be approximated well by an ideal LC circuit with a time

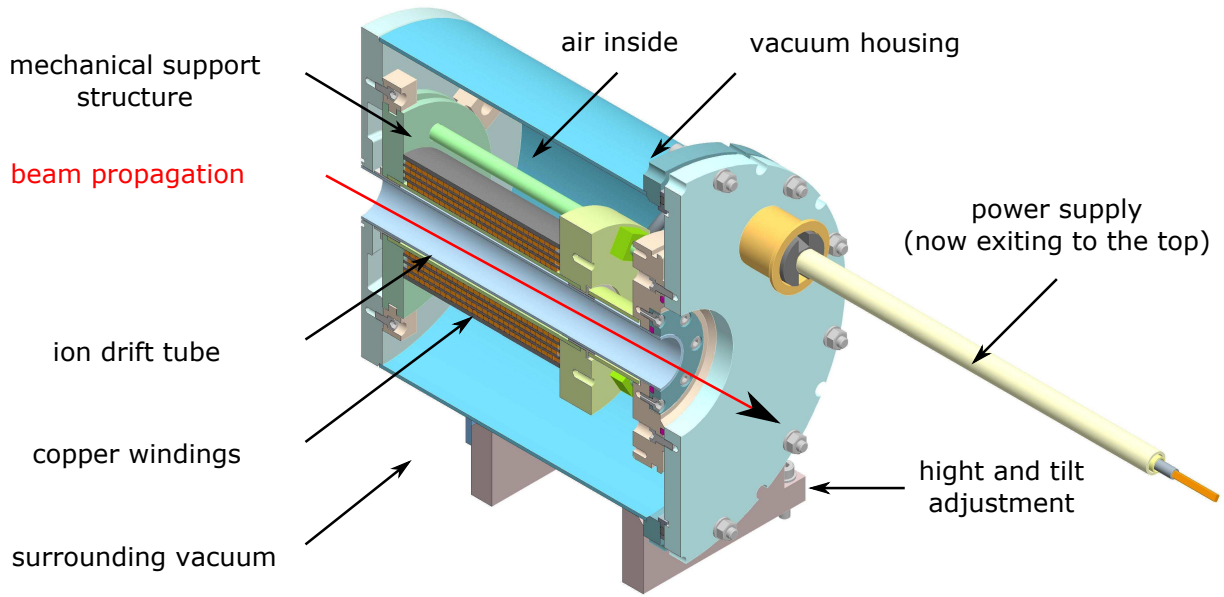


Figure 3.3: Technical drawing (cut) of the solenoid. The coil is housed inside a sealed chamber and positioned in the vacuum target chamber for experiments. The particles propagate through a clear cylindrical aperture. To prevent disturbing magnetic fields at the exit of the solenoid, the power supply cables are led directly upwards in the current design. They are inside vacuum sealed tubes as well, connecting the air chamber of the coil with the ambient atmosphere outside the target chamber. These connections are additionally isolated to ensure that the stainless steel chamber of the solenoid is on floating electrical potential. This minimizes the breakdown probability.

constant $\tau = \sqrt{LC} \approx 0.2$ ms, meaning that the solenoid needs to be pulsed $300 \mu\text{s}$ before the laser hits the target, because at this time the magnetic field reaches its maximum strength. As the time scale for the passing protons (ns) is much smaller than the time scale of the field evolution (μs), the magnetic field is further on assumed to be constant during the proton acceleration experiment.

An easy relation for the maximum current through the solenoid I_{max} [kA] in dependency of the voltage U_{max} [kV] at the pulser's capacity could be measured and is given by:

$$I_{max}^{coil} \approx 0.65 \times U_{max}^{capacity} \quad (3.18)$$

And similarly an estimate for the maximum magnetic field within the solenoid $B_{z,max}$ [T] could be obtained by measurements and simulations (which will be shown in the following section):

$$B_{z,max}^{coil} \approx 0.84 \times I_{max}^{coil} \quad (3.19)$$

3.3.1 Solenoid field distribution measurement and simulation with *CST particle studio*

The 3D field distribution was measured at 40 A DC - a measurement in pulsed mode is not possible - at GSI. Furthermore, detailed comparative simulation studies were performed using *CST particle studio*

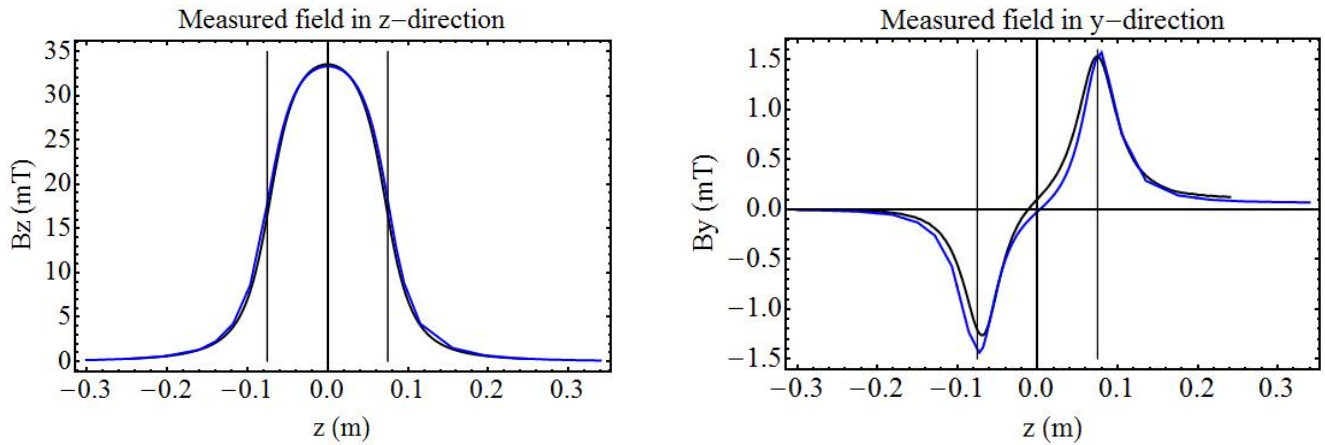


Figure 3.4: Comparison between the measured (black line) and simulated (blue line) magnetic field distribution of the solenoid for the longitudinal component z (left) and the vertical component y (right). While the measurement was done with DC current, the simulation is a full dynamic approach with the commercial program *CST EM studio* (courtesy of P. Schmidt). A good agreement is found.

[CST, 2013], modeling the coil as an axis-symmetric current around the beam tube. The results of a magnetostatic simulation of the field distribution match the measured field well and a full dynamic simulation showed only a small deviation due to the occurrence of induced eddy currents within the stainless steel drift tube. Namely, the maximum field strength decreases slightly and a phase shift is observed ($\Delta t = 40 \mu s$). Both effects can be neglected. Figure 3.4 shows the good agreement between measurement and simulation. The non-vanishing B_y component towards large values of z is an artifact of the connectors being attached from the back side still. This caused an additional magnetic field along the ion path behind the solenoid due to the current through the cables. They are now lead upwards to avoid this disturbing field on the particle propagation axis.

The simulated field is extracted and used as a field map for further particle tracking simulations done with *TraceWin* (see next section). As the solenoid (without the connectors) was modelled axis-symmetric, the field is as well and therefore only a 2D field distribution plane is extracted with a step size of 1 mm and a r - z -symmetry used for 3D interpolation.

3.3.2 Beam propagation and particle tracking simulations with *TraceWin*

The complex laser matter interaction in a typical laser-based ion acceleration experiment can only be accessed with *particle in cell* (PIC) simulations. However, they are very time-extensive and thus their reasonable application limited to small scales only (typically picoseconds in time and 10s to 100s of micrometer in space). A beam transport study using a TNSA source therefore leaves two possibilities: Either an overall solution that requires the code to adaptively change mesh and step sizes (e.g. the specially developed LASIN code, see [Almomani et al., 2012]) or a two-staged approach, starting with a normal PIC solver and creating acceptable output parameters after the acceleration phase as input for a consecutive beam transport code (a first step on this is taken e.g. in [Lecz, 2013]).

In the thesis at hand, yet another option is chosen: The proton spectra of the performed TNSA experiments are well described by a modified exponential spectrum with the two free parameters N_0 and $k_B T$

(see equation 2.28) via the RCF method (see section 2.3.2 and [Nürnberg et al., 2009]). Values for the energy-dependent beam divergence and source size are measured, too. From these parameters, a (in particle numbers down-scaled) realistic random 6D proton beam distribution is generated and used as input beam for simulations with the code *TraceWin* [cea, 2013]. Although *TraceWin* is in principle able to handle space charge effects and self-fields to some extent, those are neglected in the purely ballistic particle tracking (via the *Partran* implementation in *TraceWin*), thus avoiding the problem of Coulomb explosion of the beam right at the source due to the missing space charge compensating electrons.

TraceWin represents a fast, flexible and easy way to perform transport studies. Most conventional accelerator components are implemented (solenoids, quadrupoles, rf gaps, ect), apart from custom beam distributions also custom field maps can be imported and a graphical user interface including many output options is available. The simulation results presented in this thesis are typically obtained with *TraceWin*. The effect of neglecting space charge and especially the electrons, that are present in the experiment, will be discussed separately.

During this thesis, comparative studies with *CST particle studio* were performed, too. When referred to them, they are mentioned explicitly.

3.3.3 *TraceWin* simulation setup for the solenoid

For the comparative simulation studies with *TraceWin* the field distribution for the solenoid obtained with a *CST* simulation is used. In this way most accurate results are obtained. The inserted field map covers 310 mm, the 150 mm within the actual coil and additionally 80 mm to each direction to cover the important fringe fields. Scaling of the inserted field map, which is normalized to a current through the coil of 1 kA, to adjust for different field strengths is possible.

The simulation setup starts with the particle source. This is either the (random generated) full proton spectrum, which is adapted to the expected TNSA proton spectrum, or just a monoenergetic proton beam with still the expected remaining characteristics regarding source size and divergence, defined via the *Twiss* parameters in *TraceWin*. The latter has the advantage of very short calculation times and a fast behavior study of a single energy, as all energies can be treated independently without self-fields.

Exemplarily, for a study of 10 MeV protons only, the source is defined as follows: Radial symmetry is assumed and the source size set to $r=50\ \mu\text{m}$ with an half opening divergence angle of $r'=100\ \text{mrad}$ (maximum capture angle of the solenoid in the used setup). For the longitudinal dynamics particles of an energy spread of $\Delta W=\pm 0.5\ \text{MeV}$ are distributed over a phase spread of $\Delta\Phi=\pm 0.1\ \text{deg}$ (at 108.4 MHz, i.e. $\approx 5\ \text{ps}$). This translates to a radial emittance $\epsilon_{r,r'}=5\ \pi\ \text{mm mrad}$ and a longitudinal emittance $\epsilon_{\Phi W}=0.05\ \pi\ \text{deg MeV}$. The *Twiss* parameters can now be calculated to $\beta_x=\beta_y=r^2/\epsilon_{r,r'}=5\times 10^{-4}\ \text{mm}/\pi\ \text{mrad}$ and $\beta_W=\epsilon_{\Phi W}/(\Delta W)^2=0.2\ \text{deg}/\pi\ \text{MeV}$. In the case of the alternatively imported full particle distribution, *TraceWin* does the calculation of the *Twiss* parameters automatically.

Behind the source, a short drift of a few millimeters is optionally inserted to adjust the distances in the simulation to the experimental setup. Then the solenoid field map follows and finally several drifts with varying lengths to monitor the beam at several distances.

Choosing a focal position of 2.2 m for 9.4 MeV protons by applying a field of $B_{z,max}^{coil}=7.35\ \text{T}$ at the solenoid results in a transverse particle distribution as shown in figure 3.5. As expected, the focal energy is con-

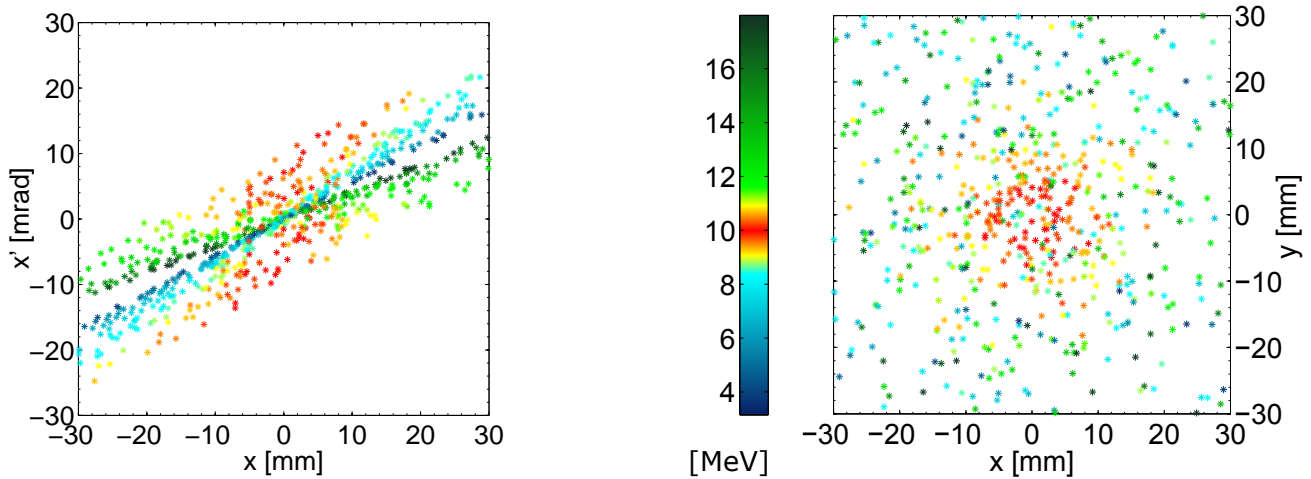


Figure 3.5: Simulated phase space and transverse beam profile of a laser accelerated proton beam at a distance of 2.2 m behind the source. The particles are color-coded due to the adjustment of the solenoid to focus protons of 10 MeV at this position in the simulation; in the experimental campaign 9.4 MeV were focused, which only shifts the central energy and does not change the principal behavior.

centrated in a centered focal spot, surrounded by a particle background of higher and lower energies. Cleaning of the pulse by applying an aperture of the size of the focal spot will block out the major part of these protons, which will be lost within the further beamline anyways. Such losses to the inner wall of the drift tube are present throughout the whole transport section with the major particle losses at and within the solenoid. The overall efficiency is quite low, as the low-energetic particles dominate the exponential spectrum with respect to particle numbers. In the case of a realistic particle distribution available at Z6, only about 1% of the particles are in the energy bin (10 ± 0.5) MeV and not all of them can be captured by the solenoid field because of their initial divergency; only the sub-population with a half-envelope divergence < 100 mrad is collected. This results in losing $> 99\%$ of the initial particles from source.

However, they are to be removed in any case to obtain a peaked particle spectrum around a chosen central energy for the bunch. And high bunch intensities are still observed, as the source provides enough particles initially. Therefore, the particle capture efficiency will be measured further on only with respect to the initially available particle numbers in the relevant energy interval instead of accounting for the full source spectrum.

3.4 Experimental campaign with the solenoid

The many preparative works during the last years on beam transport and focusing with pulsed solenoids [Harres et al., 2010, Burris-Mog et al., 2011] provide a solid basis to implement this technique for consecutive stages like the foreseen phase rotation. Before adding the cavity, however, a full characterization of the beam and the transport properties with the special system at hand is necessary.

3.4.1 The experimental setup

The LIGHT beamline is orientated at 90 deg to the existing UNILAC ion beamline at Z6 (see figure 1.1 in the introduction), as there is enough place towards the Z4 area for flexible expansion of the

beamline without interfering with the existing infrastructure. This final setup is chosen for the transport characterization experiments, too. Beam diagnostic with RCF stacks is possible at several positions and a time-of-flight detector can be optionally used. A sketch containing all distances used in the experiments is shown in figure 3.6.

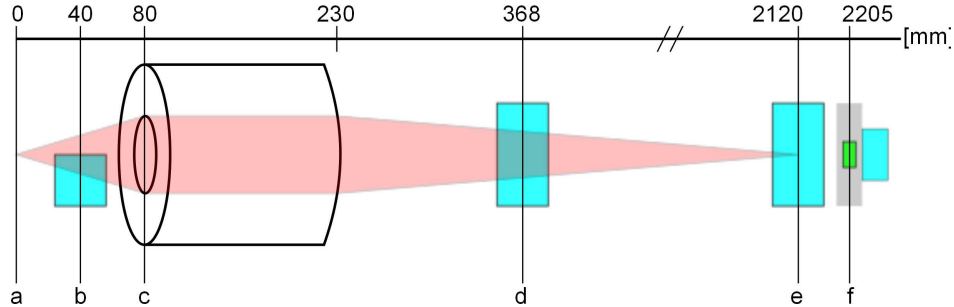


Figure 3.6: Experimental setup. After the protons are produced in the laser matter interaction at the target (a), the divergent bunch enters the solenoid (c). For characterization of the initial beam, a RCF stack can optionally be placed in front of the solenoid at 40 mm (b). For detection of the bunch at larger distances, either a RCF stack was used for dose analysis and transverse beam profile measurements at distances up to 2120 mm (d,e) or a diamond detector at 2205 mm for time-of-flight measurements (which can be operated in transmission) with also a RCF stack attached to detect the protons after passing the 20 μm thin diamond (f).

3.4.2 Transport efficiency and focusing field verification

To verify the solenoid's transport characteristics, the beam has to be measured near to the solenoid exit. At greater distances, most particles other than the focused one are lost to the inner wall of the beamline or hardly detectable due to the defocusing.

A position of 368 mm behind the source was chosen for a full aperture RCF stack in combination with a half aperture RCF stack at 40 mm. Taken the assumption of a symmetric beam, in this way the initial spectrum from source can be directly compared to the transported spectrum. This is necessary because of the typically observed shot-to-shot fluctuations in particle numbers up to a factor of 3. Furthermore, with half the beam blocked at the entrance of the solenoid, the energy-dependent rotation of the particles in the magnetic field is easily observed and can be used for benchmarking the simulations. Figure 3.7 shows the result of such a measurement in direct comparison to a simulation of the same experimental conditions with *TraceWin*.

In this experiment, the solenoid was set to focus 9.4 MeV protons at a distance to source of 2.2 m, i.e. a (maximum) magnetic field of 7.35 T. Beam size and rotation angle match the simulations well (maximum deviation of less than 10%). While the comparative simulations are separate single runs with only a mono-energetic proton beam at the corresponding Bragg energy for each layer, one has to keep in mind that in the experiment the RCFs show also an overlapping imprint of higher energetic protons. The rotation (counter-clockwise direction) increases towards lower energies and the lowest energetic protons already passed their focal position. Therefore, the imprint in the RCF is flipped in the first layer. Concerning the transport efficiency, the maximum capture angle of the solenoid at this position has to be taken into account. While the initial beam shows a half opening angle of 350 mrad for 10 MeV protons,

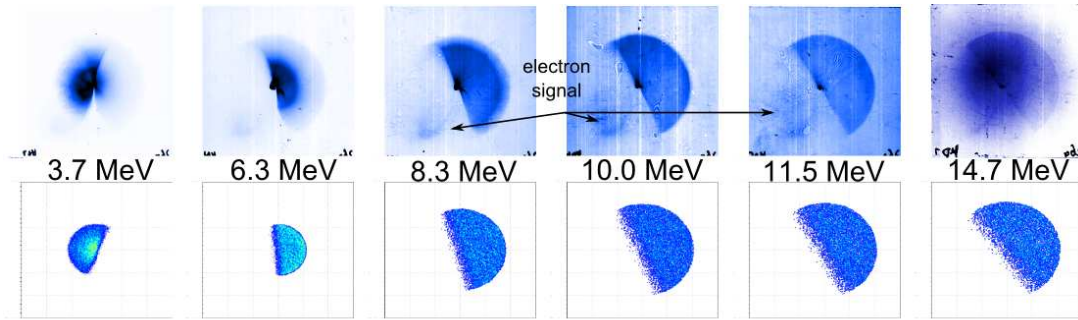


Figure 3.7: Proton imprint in the RCF stack at 368 mm behind the source: experimental (upper) and simulation (lower sequence) results. In both cases the size of a single film is $60 \times 60 \text{ mm}^2$. A central intensity peak throughout the higher energies is observed. Additionally, an electron signal can be seen in the experimental data in the lower left quarter.

the solenoid is only able to capture particles with less than 100 mrad half opening angle. However, the gaussian-like transverse beam profile results in a higher particle density in the center thus improving the situation. Our measurements show up to 34% transmitted protons, which is quantitatively 1.1×10^9 out of the initial 3.2×10^9 protons in the energy interval of $(10 \pm 0.5) \text{ MeV}$ for the shot shown in figure 3.7.

3.4.3 The diamond detector as complementary diagnostic

Transporting the beam away from the laser matter interaction point enables again the use of electrical detectors to some extent. In this case, a precise time-of-flight (ToF) measurement is performed with a $20 \mu\text{m}$ thin diamond detector as complementary detection method at distances $>2 \text{ m}$ from the source. Four equal $4 \times 4 \text{ mm}^2$ diamond segments form a $8 \times 8 \text{ mm}^2$ detection area. All segments are metallized and a potential of 10V is applied (via bias tees) to efficiently separate and drain free charge carriers, that are excited by ions passing through. Monitoring the voltage at an oscilloscope therefore records the temporal profile of the passing ion bunch and translation into the spectrum via ToF is possible, as all ions can be assumed to start at the same time from the laser target; the duration of the acceleration process (in the order of 1 ps) can be neglected.

The diamond itself shows good qualities as ion detector due to its high damage threshold, linear response and short time resolution. A detailed discussion of such diamond detectors for ion detection can be found in [Cayzac, 2009] and a similar detector is used in [Cayzac et al., 2013].

The diamond detector needs shielding against background radiation; in this case a $20 \mu\text{m}$ thin copper foil is placed in front, which causes a resulting low energy cut-off for detectable particle energies. Also, specially shielded cables are used for the signal transport.

3.4.4 Full bunch characterization within the beamline

After verification of the principle transport properties of the solenoid, the focusing is investigated. A first diagnostic possibility behind the target chamber and within the beamline at a distance of 1.07 m to the source was used for proton bunch detection with RCF stacks when applying different focusing field strengths. While a maximum field of 7.8 T resulted in focusing 9.4 MeV protons at this position, a 5.2 T field focuses 5 MeV protons.

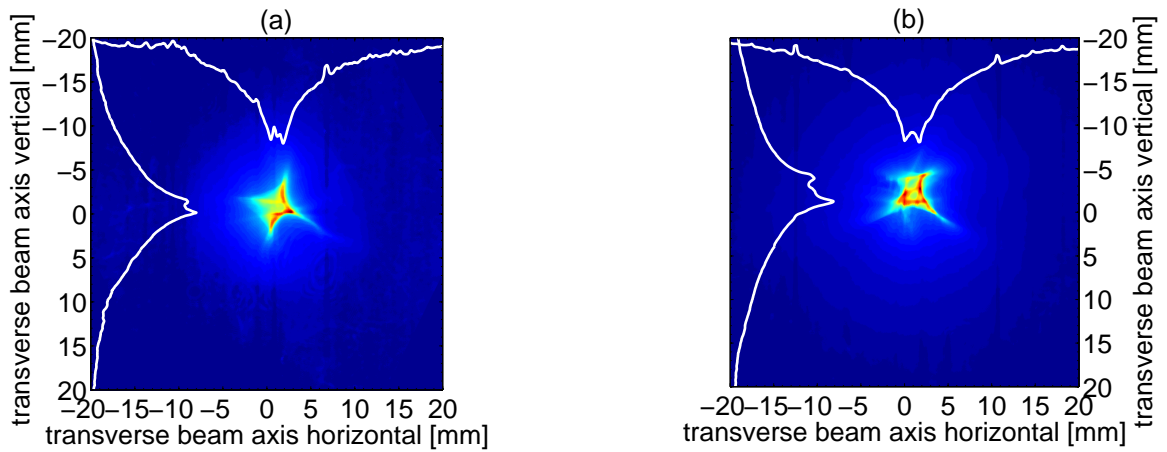


Figure 3.8: Measured transverse beam profile of the focused energy (a) 9.4 MeV and (b) 5 MeV at a distance to the source of 1.07 m. In both cases the spot was around 5 mm in diameter and contained (a) 4×10^8 and (b) 1.6×10^9 protons.

From the RCFs the transverse beam profile and particle numbers of the focal energy is obtained, see figure 3.8. In both cases, about 10^9 protons are observed in a square-like focal spot of $5 \times 5 \text{ mm}^2$. This focal shape and the somewhat hollow particle distribution within the focus are caused by different effects and will be discussed more detailed later.

The position of primary interest is between 2 and 2.55 m distance to source, as there the cavity will be placed for the following phase rotation experiments. Here, a full spatial, spectral and temporal bunch characterization is performed. This is accomplished via combined measurements with full aperture RCF stacks only or the diamond detector in combination with sub-aperture size RCFs (see figure 3.6). With the solenoid at 7.35 T and focusing 9.4 MeV protons at 2.2 m, again the RCFs yield the information about transverse beam profile and absolute particle numbers. Compared to the steeper focusing shown before, an expected increase in focal spot size is observed.

A first step in understanding the transverse focus profile is accomplished by a more detailed simulation of the the coil. Modelling the exact wire arrangement and therefore taking into account the occurring irregularities revealed a partial explanation: On the one hand, for technical reasons, the wires cannot be arranged parallel but show an intrinsic screw (due to the helical wiring in reality). Also, an asymmetry occurs at each position where the wire is lead to the next layer of windings. On the other hand, the connectors need to be inserted correctly, causing an additional asymmetry. As a consequence, higher order field aberrations are observed, as already mentioned in [Burriss-Mog et al., 2011], dominated by an astigmatic behavior. In the RCFs this spatially distinct focusing in the two transverse beam directions is integrated and leads to a cross-like shape. A simulation of first tracking protons through this most realistic magnetic field and then depositing their energy in the RCF stack shows exactly this effect. The result is illustrated in figure 3.9 in comparison with the experiment. The depleted central region of the focus, however, has to be caused by another effect and will be discussed later (section 3.5).

The temporal and spectral shape of the bunch at 2.2 m is measured precisely with the diamond detector, which is thin enough to allow for a simultaneous RCF measurement of the bunch after passing the diamond. The normalized results of both detection systems and comparative expectations from the particle tracking simulations are shown in figure 3.10. The first observation with the diamond detector is

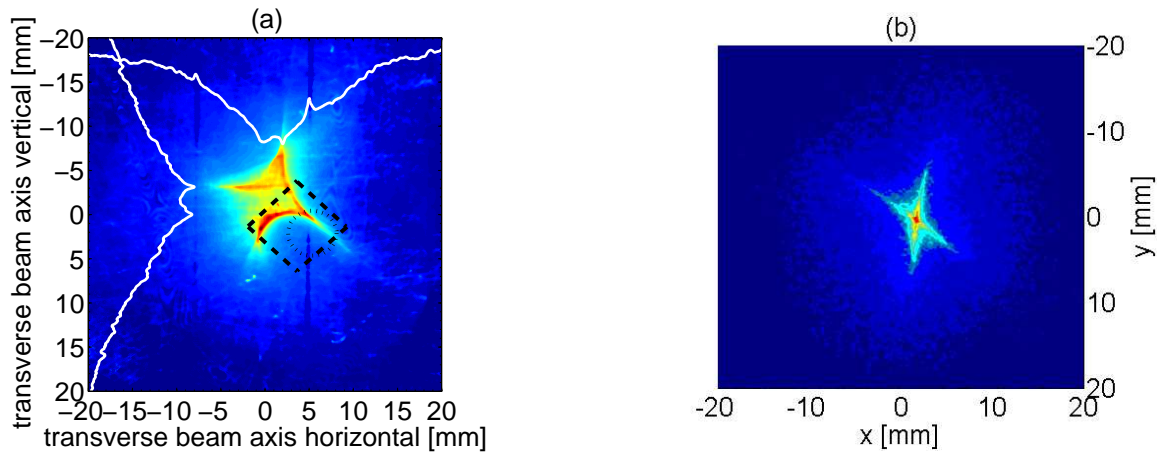


Figure 3.9: (a) Measured transverse focus profile of 9.4 MeV protons behind the solenoid at 2.12 m distance to source. The focus is about 10 mm in diameter and contains 5×10^8 protons. (b) Simulated focal spot in the corresponding RCF layer, using a realistic wire assembly for the solenoid coil, which results in an observable astigmatism of the ion lens. Additionally indicated are the position of the diamond detector (dashed black square) and the optional 5 mm aperture (dashed black circle) relative to the proton beam, which was used for some measurements.

the verification of the correct focusing. For the same test cases as with the full RCF stacks (5 MeV and 9.4 MeV) the central maximum matches the focused proton energies. Comparing the results of the diamond detector to the particle tracking simulations, a much broader spectrum is observed than expected. The experimental findings, however, can be verified by the comparative RCF measurements. They also show an only slow intensity decrease towards higher energies and are in very good agreement with the diamond detector, see figure 3.10. A better interpretation of this finding is possible when analysing the behavior of the higher energetic protons at the full transverse beam size instead of only a sub-aperture size (as inevitable when using the diamond detector with a maximum detection area of $8 \times 8 \text{ mm}^2$). Measurements with (easily large enough sized) RCF stacks reveal a focal feature throughout all detected higher energies, shown in figure 3.11. Identification of a similar, but weaker feature towards the lower energetic protons, as one might expect from the also observed broadening towards lower energies in the diamond detector signal, is hardly possible with the RCF technique, as this feature would vanish in the dominating overlapping imprint of the focal energy in the first films.

The filamented focal shape is reproduced in every energy, see 3.11, but cannot originate from the magnetic field of the solenoid, as these energies are (globally) diverging and not focused. A detailed discussion of this specific experimental finding will be presented in the following section.

3.5 Discussion of the results

An unexpectedly high energy spread of the transported bunch has been measured. Especially the still large particle numbers at the high energy slope and the occurrence of a focus-like feature throughout all energies above the focal energy are surprising. These findings cannot originate from the magnetic field of the solenoid, as they show achromatic qualities. Furthermore, the field distribution has been affirmed by detailed measurements and simulations (see section 3.3) and correct transport and focusing is observed in general (see section 3.4.2 and 3.4.4).

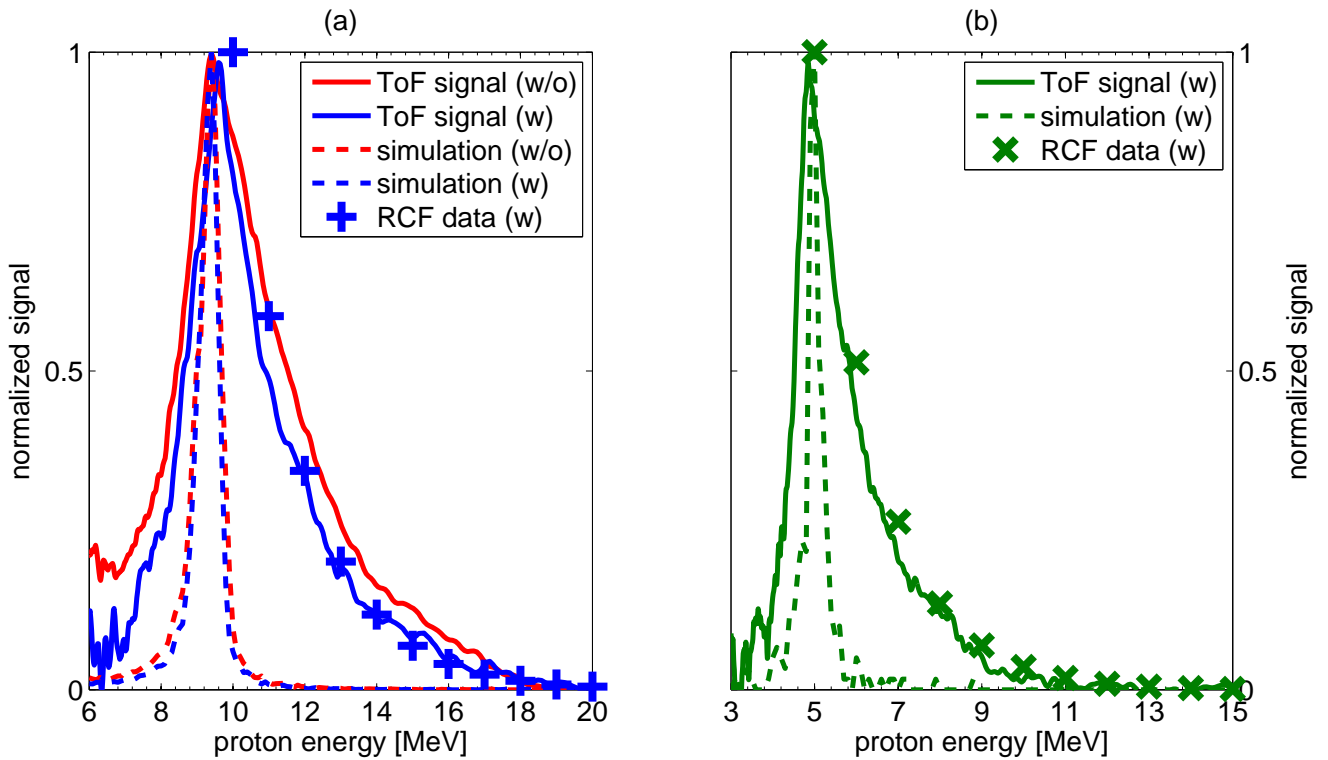


Figure 3.10: Normalized time-of-flight results of the diamond detector (at 2.2 m from source) for three different shots: (a) Focusing of 9.4 MeV protons with (w) and without (w/o) a 5 mm pinhole at 2.12 m and (b) focusing of 5 MeV, also using the pinhole. The dashed lines are the corresponding expected spectra from simulations and the crosses mark the exponential decaying spectrum for the high energies obtained from the RCF data.

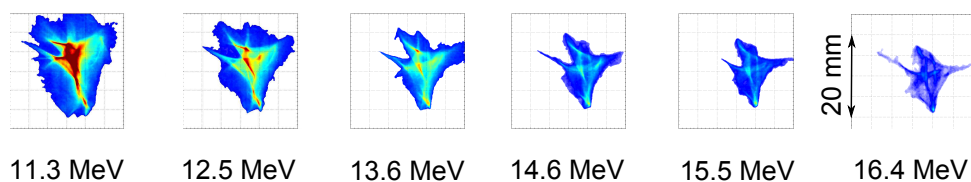


Figure 3.11: Proton imprint (in measures of deposited energy) in the RCF layers for energies larger than the focused one with corresponding Bragg energies. Contrary to the expectations, a focus-like, filamentated feature is still detectable up to the last layer.

A possible explanation can be found by including the effect of the co-moving (keV-range) electrons, that are tightly focused on-axis within the solenoid. The comparative simulation studies neglect the electrons and space charge effects entirely and consequently cannot predict effects caused by them. In the following, the experimental results will be reviewed, looking for indications to support the hypothesis of the co-moving electrons to be responsible for the observations. Therefore, they are compared to previous detailed simulation studies including electrons and space charge effects [Nürnberg, 2010] and additional quasi-static simulations. A full dynamic simulation study of the present experiment is current work in progress³ and has not been finished by the time this thesis is written.

3.5.1 Space-charge effects and earlier simulation studies

Contrary to an ion beam from a conventional accelerator, the laser-accelerated particle beam is a quasi-neutrally expanding plasma. However, the exact characteristics of the space-charge compensating electrons, that are *co-moving* with the ions after the acceleration phase, are experimentally still not investigated sufficiently.

The *hot* electrons as the driving force of the ion acceleration are well characterized and measured (see section 2.1.4). They show an exponential distribution and energies up to several MeVs. Those fast electrons are moving with a velocity close to the speed of light and will escape from the accelerated protons, which have also MeV energies, but due to their higher mass much slower velocities (just a few percent of c). Consequently, the *hot* electrons cannot provide the space charge compensation within the quasi-neutral plasma expansion. However, the validity of the quasi-neutrality assumption is well modeled in simulations (e.g. [Mora, 2003]) and can be deduced from the experimental observations, as with the measured source size the ion bunch would Coulomb explode without space-charge compensation. Therefore, electrons with the same velocity as the protons have to be present. These are the so-called *co-moving* electrons. Their energy can be calculated to be in the region of several keVs. In an experimental setup, these energies are difficult to access and no results of a full spectral and quantitative measurement could be found published.

A common conclusion is that the co-moving electrons are well approximated with the spectral shape and absolute numbers of the proton distribution, just scaling the energy to obtain exactly *co-moving* electrons ($v_e = v_p$). This is also the way of inserting the electrons in the simulation studies to which will be referred to in this section: In a previous PhD thesis [Nürnberg, 2010], simulations of the propagation of a quasi-neutral TNSA proton beam through a solenoid field have been performed with the *WarpRZ* code, which is capable of simulating multi-species beam propagation including external and self-generated fields, thus space-charge effects.

Including the electrons in these simulations leads to two immediate observations: First, a large part of the electrons (2/3 in the case at hand) is reflected at the solenoid entrance by the magnetic mirror effect. Second, the electrons get tightly focused to densities, at which the Coulomb repulsion due to their self-fields has a strong effect and accelerates electrons to much higher energies; behind the solenoid, electrons with energies up to 250 keV are observed in these simulations, although the initial cut-off energy has been at 12.5 keV (see figure 3.12).

³ D. Schumacher, private communication

The dynamics of the electrons may well have an effect on the proton distribution, as their on-axis concentration results in a negative potential. This potential affects only near-axis protons, while the potential is screened for protons on larger radii. The simulations [Nürnberg, 2010] showed:

The negative potential at the solenoid axis attracts near-axis protons. They experience a resulting force towards the beam axis. The effect is observed at 132 mm behind the solenoid in the (virtual) RCF layers by a central intensity peak throughout the stack instead of a flat transverse intensity profile of the beam ([Nürnberg, 2010], figure 6.7).

These simulations covered only short distances behind the solenoid as in the comparative experiments and large deviations in the proton spectra are not to be expected, as still most particles are propagating within the detection area of the RCF and the electrons mainly influence the trajectories of the protons and only slightly their energies. However, propagating the beam over larger distances (few meters) and keeping the typical detection area of the RCFs (several cm^2) results in all non-axis-near particles to be lost for the detector. With the higher on-axis concentration caused by the electrons within the solenoid, this now leads to an observable broader recorded spectrum than without electrons.

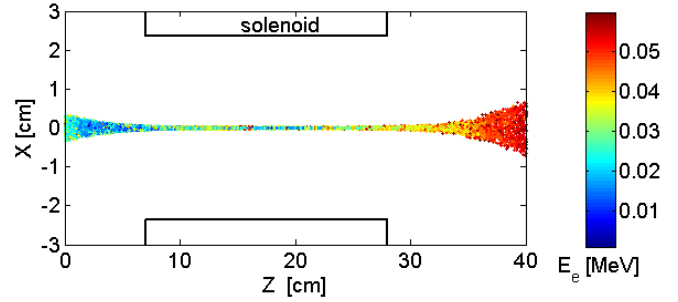


Figure 3.12: Results of the *WarpRZ* simulations from [Nürnberg, 2010]. The (initially) co-moving electrons are tightly focused on axis within the solenoid and the larger part is even reflected by the field. The on-axis accumulation causes a high negative potential and electrons are even accelerated to several 10s of keV by electron-electron repulsion.

3.5.2 Interpretation of the experimental results

A first hint of an additional focusing force inside the solenoid is observed already in figure 3.7 (full RCF stack only a few cm behind the solenoid): Instead of a flat transverse beam intensity profile in the RCFs behind the solenoid, a central intensity peak is visible throughout all energies, as observed in a similar setup in earlier experiments.

Moving to larger distances, a broadened spectrum is observed as a consequence. A quasi-static study with *CST particle studio* is performed to obtain comparative results for the larger distances probed in this thesis and analyze the expected behavior of the beam caused by the influence of the co-moving electrons. For this, a simplifying assumption is made: The electrons, tightly focused inside the solenoid and again rapidly defocused behind the solenoid, are represented by a static negative on-axis potential inside the solenoid, which acts on the passing protons. The gyro radius of the keV electrons is of the order of $50 \mu\text{m}$, which justifies a very localized on-axis potential. All the electrons are assumed to be within a cylinder with a radius of the gyro radius of the electrons. First effects of this negative potential on the passing MeV protons are observed for choosing a value of a few kV for this potential. This allows for an estimate of the necessary electron numbers. Choosing the model of a cylinder condensator for the electron cylinder inside the stainless steel beam tube, which covers the inner side of the solenoid, one can estimate the electron number to create a potential of $U=5 \text{ kV}$ by $N_e = \frac{CU}{e} = \frac{2\pi\epsilon_0 \times l \times U}{e \times \ln(R/r)}$ with the capacity

$C = 2\pi\epsilon_0 \frac{l}{\ln(R/r)}$ and $l=150$ mm the length of the solenoid, $r=50$ μm the small and $R=2$ cm the large radius of the cylinder condenser. The resulting N_e is of the order of 4×10^{10} , which therefore serves as minimum threshold for the electron number to create a large enough potential for an observable effect. It also matches very well the real electron numbers, estimated by the proton numbers to be in the range of 10^{11} to 10^{12} (substracting up to 2/3 of this value, which get lost by the magnetic mirror effect). Although of course the real process is highly dynamic, the simulation setup of tracking protons through the solenoid field with the additional static negative potential on axis yields a good approximation and comparative results are obtained regarding the focal spot profile and the occurrence of focal features throughout higher proton energies, which lead to the observed broad spectral shape.

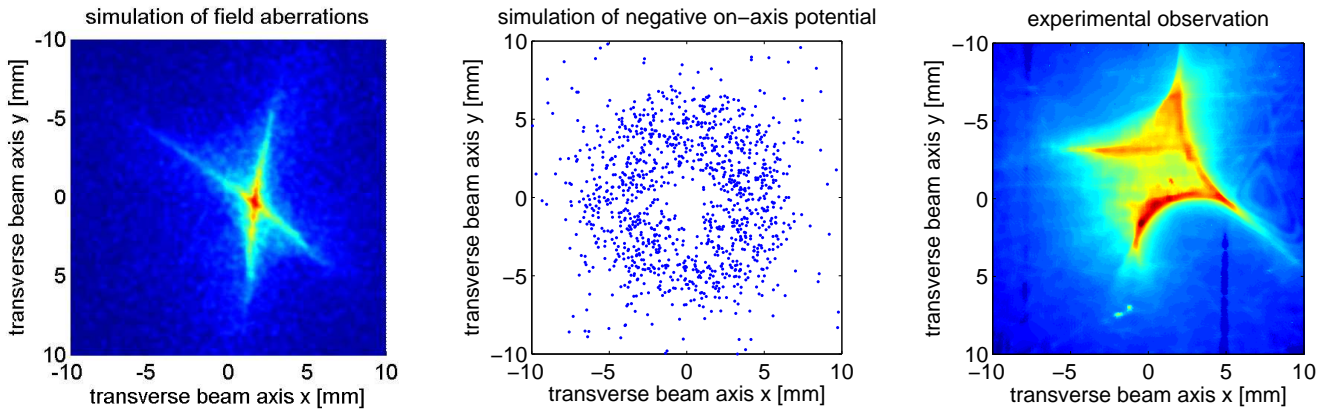


Figure 3.13: The measured transverse focal beam profile is explained by two effects: First, a detailed simulation of the wire arrangement of the solenoid revealed aberrations of the focusing magnetic field (dominated by an astigmatism). Consequently, the integrated deposited energy profile within the RCF shows a cross-like shape in a simple particle tracking simulation (left picture). Tracking the protons through an ideal magnetic field and adding a negative on-axis potential to represent the effect of the co-moving electrons, results in a ring-like intensity profile (middle picture). The measured focal spot profile (right picture) can be understood as a combination of both effects.

First, the transverse focal spot size is discussed. The *TraceWin* simulations use an ideal magnetic field and predict a round focal spot. Taking into account the field aberrations caused by the realistic wire arrangement of the coil, a cross-like focus is to be expected, still with a centered maximum intensity region; instead, in the experiment the central spot of the focus is depleted (compare figure 3.9). Such a deflection of the protons from the center at this position is also observed when adding the negative potential (in this case with $U=5$ kV) at the solenoid axis. Near-axis protons experience an additional focusing field and are focused earlier, thus already defocusing and leaving a hollow region in the beam center at the focal position of the protons that do not experience this additional field. The measured focal spot profile therefore can be explained as a superposition of both effects, the field aberrations of the coil and the presence of the co-moving electrons, as illustrated in figure 3.13.

Similarly, the observed proton focal features throughout higher energies can be created by a negative on-axis potential. In this case, however, a higher potential is necessary to reproduce the experimental findings (for the simulation shown later: $U=300$ kV). This again is a clear hint for the dynamic nature of this potential. Still, the increased necessary potential (i.e. higher electron numbers) is in a realistic

parameter region. For energies near to the focal energy, still the full beam can be recorded with the RCF films. In this chapter, the main focal energy is 9.4 MeV. Figure 3.14 shows the imprint in the RCF films for an energy slightly higher (10.1 MeV and 11.3 MeV). The central intensity aggregation clearly is gathered from the near-axis sub-population of the beam, while the outer part of the beam is not affected and forms a surrounding ring shape with a depleted region between the focal feature and the outer particles.

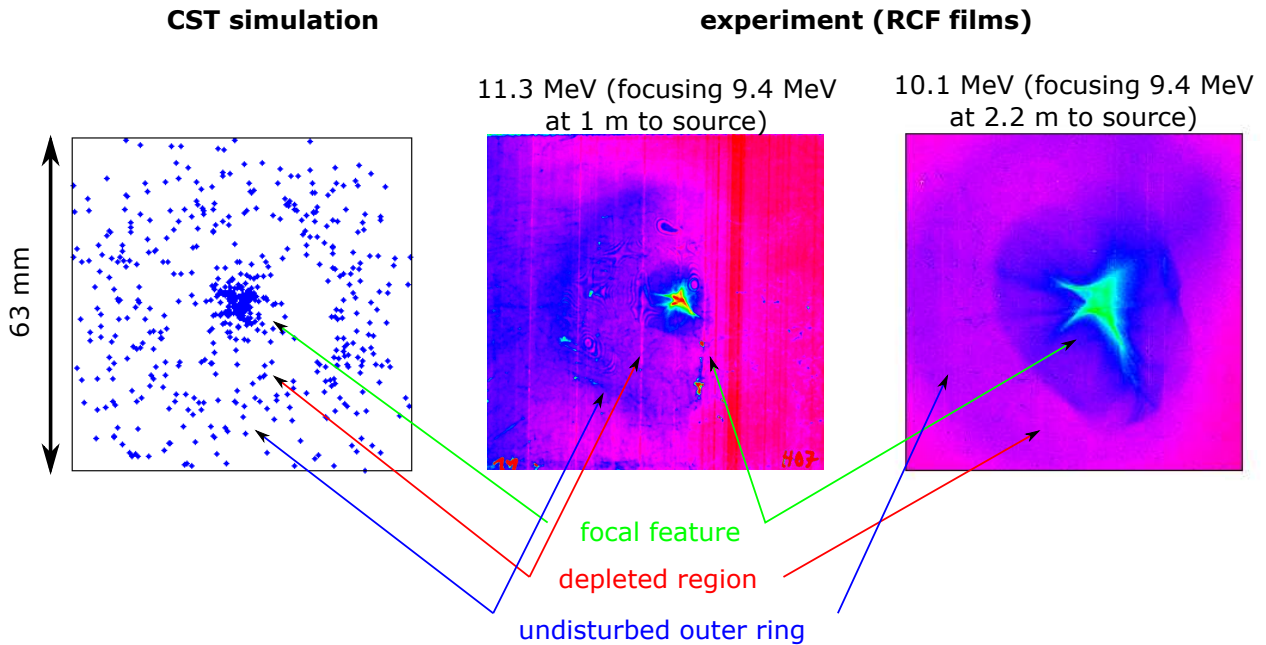


Figure 3.14: Near-axis protons experience the attracting force of the negative on-axis potential caused by the electrons within the solenoid. This additional focusing results in the experimentally observed focal features at higher proton energies. Consequently, these protons, aggregated on small radii, are missing at middle radii while the larger radii are unaffected. The left picture shows a simulation (ideally symmetric field distribution from CST), the middle a measurement of the 11.3 MeV proton population at the focal position of 9.4 MeV at 1 m and the right a measurement of the 10.1 MeV proton population at the focal position of 9.4 MeV at 2.2 m.

Ring features within the transverse proton beam profile have also already been observed in experiments with the solenoid and explained by the presence of the co-moving electrons (compare [Nürnberg, 2010], figure 6.8). More details can be found there and additional investigations are current work in progress. Results of this chapter on transport and focusing of laser accelerated protons are published in [Busold et al., 2013].

3.6 Measuring the co-moving electrons

Quantitative measurements of the co-moving electrons are not published up to now, but are essential for the correct modeling of the realistic transport process. A first approach on measuring these low energetic electrons was done within a previous thesis [Busold, 2010], in which the first experimental application of the developed magnetic spectrometer at the *Callisto* laser at the *Jupiter Laser Facility* (JLF, USA) in 2010 is described. Further improvements on the spectrometer and the data analysis methods have been taken

in the following and in a campaign at PHELIX new measurements could be performed in the scope of the thesis at hand. In this section, the spectrometer will be introduced and the obtained new experimental data presented.

3.6.1 The electron spectrometer

The spectrometer for co-moving electrons consists basically of an electro-magnet (for an adjustable magnetic field strength) and an image plate detector (IP, e.g. [Izumi et al., 2006]). A pinhole at the entrance defines the energy resolution and sufficient shielding is applied in the front to suppress the radiation background, which originates from the laser matter interaction point (laser target). The shielding is a compound of 10 mm plastic (PE), 10 mm aluminium and 50 mm lead. The open aperture through the shielding is 2 mm.

The IP is from *Agfa* and of the type *MD4.0*. It has no protection coating on top of the active layer. This is necessary, because the co-moving electrons are expected in the energy range of 1...30 keV and at these low energies the electrons are not able to penetrate the protection layer. Finally the whole spectrometer has an aluminium housing to prevent ambient light to reach the IP after irradiation, as this would erase the detector. A sketch of the spectrometer is shown in figure 3.15.

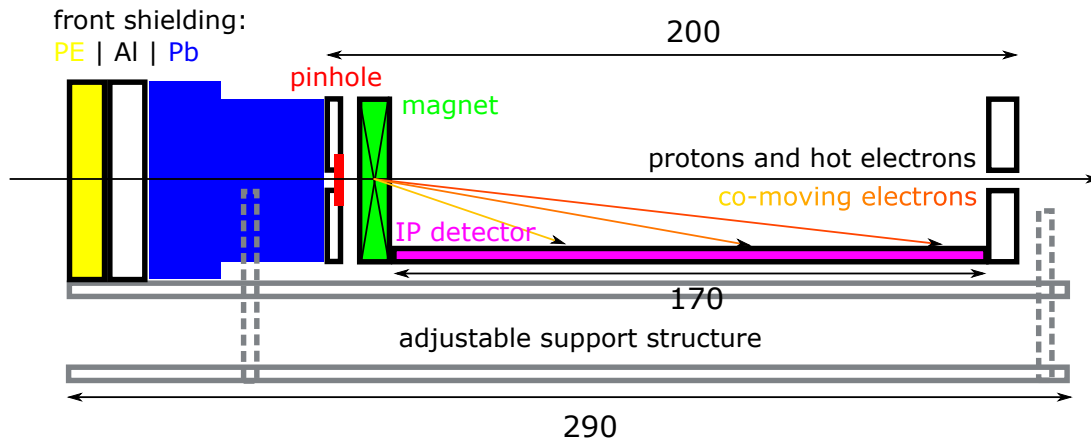


Figure 3.15: Sketch of the spectrometer for co-moving electrons. The plasma propagates through the shielding first (2 mm open aperture) and then a narrow pinhole aperture can be applied to adjust the energy resolution. In the transverse magnetic field of the electro magnet, the keV electrons are dispersed and deflected downwards onto the IP detector, while the protons and energetic MeV electrons experience a neglectable deflection and exit the spectrometer at the back side (lengths are given in mm).

The electro magnet as the dispersive element within the spectrometer has been replaced compared to the version described in [Busold, 2010]. The new magnet has additional iron apertures to reduce the fringe field regions. As the deflection of a charged particle in a magnetic field is proportional to $\int B(s)ds$, the field distribution can be replaced by a constant magnetic field B_0 over a defined length s_0 with $B_0 \times s_0 = \int B(s)ds$. This allows for an analytical solution of the particle tracking in the spectrometer. For the length of the substitutional magnetic field, $s_0 = 1$ cm is chosen. This is the (outer) distance of

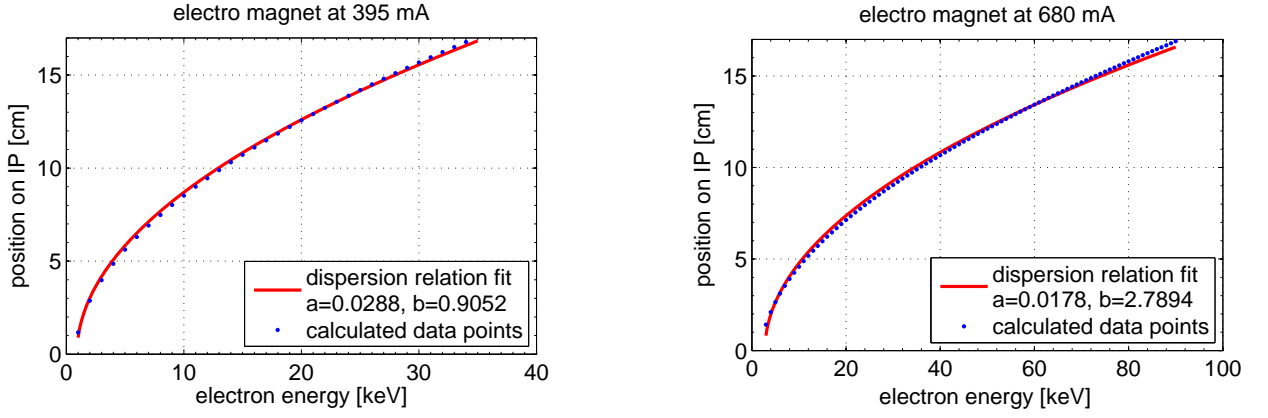


Figure 3.16: Dispersion relation of the electron spectrometer for two operation modes: at a current of 395 mA (left) and 680 mA (right). The fit parameters are according to equation 3.21.

the apertures of the magnet and no field could be measured beyond this range. B_0 [T] is then a linear function of the applied current I [A]:

$$B_0(I) = 0.021 \text{ T/A} \times I + 0.0008 \text{ T} \quad (3.20)$$

Given this substitutional field distribution and the detector geometry, the position of incidence on the IP of individual electrons can now be calculated analytically in dependency of their energy. This is done for both different constant currents ($I_1=395$ mA and $I_2=680$ mA) that were used in the experimental campaign. A continuous dispersion relation between detection position on the detector d [m] and the electron energy E [keV] can be fitted via

$$d(E) = a \times \sqrt{E - b} \quad (3.21)$$

with the fit parameters a and b . This dispersion relation is used for the further analysis; it is illustrated for both cases in figure 3.16 with the corresponding fit parameters given.

IPs are commonly used as detectors and several calibrations for electrons are published [Li et al., 2005, Chen et al., 2008]. However, a calibration for the relevant energy interval of the co-moving electrons (1...30 keV) has not been available and was performed separately at two electron gun systems at GSI Darmstadt and the IAP of Frankfurt university. Details of the calibration can be found in [Busold, 2010]. For the energy range between 30 and 100 keV, the calibration curve is interpolated by a linear dependency towards the available published data starting from 50 keV [Li et al., 2005]. The actually applied sensitivity $S(E)$ [PSL/electron] is depending on the electron energy E [keV] and defined in two sections:

$$S(E)_{E \leq 10 \text{ keV}} = -5.6 \cdot 10^{-7} \frac{\text{PSL}}{\text{keV}^3} \times E^3 + 2.9 \cdot 10^{-5} \frac{\text{PSL}}{\text{keV}^2} \times E^2 - 2.7 \cdot 10^{-5} \frac{\text{PSL}}{\text{keV}^1} \times E \quad (3.22)$$

$$S(E)_{E > 10 \text{ keV}} = 0.0004 \frac{\text{PSL}}{\text{keV}} \times E - 0.002 \text{ PSL} \quad (3.23)$$

The unit PSL denotes the quantity of *photo stimulated luminescence*, which is the equivalent to the light output from a scintillator (only that the light output is not spontaneous but stimulated within the special IP scanner, for further details see e.g. [Otten, 2007, Meadowcroft et al., 2008]). Figure 3.17 shows the calibration data and fit curves, as well as the indicated calibration results from another publication, that has been used to extrapolate the calibration up to 100 keV electron energy.

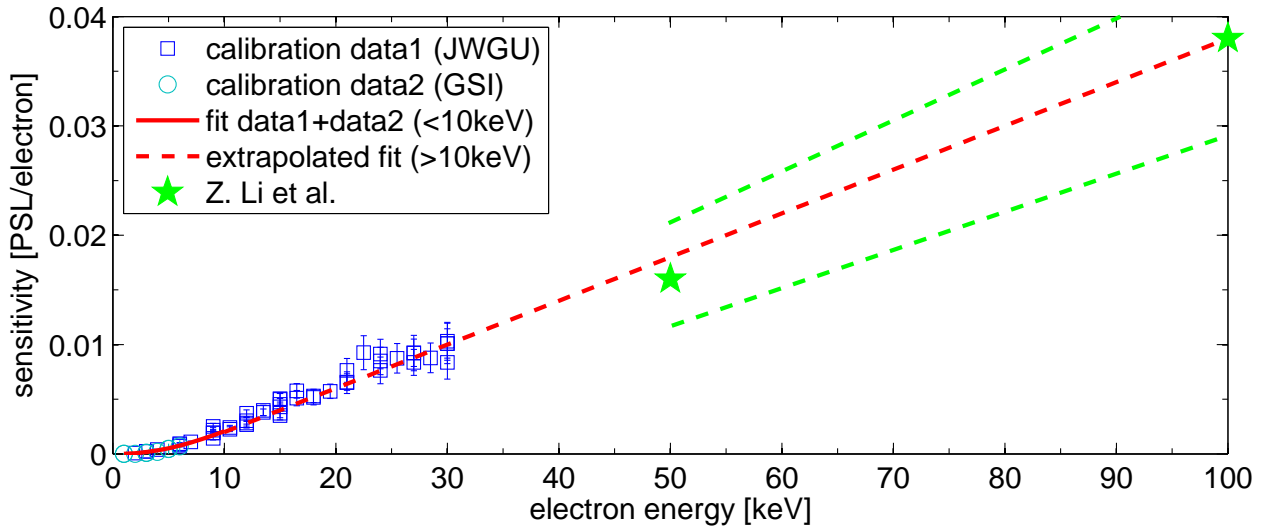


Figure 3.17: Shown are the obtained calibration results from two calibration experiments at different electron gun systems and the used (sectionwise defined) calibration curve, which is extrapolated linearly to existing published experimental data (green stars, including error range: green dashed lines). However, the relevant energies for *co-moving* electrons are between 1 and 15 keV electron energy for the expected proton spectra with energies up to 30 MeV. In this region, the two independent own calibration data (data1 and data2) are very precise and show very good agreement.

This calibration for the energies >30 keV may have large errorbars and one should keep in mind that it was performed with a slightly different IP type (Fuji BAS SR-2025), but on the one hand the region of interest (electrons with velocity $v_e = v_p$) is within the well-calibrated area $E_e < 30$ keV, and on the other hand a linear response function is to be expected for the IPs and this tendency can clearly be observed from energies > 10 keV on. Only towards lowest energies the electron penetration depth becomes critically low and the excitation process breaks down.

3.6.2 Experimental results

Electrons with energies between 2 and 90 keV were detected during an experimental campaign at the PHELIX laser (experimental area: PHELIX laser hall). Figure 3.18 illustrates the experimental setup. The typical parameters for the conducted TNSA experiments were: flat gold foils with a thicknesses of 5 or 10 μm as targets and 100 J of laser energy in 650 fs focused to intensities $>10^{19}$ W/cm². The proton cut-off energy was measured around 25 MeV and the typical exponential shape of the spectrum observed.

Due to the high sensitivity of keV electrons to deflecting fields, even small effects are sufficient to broaden the electron trace transversely on the detector. Although this broadening becomes less towards higher energies, the independent identification of electron trace and background radiation signals on the detector is hardly possible. Thus, the background subtraction represents the dominating error with respect to the electron numbers. An exemplary detector image is shown in figure 3.19 and the analysis method is described in the following.

The detector IP has a width (transverse) of 5 cm and a length (longitudinal) of 17 cm and is scanned with a *FLA 7000* IP scanner (specific scanner settings: resolution of $25 \mu\text{m}/\text{px}$ at a sensitivity of 10^4 and a latitude of 5). After digitizing, the data is converted to the IP-typical units of PSL and the trace analysis performed with a custom MATLAB routine.

A crucial point in the analysis is the background subtraction. No homogenous background can be assumed and thus the background is determined and subtracted for each energy separately, i.e. for each column of the detector image.

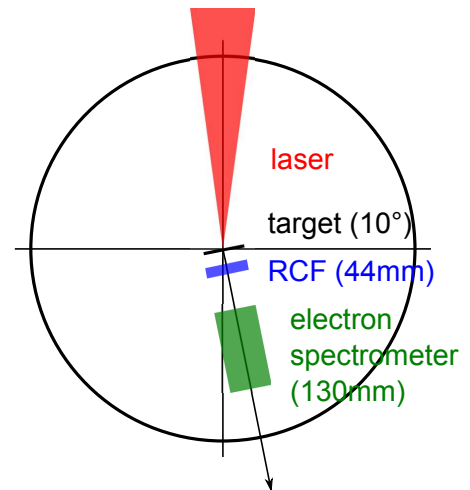


Figure 3.18: Experimental setup in the target chamber at the PHELIX laser hall.

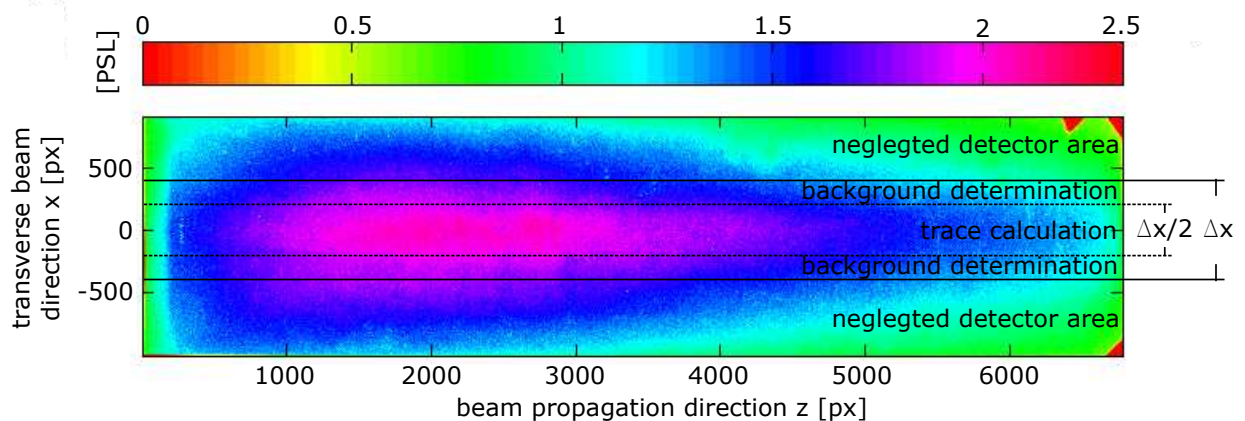


Figure 3.19: Detector image of a recorded electron trace during an experimental campaign at PHELIX. The electrons are dispersed in the magnetic field (left of the detector) and then deflected along their propagation direction z onto the detector, depending on their energy. Also indicated is the analysis method (details in text).

Such an image is exemplarily shown in figure 3.19 and the method indicated: Instead of the whole IP only a central part is used for the analysis (Δx). Within this part, again only the central part ($\Delta x/2$) is used for the trace calculation and the outer parts for the background determination (which is done for each column by the mean value of the background area). Choosing larger values for Δx results in

systematically higher electron numbers and the choice of Δx clearly dominates the overall error of the measurement. As the here chosen value is already quite small, the later given error is asymmetric with a higher uncertainty towards larger electron numbers.

In the experiment, the magnet was used in two different modes: First to measure electrons between 2 and 35 keV and second for the interval 5 to 90 keV. A RCF stack was placed in front of the spectrometer to obtain the proton spectrum and a small hole in the RCF allowed for a sub-aperture of the beam to enter the electron spectrometer. The experimental results are shown in figure 3.20. The proton spectrum is shown for comparison (scaled to the sub-aperture). Their spectrum was comparable for each shot, therefore only one spectrum is depicted - graph (f) - for a clearer view on the data.

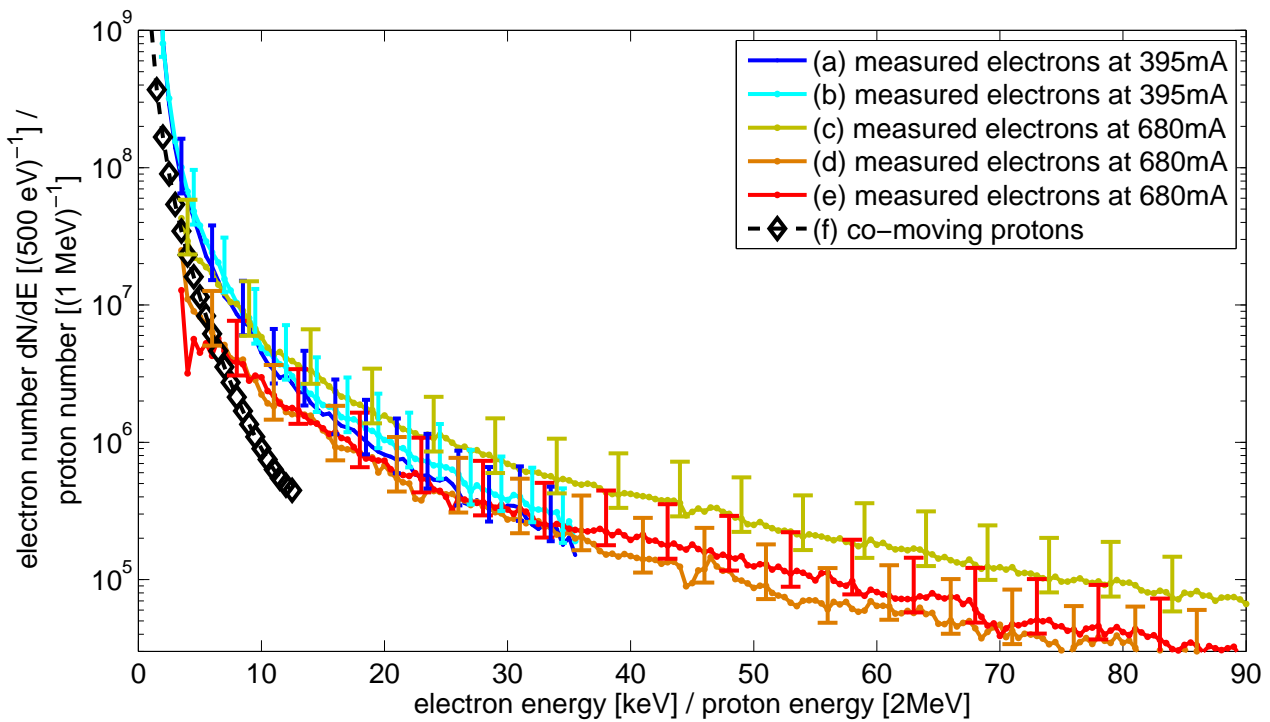


Figure 3.20: Measured low energetic electron spectra via two operation modes of the electron spectrometer: weak magnetic field, thus lower deflection and mapping only energies up to 35 keV on the detector (a)-(b); and higher magnetic field for energies up to 90 keV (c)-(e). Also indicated is the spectral distribution of the protons that entered the electron spectrometer (derived from the RCF measurements and scaled to the solid angle coverage of the electron spectrometer for comparison). For the sake of clarity, the errorbars to the electron measurements are indicated only now and then exemplarily.

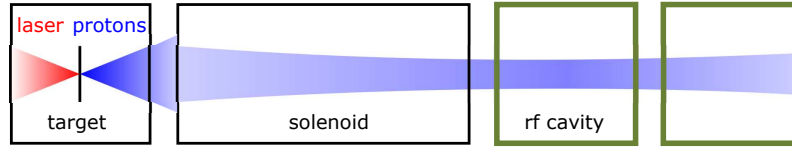
The measurements show larger numbers of electrons than of protons within the expanding plasma. The results of the two different operation modes diverge for lowest energies (<10 keV), but are in good agreement else.

These results represent an important step in measuring the keV electron energy spectrum in a TNSA experiment up to the low end and enables a qualitative view on the electrons, that are accompanying the ion beam. The expansion even seems to be dominated by the electron numbers. Still, one has to keep in mind that also other ion species besides protons are present and the global quasi-neutrality may

be ensured by them.

As the uncertainty in the absolute numbers is dominated by the systematic error in the background subtraction, further investigations are necessary for a concluding statement on the co-moving electrons. However, their presence is clear and special effects as their behavior under the influence of a external solenoidal field have to be taken into account.





4 Phase rotation and energy compression

In the last two chapters, the laser-driven proton source and the available beam transport system (the solenoid) have been described. With both those stages well characterized, now the new key element is added to the beamline: the radiofrequency cavity. In this chapter, radiofrequency cavities for accelerators will be introduced in general, the parameters of the cavity used in the experiments given in specific and comparative simulation studies with *TraceWin* presented. These simulations reveal the necessity of further diagnostic methods, that will be described afterwards. Finally, the results of the first experimental beamtime with the cavity are presented.

4.1 Radiofrequency structures for accelerators

While solenoids (and quadrupoles) address the transverse beam dynamic, adding now a radiofrequency structure (*rf cavity*), that is used for acceleration and phase rotation in conventional accelerators, to the beamline makes the inclusion of the longitudinal dynamics necessary. In this introductory section, the principles of such *rf cavities* and their effect on the beam will be discussed.

Rf cavities are typically built as cylindrical resonant cavities for electro-magnetic waves in the radiofrequency region. For a standing wave to form inside the cavity, the capacity and inductance of the cavity have to be matched to the frequency of the wave to strictly satisfy the resonance condition. For fine adjustment, a motorized plunger inside the cavity is used to tune these values. Electrically, a cavity can be described by a parallel *LCR* circuit with $\omega L = 1/(\omega C)$ at resonance and the full rf power converted into heat via the ohmic losses due to *R*, the so-called shunt impedance, which is connected to the quality factor *Q* of the cavity by

$$Q = R\omega_r C = \frac{R}{\omega_r L} \quad (4.1)$$

with ω_r the resonance frequency. The shunt impedance is also important to calculate the peak voltage within the cavity from the totally applied rf power P_{rf} :

$$U_{peak} = \sqrt{2P_{rf}R_s} \quad (4.2)$$

Cavities have various applications. The most often used one is providing the actual acceleration of the particles in a particle accelerator. Injecting charged particles at the right phase of the rf wave results in the particle experiencing the potential U_{peak} and being accelerated in the electric field. With additional drift tubes for the particles to shield the decelerating field, a particle can effectively be accelerated within the gaps between the drift tubes by the applied electrical potential.

Most important in this is the synchronization of particle injection time and rf phase. Therefore, the injection timing is directly connected to the periodic phase of the rf wave (0 to 360 deg) by the so-called

synchronous phase ϕ_s with $\phi_s=0$ deg representing the injection at the maximum accelerating field. Apart from the acceleration, cavities are used for other applications as well. In general *phase rotation* and in particular *phase focusing* will be addressed here.

4.1.1 Longitudinal emittance

Analog to the definition of a transverse emittance as the covered area of the beam in a transverse phase space diagram ($x - x'$ or $y - y'$), a longitudinal emittance can be defined as the covered area of the beam in longitudinal phase space (most commonly $\Delta E - \phi_s$). This area defines the limit for temporal focusing of the bunch in the same way as the transverse emittance defines the limit for transverse focusing. For laser-accelerated ions both emittances (transverse and longitudinal) show lowest values [Cowan et al., 2004]. The later might be exploited to access shortest bunch durations, thus highest bunch intensities. The mechanism of longitudinal focusing (*phase focusing*) will be explained in the following.

4.1.2 Phase rotation and phase focusing

As it is defined here for a particle to be at synchronous phase $\phi_s=0$ deg for maximum acceleration, then a particle at either 90 or -90 deg passes the gap at zero field and thus is not effected by the rf field at all. Now again, this is true for just one particle. A real bunch instead consists of many particles with varying longitudinal positions within the bunch. Instead of expressing the different longitudinal positions in space, they can be expressed with respect to the rf phase, too. Consequently, the different particles have individually different injection phases and experience a different electric field at the accelerating gap of the cavity.

This defines a longitudinal acceptance of the structure. If the bunch is longitudinally stretched too large, the bunch will get separated. E.g. with a 'width' of the bunch of 180 deg and $\phi_s=90$ deg the particles in the bunch's central region may stay not effected by the rf as they are injected at zero field, but the particles at the front are effectively injected at 0 deg (thus accelerated) and the ones at the back see an effective injection phase of 180 deg (thus deceleration). Starting with a monoenergetic bunch, this drastically increases the energy spread ΔE within the bunch and leads to longitudinal defocusing.

Although in typical accelerators the longitudinal length of a bunch is not that large, still the effect of the individually different injection phases needs to be compensated. In a ring accelerator this is done by not placing the bunch at the optimum acceleration position, but slightly off in a way, that the particles at the front of the bunch see a smaller accelerating field than the ones at the back. By this, the bunch is constantly focused slightly longitudinally and therefore well confined. This effect is called *phase focusing*.

With this effect, the bunch may not only be longitudinally (i.e. also temporally) confined, but also focused in the right configuration. This gives access to highest bunch intensities and can efficiently be exploited in the case of the laser-driven ion bunches (due to their ultra-low longitudinal emittance) by injection at -90 deg synchronous phase and sufficient rf power (compare section 5.3).

The reason why the general process of a working rf cavity is called *phase rotation* is easiest explained when having a look at the longitudinal phase space in the $E-\phi_s$ -diagram, see figure 4.1. The bunch with a length $\Delta\phi_s$ contains particles with energies of $E \pm \Delta E$ (typically denoted on the energy axis is the

relative energy ΔE). The effect of passing the gap of a cavity is in a simplified picture just a shift in energy of each particle according to its synchronous phase. In longitudinal phase space this is identical to a rotation with an angle depending on the applied rf power.

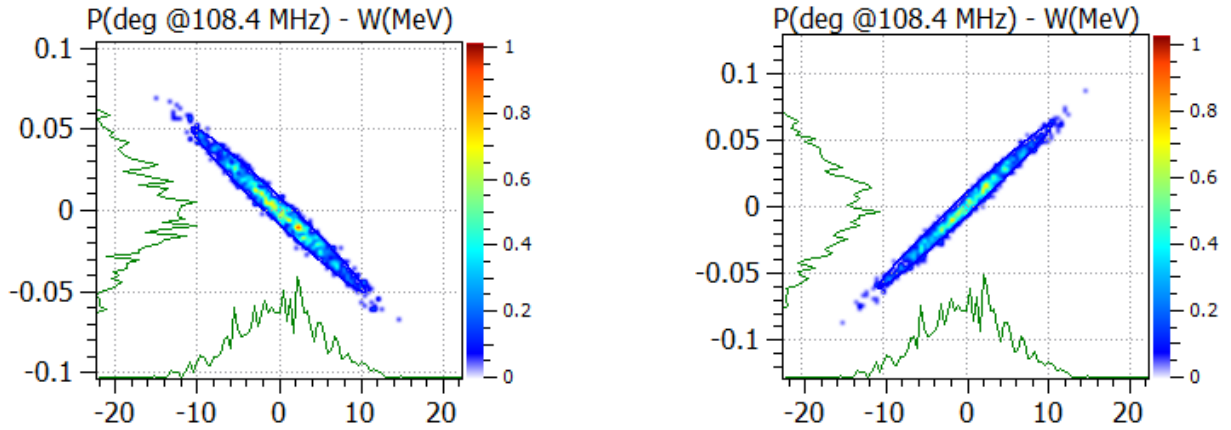


Figure 4.1: Illustration of phase rotation via applied rf in an accelerator cavity. Both pictures show the ion bunch in longitudinal phase space (relative ion energy vs synchronous phase). Left is the bunch before passing the accelerating gap of the cavity with the faster particles (positive rel. energies) at the front of the bunch (negative synch. phase). The bunch then passes the gap at a synchronous phase of -90 deg, thus accelerating the particles at the rear and decelerating the ones at the front. The result is obviously a rotation of the bunch in the longitudinal phase-space-diagram with the rotation angle depending on the rf power, i.e. gap voltage.

4.2 Implementing the radiofrequency cavity into the setup

The radiofrequency (rf) cavity used in this work is a three gap spiral resonator, which was characterized and implemented at the UNILAC before. A full technical description can be found in the corresponding PhD thesis about the earlier application of the cavity [Häuser, 1989]. An overview of the relevant electrical and geometrical data is given in table 4.1.

Spiral resonators allow for a compact design of the cavity. An ion crosses the potential of the electromagnetic wave at each of the three gaps at the same phase (for the design energy of 8 MeV/u; operation at 10 MeV as intended only results in a smaller effective total gap voltage). The gap voltages are ideally related 1:2:1 and with the given parameters of the resonator, a total poten-

electrical data		gemetrical data	
resonance frequency	108.4 MHz	length	550 mm
opt. particle energy	8 MeV/u	diameter	500 mm
shunt impedance	21.8 M Ω /m	gap length of spiral-spiral drift	40 mm
rf power	> 100 kW	gap length of spiral-aperture drift	20 mm
quality factor Q_0	6000	spiral drift tube length	150 mm
plunger		aperture drift tube length	85 mm
frequency shift	1 MHz	open aperture	35 mm

Table 4.1: The technical data of the three gap spiral resonator, taken from [Häuser, 1989].

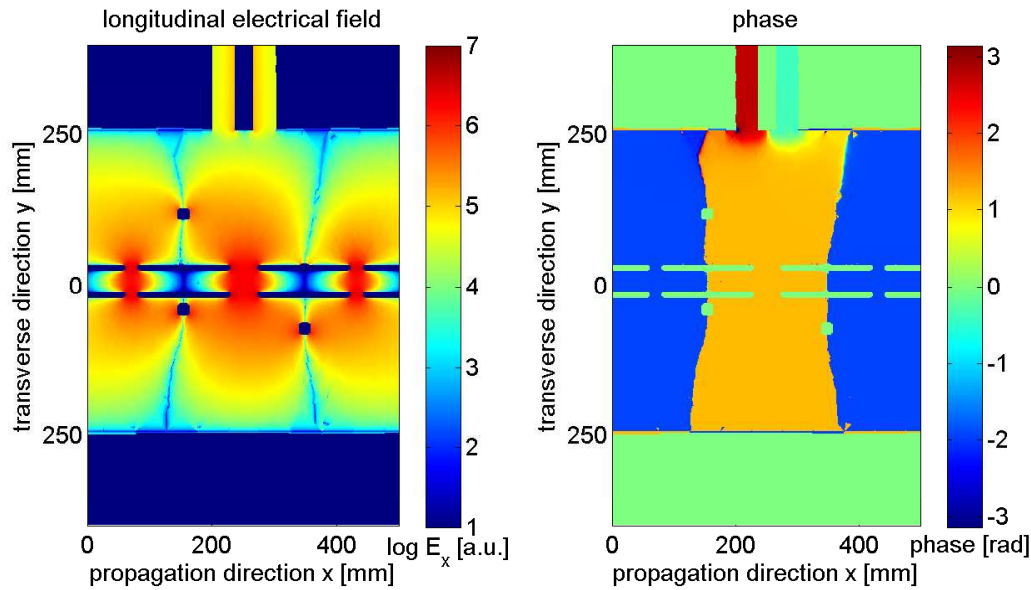


Figure 4.2: The electrical field distribution (in absolute values) and phase (phase shift between gaps: π) within the spiral resonator (courtesy of D. Schumacher).

tial of 1.1 MV can be calculated over all three gaps at a rf input power of 100 kW. A simulation of the cavity (see figure 4.2) shows the electrical field and phase distribution within the resonator. The high gap voltage and input power cause massive x-ray radiation (by interaction with the residual gas, similar to a x-ray tube). Although this radiation becomes less with better vacuum conditions, additional shielding of the cavity is necessary and therefore it is covered by 20 mm of lead. However, the main radiation direction is the beam axis, which obviously cannot be covered. The cavity is consequently operated only when the experimental cave is cleared and no personal access possible.

Phase and amplitude of the rf wave in the cavity are adjustable and in full operation mode all necessary data concerning the rf and the cavity is monitored online during the experiment:

- rf input power
- relative rf amplitude
- relative rf phase

Due to varying thermal conditions, the resonance frequency of the cavity may change slightly; this effect is observed mainly directly after starting the cavity due to the heating of the whole structure until a

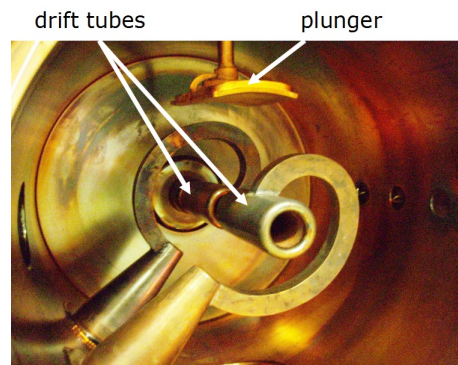


Figure 4.3: Photo of the interior of the cavity.

stable thermal operational state between the rf heating and the water cooling is reached. To compensate for this, a plunger is placed inside the resonator and permits a shift in resonance frequency up to 1 MHz. The plunger is routinely run in automatic mode and keeps the cavity at resonance.

The phase and amplitude measurement is done directly at the cavity. As PHELIX is synchronized to the 108.4 MHz reference signal, this provides for a relative measurement. For the absolute phase, additional measurements are necessary (the later section 4.4 is dedicated to the synchronization in detail).

The rf input power is measured within the GSI's rf system (as well as the possible power backflow, that occurs if the cavity is run not perfectly at resonance). Knowing the shunt impedance and neglecting the possible power backflow, a direct calculation of the gap voltage (see equation 4.2) is possible. However, there are several reasons why the rf input power necessary in the experiments will be of a higher value than the calculated power with the *TraceWin* simulations: the power backflow is ignored, the ideal design energy of the cavity is 8 MeV/u instead of 10 MeV/u (velocity matching of the drift tubes) and general imperfections (e.g. in the geometry) of the cavity and the rf power supply system.

4.3 Experimental setup and comparative beam parameters

For the experiments on phase rotation and energy compression, the rf cavity is added to the beamline at a distance of 2 m to the source and a diagnostic box at 3 m. The solenoid is set to focus 9.6 MeV protons at this later position (7.5 T) to keep the transverse beam size as small as possible at the detection area without additional focusing elements. An overview of the setup is given in figure 4.4.



Figure 4.4: The 150 mm long pulsed solenoid is positioned 80 mm behind the laser target (40 mm from target to the stainless steel vessel surrounding the solenoid) and is typically set to focus 9.6 MeV protons at 3 m. The cavity (550 mm long) starts at 2 m and is followed by a diagnostic box at 3 m, where RCF stacks, the diamond ToF detector and a compact magnetic dipole spectrometer can be placed.

4.3.1 Bunch characterization behind the cavity (no rf operation)

While the principle transport characteristics have been described in chapter 3 already, in this section only the slight modifications of the proton bunch properties due to the different focal position are shown.

First of all, the transverse focal spot size is increased to $15 \times 15 \text{ mm}^2$, as expected with the weaker focusing of the solenoid. The absolute particle numbers are again in access of 10^9 with the known fluctuations up to a factor of 3 in the focal energy interval ($\Delta E = 9.6 \pm 0.5 \text{ MeV}$). Although the observed spectrum is broadened due to space charge effects at the solenoid (see section 3.5), only the particles around the center can be captured within the bunch by the rf and contribute to the final bunch characteristics. The other particles will be caught in satellites (or in general scattered longitudinally) at different energies and ultimately need to be removed. Therefore, an analytical description of only the relevant central part

of the bunch's spectrum is satisfying. As will be shown in the following, this central part is well fitted by a Gaussian-like distribution,

$$\frac{dN}{dE} = \frac{N_0}{E} \times \exp\left(-\frac{(E - E_0)^2}{2\sigma^2}\right), \quad (4.3)$$

with the scaling parameter N_0 , the standard deviation σ and the central energy E_0 . The parameter of interest is the energy spread of the bunch $\Delta E/E_0$ at FWHM, which is connected to the standard deviation by:

$$\Delta E \approx 2.35\sigma \quad (4.4)$$

A reference spectrum is recorded with the diamond detector at 3 m distance to the source when focusing 8.8 MeV protons to this position. Although (solely) these measurements were performed at a different central energy (i.e. operating the solenoid at 7.3 T instead of 7.5 T), they can be used for comparison of the general spectral shape all the same, as there is no significant difference to be expected other than the parameter E_0 being shifted.

From the ToF domain, a bunch length of 8.6 ns at FWHM is obtained. Transformation to energy domain and a fit of the central region with a Gaussian-like distribution function (equation 4.3) results in a fitted central energy of $E_0=8.76$ MeV and a standard deviation of $\sigma=0.7$ MeV, as shown in figure 4.5.

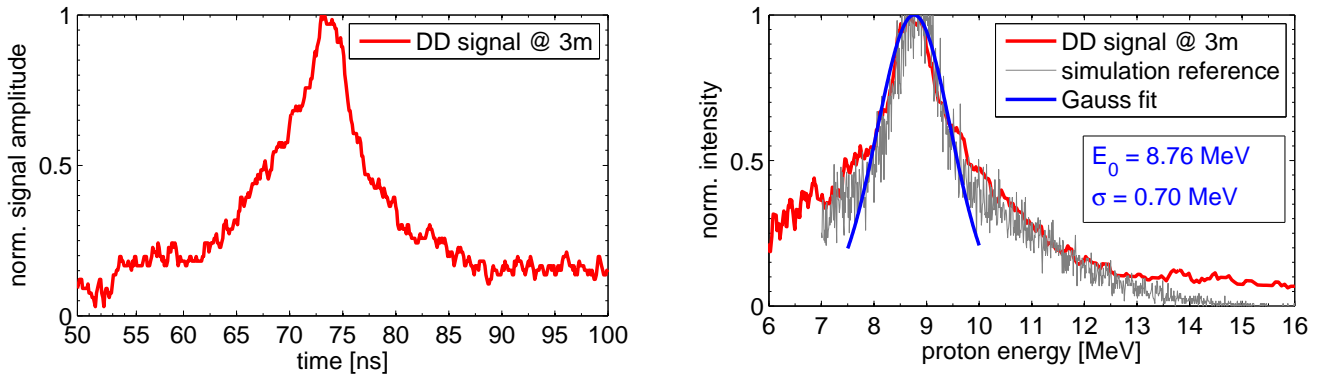


Figure 4.5: ToF results from the diamond detector (left picture) and obtained proton spectrum (right picture) for the case of focusing 8.8 MeV protons at 3 m, for which the FWHM is 8.6 ns (ToF) or 1.6 MeV (energy spectrum). The shown fit and fit parameters are according to equation 4.3. Also indicated (grey) is the reference input spectrum (for $E_0=8.8$ MeV) for the comparative tracking simulations with *TraceWin*.

4.3.2 Comparative simulations with *TraceWin*

The comparative simulation studies are again performed via *TraceWin*. Contrary to the simulation of the solenoid, no irregularities are to be expected in the case of the cavity and therefore the built-in *gap* function of the code is used for simplicity. To account for the realistic energy distribution of the initial proton bunch, again a customized input beam is created for the simulations, which is adapted to the actual measured beam parameters (compare section 4.3.1) by a superposition of a Gaussian with $\sigma=0.7$ MeV and another Gaussian with $\sigma=2.1$ MeV. The resulting spectrum fits the measured one very

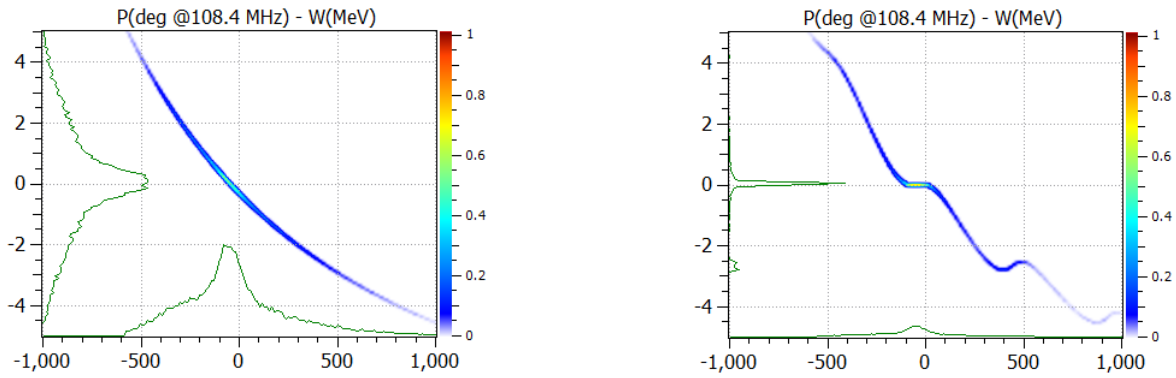


Figure 4.6: Principle of the energy compression via phase rotation. Left the bunch at 3 m without rf and right with rf (injection at -90 deg), shown in a ϕ_s -vs- ΔE diagram with $E_0 = 9.6\text{MeV}$. The energy is clearly compressed, but still residual particle numbers throughout all energies exist due to the longitudinally broad input beam.

well, as already indicated in figure 4.5.

Optimum energy compression is found to be at -90 deg synchronous phase and 850 kV total gap voltage (summarized over all three gaps), see figure 4.6. Caused by the large energy spread of the beam, not all protons are captured within one bunch and satellite bunches of higher or lower energy may occur as well as residual particle numbers of all energies. To obtain a 'clean' bunch, an additional dipole magnet could provide the necessary energy filtering after the phase rotation in future experiments.

Calculation of the proton energy distribution behind the cavity (at 3 m from source) for several different injection phases is done for a full phase scan for comparison reasons. Figure 4.7 shows the results for the phases probed in the following experimental campaign. One should be aware of the log scale in the figure. The ideal phase rotation in the simulation results in very sharp bunches, which cannot be expected that sharp in the experiment; thus the peaks will not be dominating the relative spectral intensities that much.

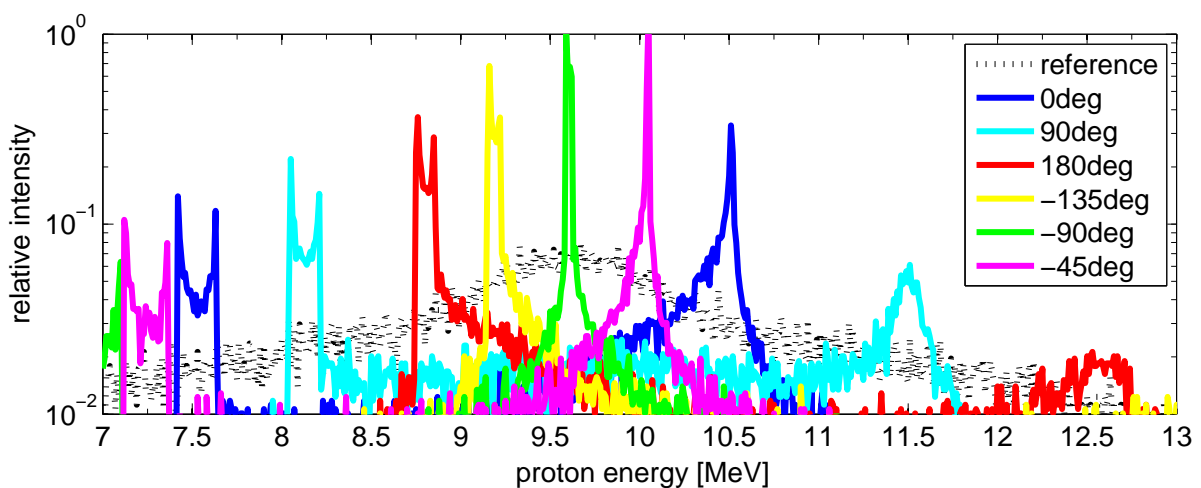


Figure 4.7: Simulated proton distribution for different injection phases ϕ_s (synchronous phase) for comparison to the experimental results. A characteristic energy shift is observed for each injection phase as well as occurring satellites.

Moving away from the optimum position at -90 deg, the energy spread of the final bunch increases and an additional energy shift is observed. This shift and the position of the satellites represent a way to measure the absolute synchronous phase, as will be shown in the next section.

4.4 Synchronization of laser and cavity

A crucial point for the combined experiments with the PHELIX laser and the rf cavity is the synchronization of both for reliable adjustment and exact knowledge of the injection phase of the proton bunch into the rf field (\rightarrow synchronous phase). Therefore, the full timing system is derived from the continuous UNILAC 108.4 MHz reference signal.

The rf wave within the cavity is freely adjustable and always in exact phase correlation to this reference and also PHELIX can be operated stabilized to the 108.4 MHz with a remaining jitter of 0.3 ns (i.e. ± 12 deg). Although a more precise adjustment in advance is currently not possible, an improved precision can be obtained with an on-shot measurement: The dielectric mirrors of the laser beamline have only a finite reflectivity. A photo diode - in this case placed behind the mirror in turning box four of the 100 TW beamline (close to the target chamber) - registers the leaking laser intensity of the passing pulse at an experimental shot and therefore provides the necessary precise relative measurement.

By recording the reference rf signal, the actual rf signal within the cavity and the photo diode signal of the passing laser pulse on-shot, a high precision relative phase measurement is possible with an accuracy of 0.05 ns (i.e. ± 2 deg). A calibration for absolute values still needs to be derived from experimental observations. Therefore, a compact dipole spectrometer has been designed and applied.

4.4.1 The compact dipole spectrometer

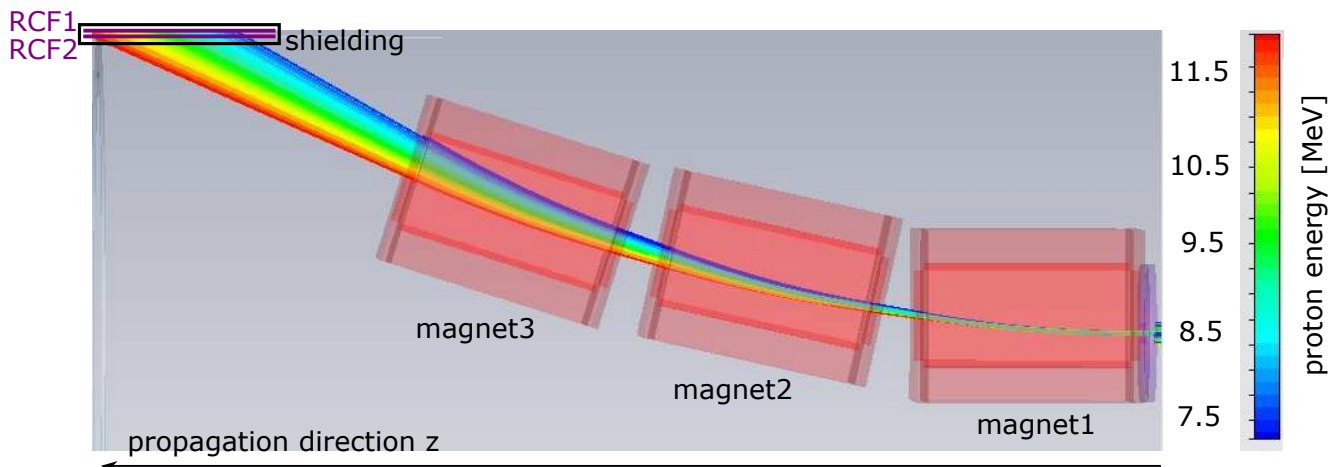


Figure 4.8: The protons enter the spectrometer through a pinhole (right), are dispersed in the perpendicular magnetic fields and finally detected with a RCF (type EBT3); also other detectors are possible, e.g. an IP.

A standard technique for determining the energy spectrum of a charged particle beam is by dispersion in a homogeneous magnetic dipole field. The separation is determined by the value of $\int B \cdot ds$, i.e. the product of the magnetic field B and the covered path length within the field s . To keep the spectrometer

compact enough to be placed within the beamline, high field strengths and permanent magnets are chosen. The final spectrometer consists of three identical permanent dipole magnets, an entrance pinhole and a detection area for a passive detector (IP or RCF).

Within each of the dipoles, two permanent $15 \times 30 \times 60 \text{ mm}^3$ *NdFeB* block magnets are aligned parallel to each other with a distance of 2 mm between the poles. They are fully enclosed with an iron yoke and iron apertures except for the entrance and exit slits. This results in a well defined field distribution with a very narrow fringe field region and the homogenous field area inside equals in good approximation an ideal (sharp rectangular) field area of 1.2 T over 60 mm (beam propagation axis *z*). Measurement and simulation (*CST EM studio*) of the field distribution have been done and the dispersion relation for the protons within the field obtained (see [Jahn, 2013]). Figure 4.8 shows a schematic view of the spectrometer.

With the magnets being permanent magnetic, the dispersing field is fixed and the energy resolution determined by the entrance pinhole size. The simulation shown in figure 4.8 uses a 1 mm diameter pinhole, while in the experimental campaign, a rather large entrance pinhole is used with a 6 mm diameter, resulting in an only rough energy resolution. The dispersion relation in the detector plane is depicted in figure 4.9.

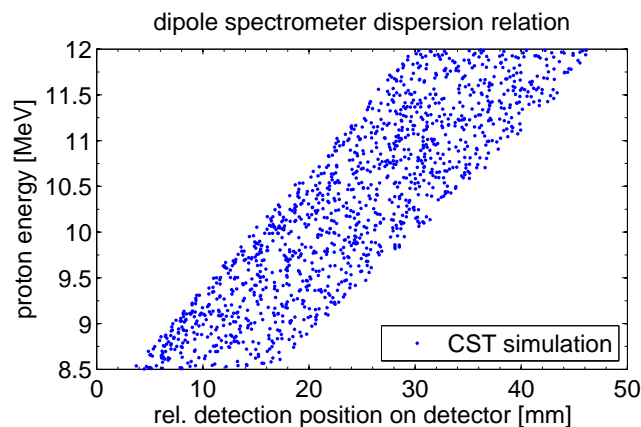


Figure 4.9: The dispersion relation of the magnetic dipole spectrometer. As a result of the large entrance pinhole (6 mm), the energy resolution is insufficient for precise measurements.

Two EBT3 films, which are covered by a $50 \mu\text{m}$ nickel layer and a $12.5 \mu\text{m}$ aluminium foil, served as detector. This first layer of aluminium and nickel is necessary to shield the RCFs from the radiation background caused by the running cavity. The Bragg energies of the two RCF layers are 8.8 MeV and 11.7 MeV. In the analysis, the integrated deposited energy over both layers is shown always. Due to the shielding and an angle of incidence of 63 deg on the detector (to detector surface normal) for the protons around the first Bragg energy (8.8 MeV), a lower energy cut-off exists at this energy, as lower energetic protons are not able to reach the active layer of the RCF, as they get stopped completely before.

Although no precise energy spread measurement is possible with this spectrometer in combination of the used pinhole, the relative energy spread of the proton bunch and the possible net acceleration or deceleration can be obtained directly after the experiment via the length and position of the proton trace

on the detector. This enables the necessary immediate feedback to calibrate and verify the synchronous phase, as a direct absolute measurement is not possible.

4.4.2 Calibration of the synchronous phase

The experiments on phase rotation with the applied rf start with a systematic scan of rf power and relative rf phase to define the working point for optimum energy compression and by this obtain the calibration of the measured relative phase to the absolute synchronous phase. These measurements are done with the compact magnetic dipole spectrometer. The relative length of the proton trace on its detector is a measure for the bunch's energy spread (all shown lengths are relative values with respect to the reference trace length without applied rf). This relative length has a minimum at optimum energy compression (-90 deg synchronous phase) and also depends on the totally applied gap voltage. This voltage U_{peak} cannot be measured directly, but is depending on the rf input power P_{rf} as $U_{peak} \propto \sqrt{P_{rf}}$ (see equation 4.2). This P_{rf} is calibrated to a normalized voltage $U_{n,exp}$, which is adjusted in the experiment. The measured relation is $P_{rf} = 2.74 \cdot U_{n,exp}^2$ for $[P_{rf}] = \text{kW}$ and $[U_{n,exp}] = \text{V}$. As the optimum rf input power is found to be at $U_{n,exp} = 6\text{V}$ (i.e. $P_{rf} \approx 100\text{kW}$), all given rf power values will be given relative to this value further on.

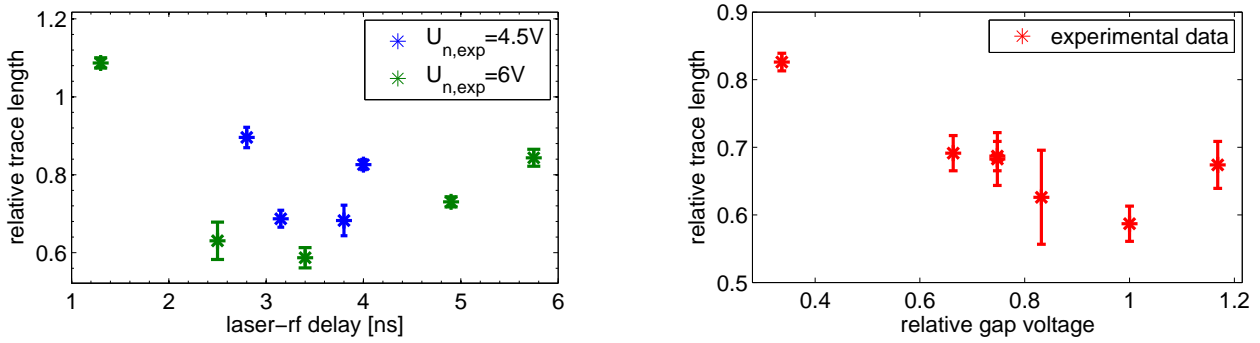


Figure 4.10: Left: Determination of the synchronous phase by varying the delay between the laser pulse and the rf and measuring the relative energy spread (relative trace length) at the dipole spectrometer. Shown are the results for two different rf input powers. The optimum energy compression (i.e. -90 deg synch. phase) is found to be at the minimum at 3.4 ns. Right: Scan of the applied gap voltage (\rightarrow rf input power) at -90 deg synchronous phase. Behind the optimum working position for energy compression (at $U_{n,exp} = 6\text{V}$) the energy spread increases again. This indicates that the bunch is *over-rotated* in longitudinal phase space, which enables the possibility of *phase focusing*.

From the analytical calculation, this input power indicates ideally a total gap voltage of 1.07 MV. As expected this value disagrees with the *TraceWin* simulations, which predict an optimum operation at an integrated gap voltage around 850 kV (compare section 4.2).

In the experimental campaign, the relative trace length measurement could be performed directly after each experiment shot, thus the calibration obtained within short time:

$$\Phi_s = 39 \frac{\text{deg}}{\text{ns}} \cdot \tau - 222.6 \text{deg} \quad (4.5)$$

with the synchronous phase Φ_s in units of degrees and the delay τ in nanoseconds. For the results shown in figure 4.10, the trace length is measured at 25% signal intensity. The situation when injecting a bunch with central energy $E_0=9.6$ MeV at $\Phi_s=-90$ deg is illustrated in figure 4.11. In the following, all results will be presented with regard to the measured synchronous phase. The correctness of the obtained relation will be verified further on by the correct prediction of the energy shift of the bunch and the occurrence of satellites at the predicted energies due to the injection phase. For interpretation of the results of the compact dipole spectrometer, one has to keep in mind the lower energy cut-off around 8.8 MeV and the only poor intrinsic energy resolution in the used setup. Therefore, the results of the tracking simulations are convoluted with the pinhole for comparison of the results. Still the occurrence of structures finer than the energy resolution is possible at the spectrometer, as the transverse beam profile of the bunch is not homogenous and local maxima may occur over the full pinhole aperture of 6 mm.

The experimental data of a complete scan over the synchronous phase is shown in figure 4.12, compared to the expectations from the simulations, which have been convoluted with the detector response (pinhole size) in the plot. The region of optimum energy compression is probed at a higher resolution of $\Delta\Phi_s=45$ deg with additional measurements at -125 deg and -32 deg, while the general step size of the measurements is $\Delta\Phi_s=90$ deg (within the adjustment accuracy of ± 12 deg).

At optimum energy compression (-90 deg) the central energy of the bunch remains unchanged. This is correctly observed with the dipole spectrometer by measuring a central energy of 9.6 MeV, which is the same as for the reference bunch without rf. Probing at an injection phase slightly off this optimum results in an additional shift of the central energy E_0 of the bunch. This is observed correctly for the case of -125 deg (shift to $E_0=9.3$ MeV) as well as for -32 deg (shift to $E_0=10.15$ MeV). All bunches show a comparable minimum energy spread with a tendency of slightly higher particle numbers than expected towards the higher energies.

The intensity maximum of the low energy satellite around 7.5 MeV, that moves towards higher energies with increasing injection phase, is not observed in the experimental data due to the lower energy cut-off at 8.8 MeV.

At 2 deg (maximum acceleration) the central energy is shifted to 10.5 MeV and now also a broadening of the spectrum is registered. At 89 deg injection phase the bunch experiences maximum energy de-compression. From the simulations, two satellites are predicted around 8.2 and 11.5 MeV. However, there is still a constant particle intensity for all energies in between. Considering the experimental data

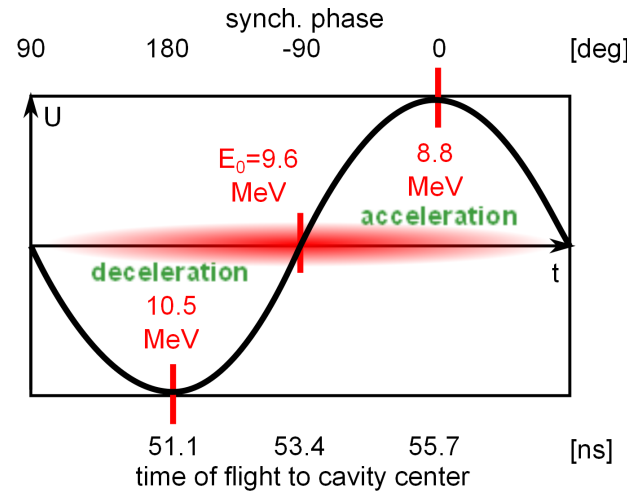


Figure 4.11: Illustration of the bunch position at the cavity center at $\Phi_s=-90$ deg (for $E_0=9.6$ MeV) and indicated according synch. phases for other energies within the bunch.

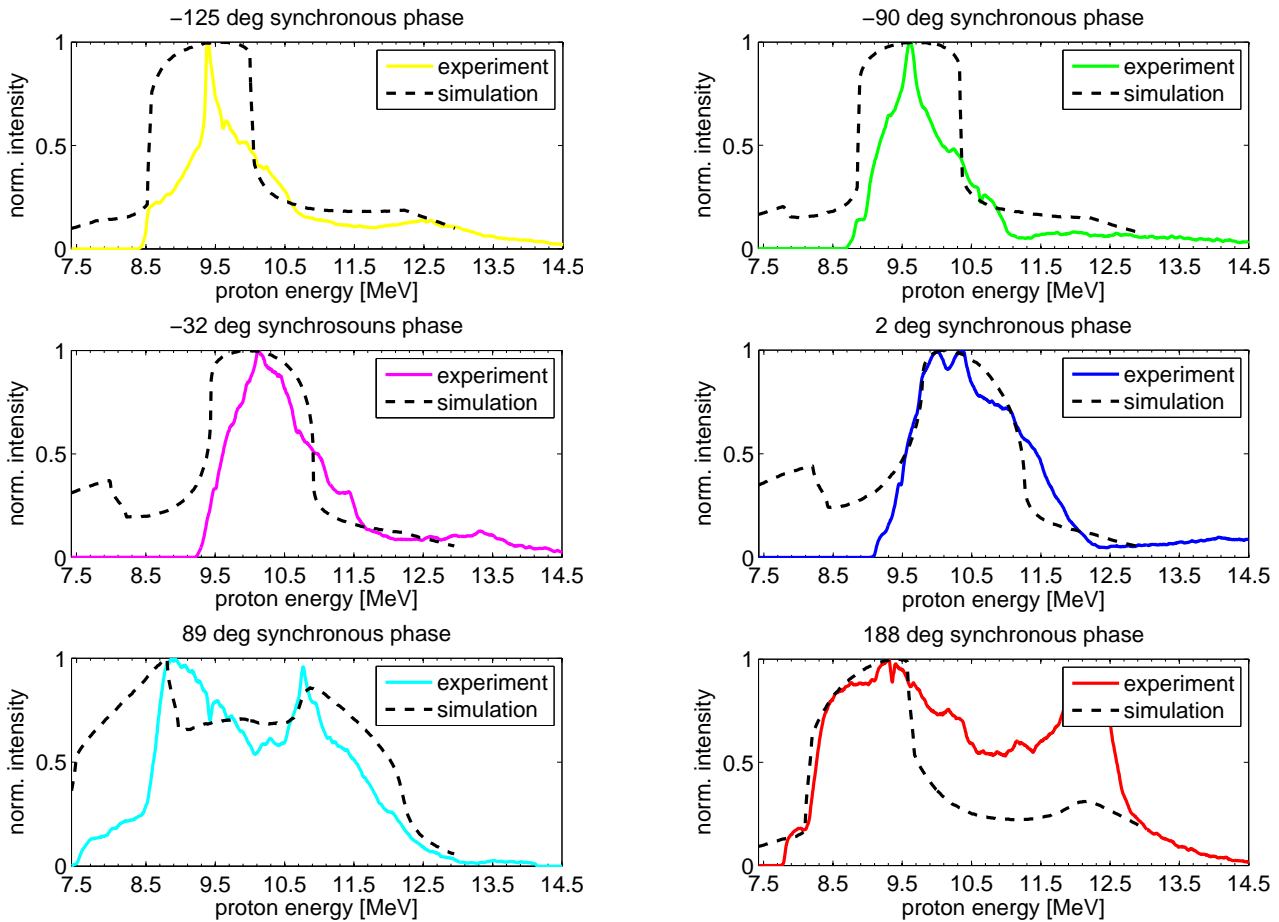


Figure 4.12: Measured traces at the magnetic dipole spectrometer for different injection phases. Also shown are the expectations from the simulations (see figure 4.7), convolved with the detector response. The observed energy spread in the experiment is clearly dominated by the detector’s intrinsic characteristics. The general shifts of the bunch’s central energy due to the injection phase, however, are in good agreement.

at the dipole spectrometer, the convolution of the signal with the pinhole results in a artificial shift of the high energy satellite, which is then observed correctly. The low energy satellite, however, is below the lower cut-off energy and thus explains the sharp drop of the signal towards lower energies. For 188 deg injection phase, this low energy satellite finally enters the detection region and matches very well the observed profile. Also the higher energetic satellite around 12.5 MeV appears consistently, only at a higher intensity than simulated.

The tendency towards higher particle numbers in the high energy region compared to the simulations is observed throughout (almost) all measurements and indicates a systematic under-estimation. A possible reason is the observed filamentation of the beam (especially in the higher energies, see section 3.5). The dipole spectrometer only covers a small part of the transverse beam profile and with a local filamentation maximum of the higher energetic particles by chance overlapping with the entrance pinhole, a systematic relative over-estimation of these energies would be the result.

The validity of the basic phase rotation characteristics and the correct determination of the absolute injection phase has now been obtained with the compact dipole spectrometer. For a detailed analysis of the

energy spread of the bunch, however, the energy resolution is insufficient. These measurements were done with another method and will be described in the following section.

4.5 Experimental results on energy compression

A measurement of the expected proton bunch is not possible with sufficient precision with the RCF method and the diamond detector, used for the characterization of the bunch along the transport section.

To provide sufficient sensitivity, EBT3-type RCFs need to be used. Due to their design, they show an energy resolution of 1.5 MeV around 10 MeV proton energy in a pure EBT3 stack configuration. This energy resolution is not acceptable as differences at a 0.5 MeV level (see figure 4.7) need to be resolved. Also, the diamond detector is practically not usable. The rf field manipulates the proton energies and consequently terminates the direct *time-vs-energy* dependency for the ToF measurement with the diamond detector. Although this could in principle be included in the calculation (knowing the position of the accelerating gaps), a precise measurement needs to be done at sufficient distance to the cavity. However, without additional transverse focusing elements the bunch will be very defocused at higher distances.

For a simple setup with a measurement near to the cavity exit, an additional diagnostic method is exploited: a modification of the RCF technique to reach the necessary energy resolution with EBT3 films and still obtain information about the transverse beam size and absolute particle numbers, called *the spectrally enhanced Radiochromic Imaging Spectroscopy (RIS)*.

4.5.1 The spectrally enhanced RIS

The RCF technique RIS is a very powerful technique for the characterization of the proton bunch, because it does not only probe a small sub-aperture of the beam, but is able to cover the full transverse beam profile, which is yet recorded with excellent spatial resolution, and obtains absolute particle numbers. However, the recorded energy deposition in the discrete active layers represents an intrinsic minimum energy resolution, which is worst for the EBT3 type films, as their active layer is enclosed by two rather thick plastic layers of 100 μm . Still, those films are the most sensitive and needed to be used in the experimental campaign. With the solenoid being the only transverse focusing element presently, the beam size behind the cavity is large ($15 \times 15 \text{ mm}^2$) due to the smooth focusing, thus the areal densities low and the sensitive EBT3s necessary. To still meet the required minimum energy resolution (0.5 MeV) with the EBT3 type RCFs, the analysis technique is modified for higher energy resolution at the expense of spatial resolution.

Each active layer in a stack of RCFs has a corresponding Bragg energy⁴ (see general description of RIS in section 2.3.2) according to thickness and density of the material in front of the active layer. If now a part of the transverse beam profile propagates through an additional layer of material (e.g. by covering half of the stack with an additional thin metal foil), the active layer of the RCF contains two different Bragg energies (one for each half space). In this way, as many different Bragg energies can be mapped in one active layer as different material thicknesses are applied in front of the layer. Scattering every thickness

⁴ Reminder: In this thesis, the term *Bragg energy* is used for the proton energy with the maximum energy loss within the active layer of the corresponding RCF, thus the proton that is stopped completely at the end of the layer.

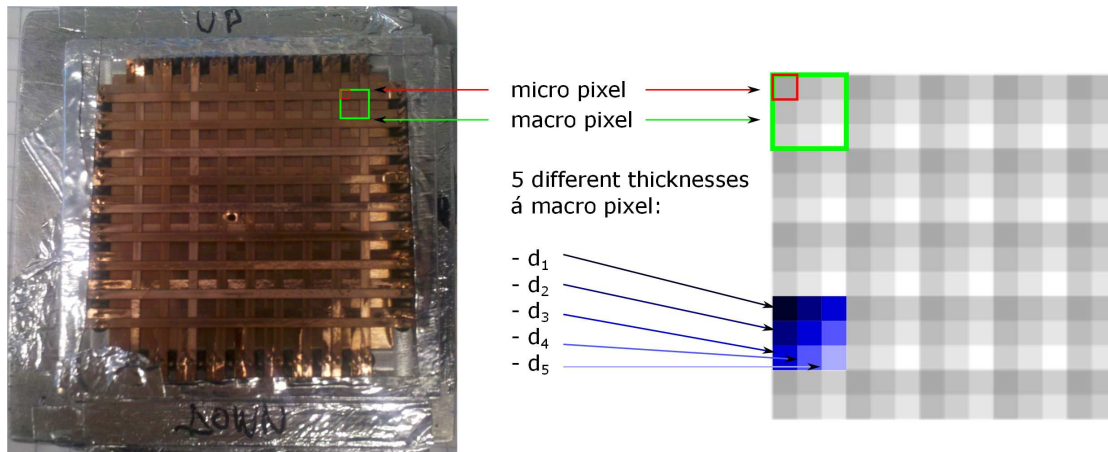


Figure 4.13: Left shown is a picture of the designed copper net, which is used as first absorption layer in the RCF stack. A hole through one of the central micro pixels (and also through the following RCFs behind) makes a parallel measurement with the RCFs and a comparative diagnostic (e.g. the compact dipole spectrometer) possible. The right picture shows the schematic of the copper net. The thicknesses of the net itself are between 0 and $80\ \mu\text{m}$ in five steps of $20\ \mu\text{m}$ ($d_{i+1} = d_i - 20\ \mu\text{m}$ with $d_1 = 80\ \mu\text{m}$). Behind the net are additional (full aperture) copper and aluminium absorbers to adjust the Bragg energies.

over the full transverse beam profile still keeps an acceptable spatial resolution for each Bragg energy. For the experimental campaign with the cavity, a special copper spacer with a regular pattern of different thicknesses has been designed and fabricated. The resulting energy resolution is given by the different applied thicknesses of the micro pixels and the spatial resolution by the size of the regularly placed macro pixels (sketch see figure 4.13).

Each micro pixel has a size of $1.27 \times 1.27\ \text{mm}^2$ (1/20 inch) and each macro pixel is consequently $3.81 \times 3.81\ \text{mm}^2$ in size. The chosen pattern results in micro pixels of five different thicknesses d_{1-5} and the arrangement is the same in each macro pixel. These thicknesses are linearly scaled between zero and $80\ \mu\text{m}$ with a step size $\Delta d = 20\ \mu\text{m}$. The resulting copper net with regular varying thickness in general allows for mapping five different Bragg energies in one active layer, in this case over a full usable detection area of $20 \times 20\ \text{mm}^2$.

In the experiment at hand, the targeted proton energy is 10 MeV and one specific configuration for the RCF stack with the copper net improves the obtainable results further: the copper net is followed by additional $100\ \mu\text{m}$ copper, $25\ \mu\text{m}$ aluminium and finally three EBT3 films. In this arrangement, the middle RCF maps the five Bragg energies 9.0, 9.5, 10.0, 10.5 and 10.9 MeV, which at the same time appear as Bragg energies in the first (9.0 and 9.5 MeV) and third (10.5 and 10.9 MeV) film, too, within an accuracy of $<0.1\ \text{MeV}$. In the later analysis, the micro pixels of corresponding Bragg energies from different films are merged in virtual layers to in total 11 different of those virtual layers, which are created from the three films (see figure 4.14). While all central layers cover (in combination) 3/9th of the transverse beam profile, the highest and lowest energies cover only 1/9th and the second highest and second lowest 2/9th. For a correct analysis, this difference in coverage ratio needs to be compensated, which is done by scaling the totally deposited energy in each layer, i.e. practically dividing the measured deposited energy of the second highest and lowest energies by 2 and of the central energies by 3. This needs to be

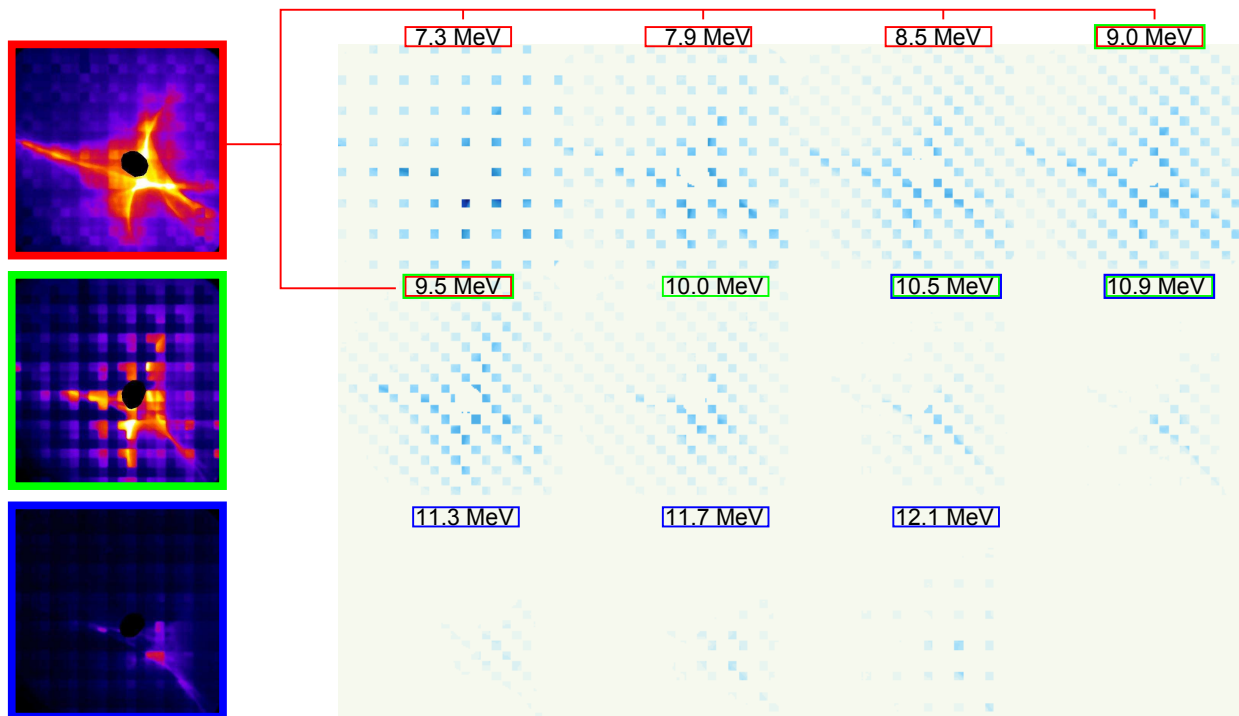


Figure 4.14: Example of the obtained results with the *spectrally enhanced RIS*. On the left shown is the color-coded deposited energy profile in the 3 films. 11 virtual layers are deduced from these (depicted with corresponding Bragg energies on the right). A still good spatial resolution is obtained. For correct deconvolution in the next step of the analysis, the deposited energy in all films is scaled according to the spatial coverage.

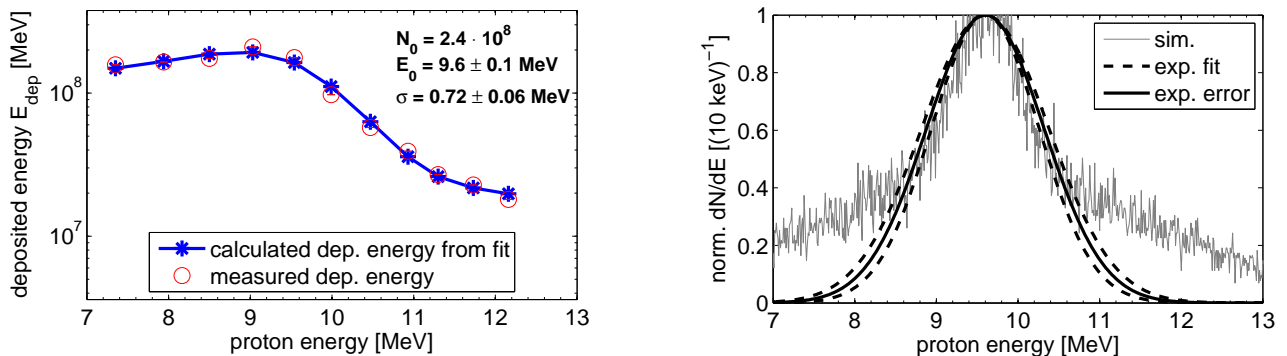


Figure 4.15: Deposited energy in the RCFs when focusing 9.6 MeV at 3 m to the laser target. A Gaussian spectral distribution with an energy width of $\sigma=0.72$ MeV (compare equation 4.3) can be deduced by deconvolution. The calculated deposited energy from such a Gaussian-like distribution fits the measured deposited energy very well.

taken into account when finally calculating absolute particle numbers.

Comparative measurements with a focal energy of 9.6 MeV are performed with the RCF technique. Assuming the spectral shape of (the earlier introduced) Gaussian-like distribution (see equation 4.3) and deconvolution of the deposited energy profile obtains the fit parameters $E_0=9.6$ MeV and $\sigma=(0.72\pm0.06)$ MeV. Then calculating backwards, the expected deposited energy of the fitted Gaussian within the RCF stack shows a very good agreement, see figure 4.15. In another shot with the same setup, a fitted standard deviation of $\sigma=(0.68\pm0.06)$ MeV has been obtained. Both fit very well to the comparative measurements with the diamond detector. By means of energy spread at FWHM this is $\Delta E/E_0=(18\pm3.0)\%$.

4.5.2 Energy compression of the proton bunch

The first steps of data processing reveal the deposited energy at the different Bragg energies. Before calculating the energy spread, these results (shown in figure 4.16) can be used already for cross-checking the basic characteristics of the phase rotation.

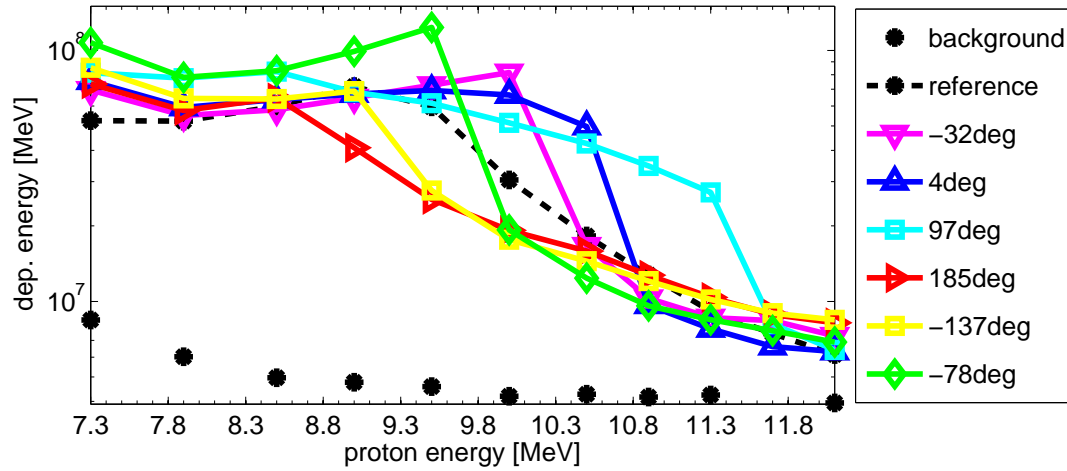


Figure 4.16: Deposited energy in the RCFs, depending on injection phase. Also shown a reference shot with rf off and a measurement of the background signal (caused by the rf radiation) with no protons on the detector but only the rf running.

Starting at the optimum energy compression (-78 deg), a peak in deposited energy is observed around 9.5 MeV with a drop of nearly an order of magnitude behind the maximum; this drop of course cannot be seen in front of the peak, as the particles contributing to the peak deposite energy in the front layers, too. A peak-like and accordingly shifted feature is also observed for the neighboring measurements at -32 deg and -137 deg. Furthermore, the intensity drop behind 10.5 MeV for 4 deg and the broad energy distribution with intensity drop behind 11.5 MeV for 97 deg are confirmed by the simulations and in good agreement with the complementary dipole spectrometer data, as well as the predicted intensity peak around 8.5 MeV (188 deg synchronous phase).

A detailed analysis is now performed in the area of optimum energy compression by the deconvolution technique, assuming a Gaussian-like spectrum (equation 4.3). Contrary to fitting the reference spectra, now the central energy E_0 is not treated as a free fit parameter anymore, but obtained from the simula-

tions at the precise synchronous phase of each shot. This results in a net shift of the central bunch energy of $\Delta E = 0.1$ MeV to $E_0 = 9.7$ MeV for the case of -78 deg. Performing the deconvolution with this value for E_0 results in the fit parameter $\sigma = 0.11$ MeV. The error of this calculation is dominated by the uncertainty of the correct Bragg energies for each RCF layers. Using a maximum error of 0.1 MeV, this consequently results in a measurement uncertainty that can be included by an error for E_0 of 0.1 MeV. Applying the deconvolution also to the values of $E_0 \pm 0.1$ MeV then gives an error estimate for the standard deviation σ , thus the energy spread. This uncertainty is a consequence of the still limiting energy resolution. The deconvolution with $E_0 \pm 0.2$ MeV, however, clearly fails to reproduce the deposited energy profile. The energy resolution for the spectrally enhanced RCF technique in this special case therefore can be estimated to ± 0.1 MeV with respect to E_0 , which in return can be used for an error estimation of the measured standard deviation to $\sigma = (0.11 \pm 0.07)$ MeV for the applied RCF technique. Figure 4.17 shows the deconvolution fit and resulting spectrum. Also shown is the comparison with the simulated spectra, which are even narrower than the lower error limit that can be obtained with the detection method.

A similar analysis is possible with other shots with an injection phase near the optimum injection. In these cases the spectrum can still be fitted by a Gaussian profile in good approximation. Shown in figure 4.17 are the results for -32 and -137 deg. The resulting energy spread is $(3.1 \pm 1.7)\%$ for the case of -32 deg and $(5.3 \pm 2.7)\%$ for the case of -137 deg. In both cases, the measured energy spread is larger than for the optimum injection phase $((2.7 \pm 1.7)\%)$ and again considerably larger than in the simulation.

As the RCF films are absolutely calibrated to protons, a calculation of particle numbers is possible via numerical integration of the Gaussian-like distribution function (equation 4.3). Instead of integrating the proton number per given energy interval (e.g. MeV^{-1}), the integration is done here within the FWHM of the distribution function. This calculation is performed for all three shots shown in figure 4.17. The error is derived from the uncertainty of the correct Bragg energies of the RCF layers and might actually be a little higher if involving the uncertainty in the dose calibration of the film, which is around 5%.

Finally the obtained values have to be multiplied by 3 to (roughly) take into account, that each (virtual) layer only covers one third of the transverse beam profile, and once more be multiplied by 3 to reverse the down-scaling of the deposited energy of the (central) layers compared to the edge layers, which cover only one ninth. The resulting proton numbers within the FWHM of the Gaussian-like distribution function are $1.7 \cdot 10^9$ ($\pm 15\%$) for the shot at -78 deg, $1.2 \cdot 10^9$ ($\pm 17\%$) for the shot at -32 deg and $8.7 \cdot 10^8$ ($\pm 5\%$) for the shot at -137 deg.

For the other injection phases a Gaussian-like proton spectrum cannot be assumed anymore. Still an analysis is possible to some extent, e.g. for the case of maximum acceleration (4 deg synchronous phase): The simulations predict an asymmetric distribution with a peak at 10.5 MeV, a steep fall towards higher energies and a flatter one towards lower energies. An approach to analyze this shot is to separate at the peak energy and fit both parts individually. For the high energy part (10.5 MeV layer until last) this has no consequences (except for the poorer statistics) as the lower energetic protons do not interfere with the signal, because they are stopped in the front layers completely.

The low energy part (first layer until 10.5 MeV layer, again including this last one), however, is missing the information of the energy deposition of the higher energies and still assumes the symmetric Gaussian to be valid. Thus, this will result in a systematic error and under-estimate the particle numbers at

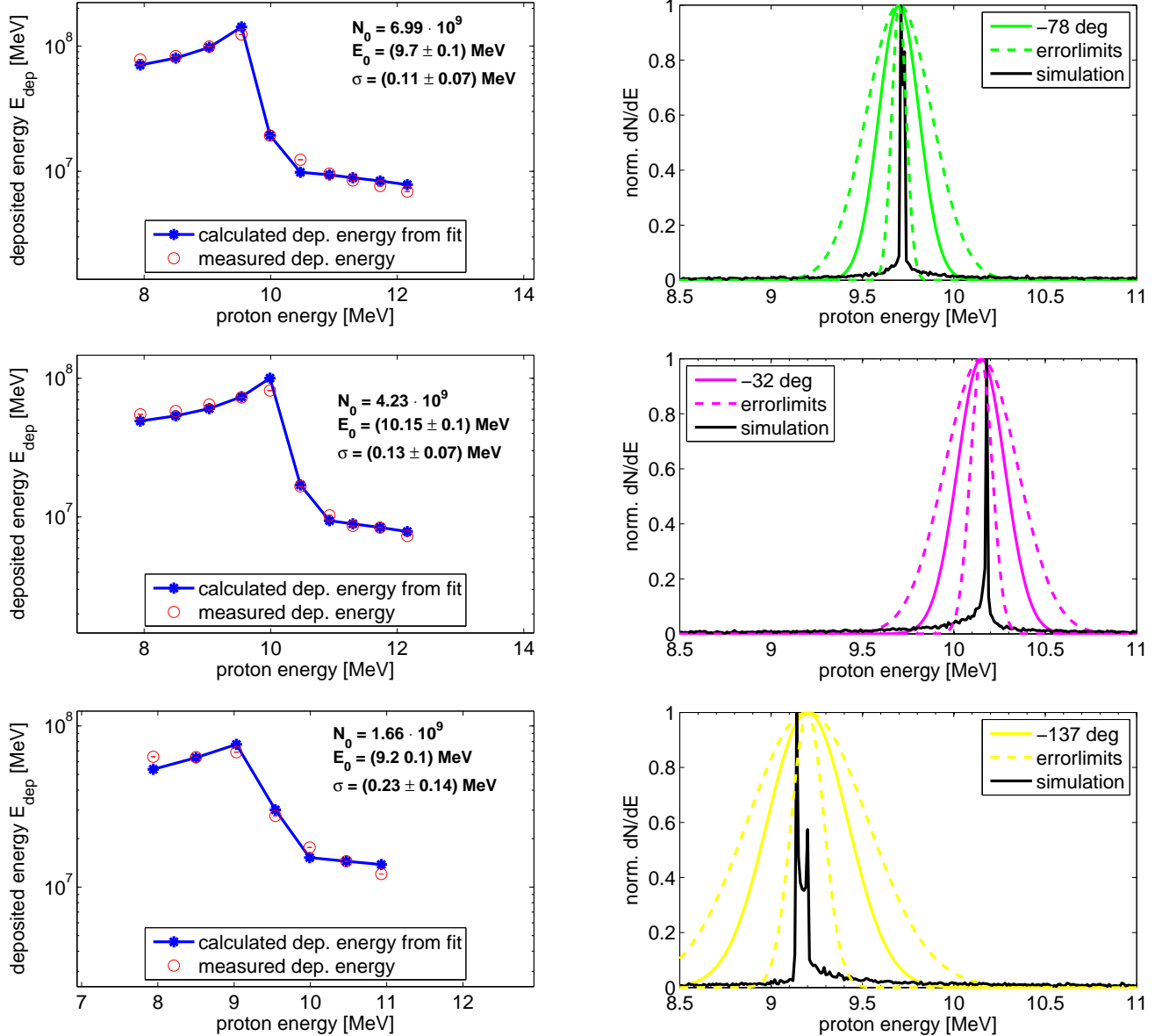


Figure 4.17: Deposited energy in the RCFs at optimum energy compression of the bunch (upper left graph). The data analysis (deconvolution of the deposited energy into a proton spectrum) results in a narrow Gaussian spectrum around a central energy E_0 of 9.7 MeV with a standard deviation $\sigma=(0.11\pm 0.07)$ MeV; this corresponds to an energy spread $\Delta E/E_0$ at FWHM of $(2.7\pm 1.7)\%$. This spectrum is then illustrated (upper right graph) including the results from the (ideal) simulation. Also shown are the deconvolution fits for injection phases -32 and -137 deg and resulting spectra including the reference results from simulations.

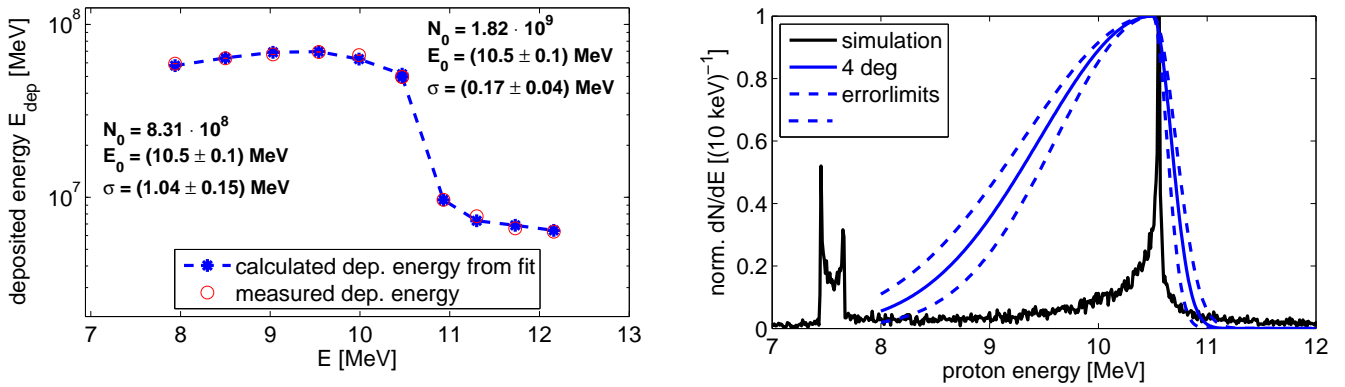


Figure 4.18: Deposited energy in the RCFs at $\Phi_s=4$ deg (left graph). The analysis is split into two separate regions (low and high energies) with the central deposited energy (10 MeV) as common overlap. This asymmetry assumption is based on the simulation predictions and fits the simulations well if the sharp peak of the ideal simulation is neglected (right graph).

10.5 MeV while over-estimating the standard deviation. As illustrated in figure 4.18, the individual fits may match well, but only the high energy part is fitted correctly.

Plotting the resulting section-wise defined function against the expected simulated distribution (also shown in figure 4.18) indicates the correct principal behavior. As expected, the higher energy slope gives a good measurement, while the low energy slope (suffering from the systematic error) is expected to show a much narrower standard deviation.

The forseen operation mode of the beamline, however, is at -90 deg injection phase to minimize the bunch's energy spread or perform a phase focusing experiment. The use of the cavity to accelerate the bunch is inefficient and unnecessary. Higher energetic particles are available from the source and could be chosen right from the beginning by adjusting the solenoid field.

Results on these first experiments are published in [Busold et al., 2014b].



5 Perspectives for the LIGHT beamline

The experimental chapters up to now have been straight forward in combining the different stages to a reliable working novel beamline concept: Characterization of the source, the transport section and the phase rotation stage. However, there are multifold optimization possibilities at each stage; several of them being investigated already within the LIGHT collaboration and some even within the scope of this thesis. In this final chapter a selection of promising improvements will be introduced and first experimental results presented, starting again at the source and finishing with the possible next stages towards a fully functional laser-driven proton beamline for secondary experiments with highest-intensity single bunches.

5.1 Optimization of the source

The optimization of the laser-based sources is a wide and intensely studied field of research. At this point, other acceleration mechanisms like **RPA** (*radiation pressure acceleration*, see e.g. [Esirkepov et al., 2004, Palmer et al., 2011, Aurand et al., 2013]) or **BOA** (*breakout afterburner*, see [Yin et al., 2006, Yin et al., 2011]) are presented typically in the run for higher particle energies. In this special case, however, considerable higher energies are not of main interest and would even be incompatible with the existing cavity, thus cause major changes within the setup. The focus of this beamline is reaching highest bunch intensities at the present energy level around 10 MeV. Therefore, possible improvements should aim at a higher efficiency of the TNSA mechanism.⁵

The source is defined basically by the laser and the target parameters. Both can be tuned and promising possibilities are presented in short in the following.

5.1.1 Target parameters

The driving mechanism of the laser-based ion acceleration is the coupling of the laser to the electrons of the target, i.e. the efficient heating of electrons. Improving this coupling directly improves the ion acceleration. In TNSA experiments, a great part of the laser light is reflected at the critical surface ($\approx 50\%$) in the pre-plasma and therefore lost to the electron heating. Enhanced laser absorption by controlling the pre-plasma parameters was shown in two different ways: On the one hand, using an additional laser [Carroll et al., 2009, Yogo et al., 2007] to control the pre-plasma parameters. The electron heating mechanisms are highly depending on the density gradient (scale length) of the pre-plasma. This can be 'engineered' by a preceding laser pulse, which is matched in intensity and arrival time. Such a preceding laser pulse may be at fs or at ns level. Both options are possible at Z6 with either the PHELIX double-pulse option of the fs frontend or employing the nhelix ns laser.

Another way of increasing the laser-to-electron coupling efficiency is preparing the target front surface and either re-use the reflected energy [Scott et al., 2012] or enhance the absorption by structured surfaces [Margarone et al., 2012, Marjoribanks et al., 2008]. With the latter, an absorption efficiency increase of up to 90% has been demonstrated experimentally. Such target preparation techniques are also

⁵ For completeness, there should also be mentioned the **collisionless shock acceleration** [Haberberger et al., 2012] and the acceleration via **Coulomb explosion**. The latter most recently drew increased attention by the demonstration of accelerating MeV proton bunches in a peaked spectrum via irradiating a (composite material filled) carbon nanotube with an intense laser pulse [Murakami and Tanaka, 2013].

applicable at the LIGHT beamline, especially in close collaboration with the target fab at TU Darmstadt, which is able to manufacture such targets.

Furthermore, the continuous and exponentially decaying spectrum of the typical TNSA ion beams are unfavorable for many applications. Therefore the shaping of the spectrum from source has been the focus of several investigations and the vague term *quasimonoenergetic* is often used already for local modifications of this spectral shape. Although even the best experimental results are still far from a monoenergetic ion beam, major modifications to peaked spectra could be demonstrated for protons and carbon ions [Hegelich et al., 2006, Schwoerer et al., 2006] by special ways of target treatment.

Finally, the target geometry can be changed, too. Hemispherical targets have been used to modify the beam divergence from source [Bartal et al., 2012] and also more complex geometries have been investigated. Furthermore, the target size can be changed. Limiting the transverse target dimensions leads to a better confinement of the hot electrons in TNSA experiments and consequently to an improved acceleration [Kluge et al., 2010]. This is in principle also true for minimizing the target thickness. However, this is limited by the laser parameters, as a very thin target can already be destroyed by pre-pulses or the ASE preceding the main pulse. Especially for being able to use sub- μm thin targets to achieve relativistic transparency of the target within the pulse duration (\rightarrow BOA) or even thinner targets to accelerate a whole volumetric increment of the target (\rightarrow RPA), work on the laser parameters is vital.

5.1.2 Laser parameters

Much effort was taken to improve the laser parameters during the last years. The two laser parameters, that are presently in the focus of research, are the intensity and the contrast of a laser system. Although at PHELIX great progress could be made by removing pre-pulses, reducing the contrast level to 10^{-10} [Wagner et al., 2013], upgrading the target area at the laserbay with now up to 250 J of laser energy available in the short pulse mode and a steep focusing parabola for smallest spot sizes, the 100 TW beamline at the Z6 area is essentially limited in energy by its sub-aperture beam size. Thus, the LIGHT beamline will be restricted to a TNSA source for the near future, which is, however, fine as the handling of considerably higher particle energies is not possible with the present system.

Apart from contrast and intensity another laser parameter might be of interest instead: The laser transverse focal shape on the target. Calculations predict a lower divergent beam from the source if applying a hollow laser beam profile [Brabetz et al., 2012]. Also, it has been demonstrated that an elliptical focal laser spot results in an elliptical proton beam [Roth et al., 2005] with reduced divergence in one plain and increased in the other. This might lead to an increased capture efficiency of the protons when using quadrupoles instead of a solenoid. Using quadrupoles holds several advantages in general, which will be explained in the following section.

5.2 Alternatives for beam transport and energy selection

The pulsed solenoid is currently the central element for energy selection and beam transport within the beamline. Reduction of its field aberrations for better optical properties is an important aspect for possible optimizations. However, the whole concept of solenoidal focusing may be reviewed compared to the use of (the more standard) quadrupole focusing. Reasons for this consideration are:

- Quadrupole focusing is stronger than solenoid focusing [Hofmann, 2013]. Especially for higher ion energies the solenoid becomes inefficient.
- Quadrupoles with strengths necessary for the currently available energies can be built as permanent magnetic devices, thus reducing size and complexity of the setup.
- The high capture efficiency of the solenoid can nearly be matched with special designed quadrupole setups, too.
- The observed space charge effects at the solenoid focusing will not occur using quadrupoles.

Based on these arguments, first experiments with permanent magnetic quadrupoles (PMQs) have been performed at PHELIX in the scope of this work. The experimental setup and results are presented in this section. However, there are also some drawbacks concerning the PMQs:

- Changing the focal energy and/or position requires a re-arrangement of the magnet setup and thus possibly even re-alignment. Consequently, a setup based on PMQs is less flexible.
- The inevitable defocusing of the divergent beam in one transverse direction at the first quadrupole results in significant particle losses. However, this might be compensated by an 'engineered' proton beam from source.

Finally, it should also be mentioned here that extensive research is done on the investigation of alternative ion optics other than the conventional ones (solenoids and quadrupoles) presented in this thesis, e.g. driving miniature single-loop coils with ns laser pulses [Fujioka et al., 2013] or plasma lenses with additional fs laser pulses [Toncian et al., 2006]. All these are single-use devices, that need to be replaced after each shot, and need a second laser pulse. Still, significant progress has been claimed lately with capture efficiencies of 30% and achromatic focusing possibilities for a plasma lens setup (similar to [Toncian et al., 2006])⁶.

5.2.1 The permanent magnetic quadrupole doublet and experimental setup

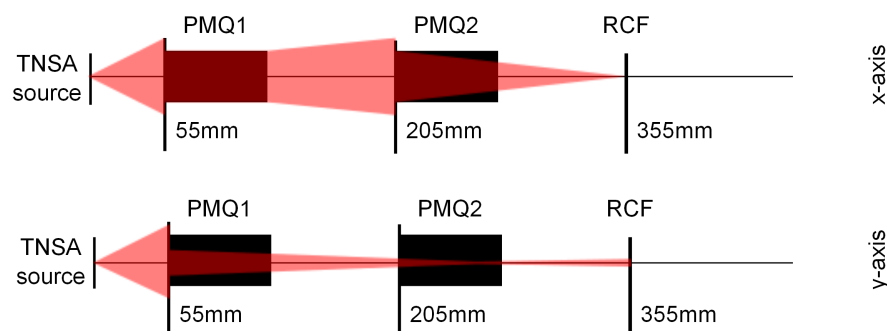


Figure 5.1: Schematics of the quadrupole setup. Each quadrupole is focusing the beam in one (transverse) beam direction and defocusing in the other.

As an alternative to the pulsed solenoid, quadrupole focusing was investigated within this thesis, too, using a PMQ doublet. It consists of two identical PMQs, which are both well characterized: they have

⁶ J. Fuchs *et al.*, unpublished results and private communication

a length of 80 mm, a field gradient of 85 T/m and a clear aperture of 24 mm diameter each. The still compact design is possible due to the Hallbach design of the devices. Special support structures provide for a flexible and precise alignment inside the target chamber.

While the pulsed solenoid needs to be placed at a sufficient distance to the target to avoid induced Eddy currents at the target position due to the rising magnetic field, the quadrupoles can be placed at a nearer position, which increases the overall capture efficiency and at least partly compensates for their largest disadvantage: The defocusing of the beam in one transverse direction at the first magnet results in significant additional particle losses compared to the solenoid.

In an experimental campaign with PHELIX at Z6, transport and focusing with this doublet has been investigated. The first PMQ is set at 55 mm distance to the target and the second at 205 mm. This configuration results in focusing 5 MeV protons at 355 mm and an improved capture efficiency (in contrast to earlier experiments with quadrupoles [Schollmeier et al., 2008]). Beam detection is again done by RCFs and comparative simulation studies performed with the *TraceWin* code. The energy depended full transverse beam characterization (x-y, x-xp and y-yp plots) is shown in figure 5.2.

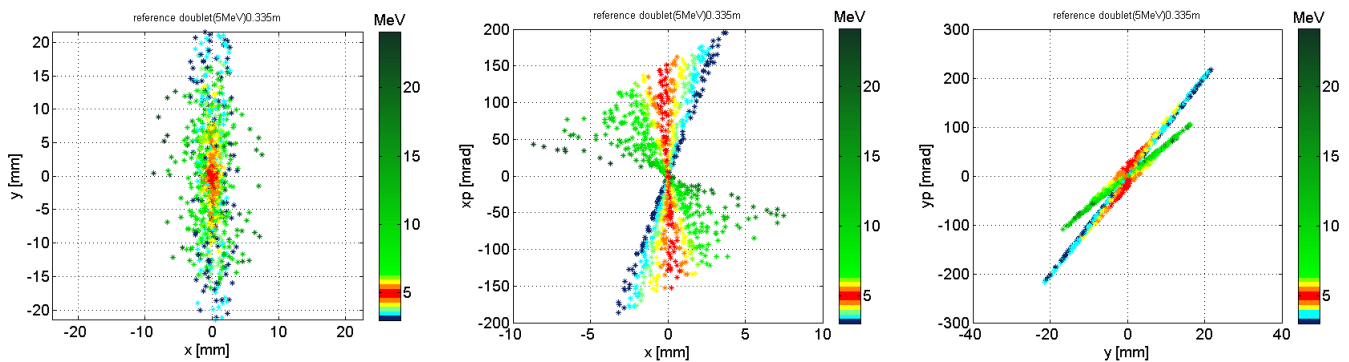


Figure 5.2: The simulated transverse beam properties at 355 mm from the source. The left picture shows the transverse beam profile and the middle and right pictures the distribution in phase space for both transverse beam axes.

5.2.2 First results on efficient quadrupole focusing with a doublet

At a distance of 355 mm to the TNSA source a focus of 5 MeV protons is observed, containing 1.7×10^9 ($\pm 6\%$) particles in an energy interval of $\Delta E = \pm 0.5$ MeV around the focal energy. The focus shows an elliptical shape and is $1 \times 2 \text{ mm}^2$ at FWHM in size. The (color-coded) layers of the irradiated RCF stack are shown in figure 5.3 and compared to the simulated shape of the corresponding Bragg energy of each layer.

While one has to keep in mind that in the experiment also the higher energies contribute to the detected deposited energy of each layer, the simulations in this case are done with a mono-energetic beam and for each Bragg energy separate. Considering this, the results of experiment and simulation are in excellent agreement. The observed rippled structures at the edges of the beam throughout all layers originate from inaccuracies of the focusing fields towards outer radii and are directly connected to the interfaces between the different segments of the Hallbach magnet.

Most importantly, the quadrupoles show excellent optical qualities, which are related on the one hand to less aberrations in the focusing field and on the other hand to the separated focusing in both trans-

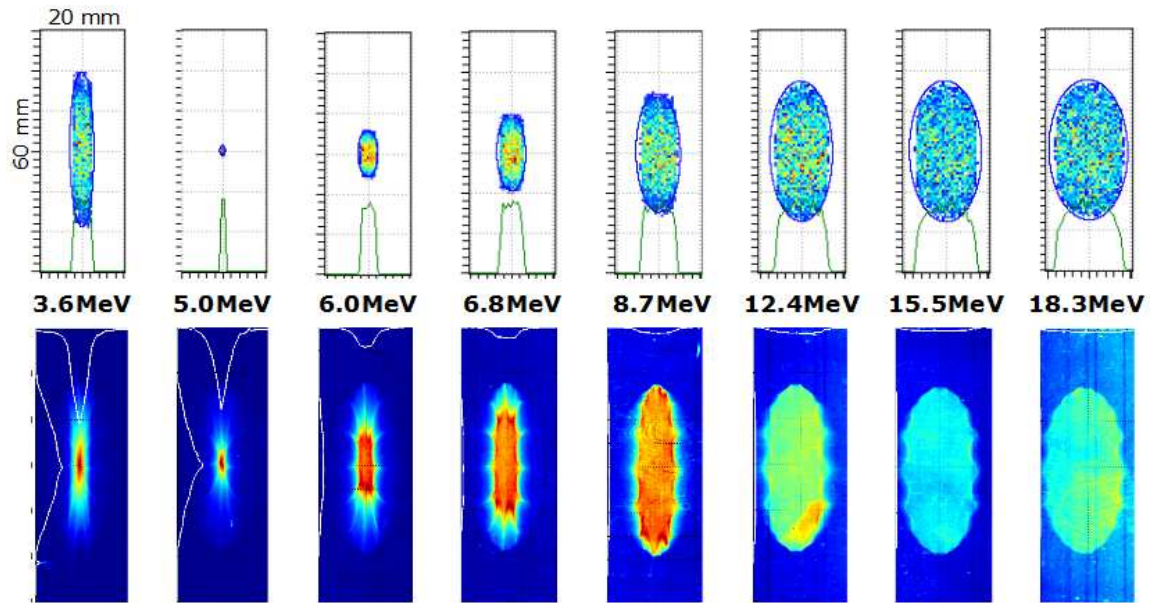


Figure 5.3: Comparison of simulational and experimental results on focusing a TNSA proton beam with a magnetic doublet. The upper row shows the simulated transverse beam profile at 355 mm distance behind the source for different energies. The lower row shows the experimental results: the single layers of the used RCF stack (their response to the proton beam is color coded) with the corresponding Bragg energies. All shown films have the same dimension as in the simulation ($20 \times 60 \text{ mm}^2$) and are in very good agreement.

verse directions and the resulting reduced space charge effects in contrast to the solenoid: Co-moving electrons, that are able to penetrate the magnetic field, are defocused in the plain perpendicular to the proton defocusing due to their negative charge. Thus a high on-axis concentration like in the solenoid case is avoided and the space charge effect minimized.

In another experimental campaign, the focusing characteristics of a single of these PMQs has been investigated in detail with respect to the electron influence. The electrons have been stripped of the beam with a thin metallic foil at a position of a few centimeters to the source. The PMQ produced a straight line focus of the protons and the effect on the properties on this focus has been measured when stripping the electrons (the straggling of the protons inside the stripper foil has to be taken into account). Doing this, no significant further changes in the focusing characteristics have been observed, thus no effect of the presence or absence of the co-moving electrons in the quadrupole case⁷.

5.3 Towards highest intensities

Apart from tuning the laser-based source and the transport section, the capabilities with the rf cavity can be exploited further, too. Although the injected proton bunch shows a large energy spread of $(18 \pm 3)\%$, the corresponding ellipse in phase space is very narrow (\rightarrow low longitudinal emittance) and a quite strict linear relation between phase and energy is observed due to the particles being emitted from source in only a very short time ($\approx 1 \text{ ps}$). This allows for efficient phase focusing with the cavity.

⁷ A detailed description of a dedicated experimental campaign can be found in H. Al Omari, PhD thesis, Frankfurt University (2014)

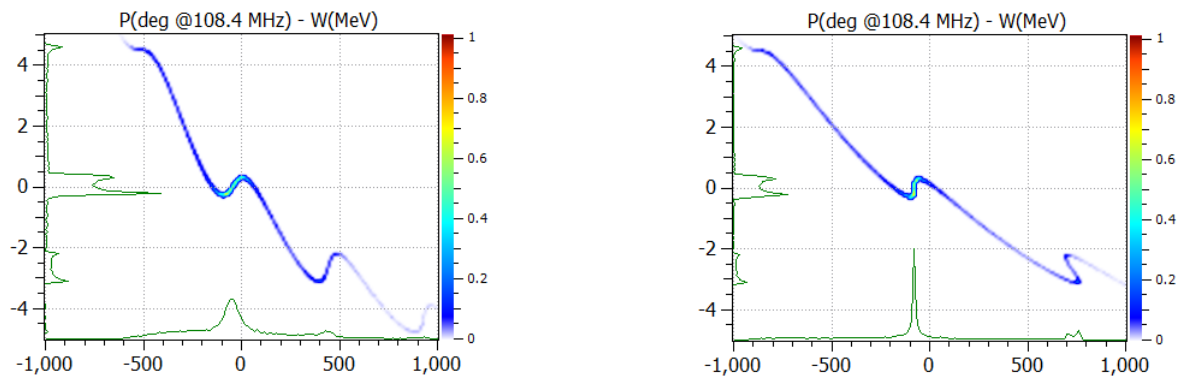


Figure 5.4: Simulation of phase focussing with the rf cavity. Applying higher rf voltages than in the case of optimum energy compression results in 'over-focussing' right behind the cavity (at 3 m to source, left picture). Propagating the bunch further leads to a longitudinal focusing and a minimum bunch duration of 0.1 ns (FWHM) is observed at 5 m from source (right picture).

Increasing the applied rf power at the cavity, the bunch is further rotated in phase space, leading to an again increasing energy spread after the point of optimum energy compression. This 'over-focused' bunch has now slower particles at the front and faster ones at the rear. Further propagation of this bunch compresses the bunch in time automatically, as the particles from the rear catch up with those in front. This mechanism is called *phase focusing* and is illustrated in figure 5.4.

The first experiments with the cavity of the LIGHT beamline revealed that this is possible with the existing setup already as could be observed by the again increasing energy spread of the bunch in the rf powers scan at an injection phase of $\Phi_s = -90$ deg (see figure 4.10 in the previous chapter). Preliminary simulations predict a pulse duration in the sub-ns regime down to 0.1 ns to be possible. With the available high particle numbers and additional transverse focusing, this allows for highest intensities for a single short bunch.

5.4 A unique experimental area at GSI

After addressing several optimization possibilities and the capabilities of the present LIGHT beamline at Z6, in this final section the concept of a fully functional laser-driven proton beamline and its use for secondary experiments with the unique beam is presented.

The accessible high intensity beams are of great interest in investigations on high intensity effects in plasma physics, material science, biology and for the use as a diagnostic tool. These peak intensities at the MeV energy level cannot be provided by present conventional accelerators. E.g. taken the parameters of the planned high intensity proton linac for the FAIR facility⁸, one can calculate from the minimum pulse length ($36 \mu\text{s}$), the rf frequency (325 MHz) and the proton number per pulse (7×10^{12}) a maximum intensity of 5×10^8 protons/ns in the optimum case, while (via phase focusing) even now intensities of $> 10^{10}$ protons/ns are accessible with the LIGHT beamline. Therefore, additionally to the general ongoing experiments on the optimization of beam transport of laser accelerated particles, secondary experiments may soon be performed with little additional effort, making use of the unique experimental conditions already available at the area.

For a complete beamline concept, the LIGHT beamline may be upgraded by additional focusing devices

⁸ https://www.gsi.de/de/start/beschleuniger/fachabteilungen/linac/projects/proton_linac_for_fair

for optimized beam transport and re-focusing of the bunch behind the cavity. Optional insertion of a dipole magnet provides for additional energy filtering (especially extracting the occurring satellites behind the rf). Finally, the bunch can be lead to a new target chamber for secondary experiments at Z4, combining the LIGHT beamline, the available UNILAC beam and the high energy laser *nhelix*. This combination would enable manifold experimental possibilities in a world-wide unique experimental area. The described layout is illustrated in figure 5.5.

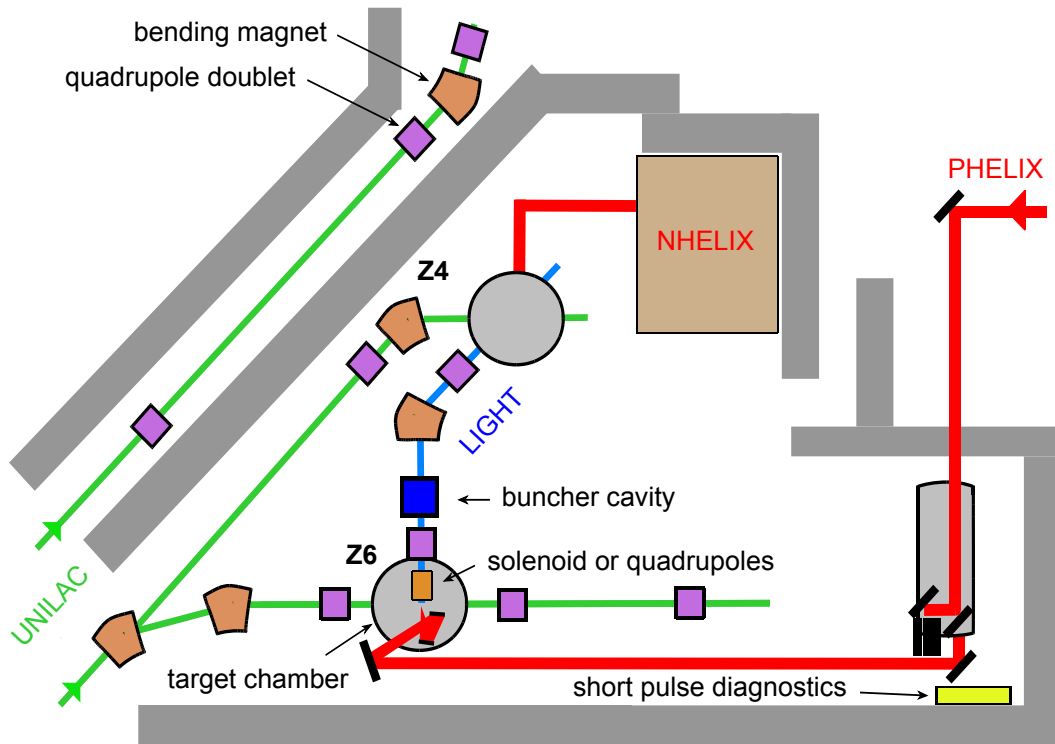


Figure 5.5: Schematic view of a possible new proton beamline at Z4 at GSI's experimental hall. Additional focusing is necessary to keep the transverse bunch dimensions small to avoid further particle losses within the beamline and provide for a tightly focused interaction region in a new target chamber at Z4. An optional dipole bending magnet provides for additional energy cleaning of the bunch behind the cavity. In this new target chamber, also the UNILAC beam and the *nhelix* laser could be available with only small effort and costs, as both systems are available at the site anyways. A versatile testbed for experiments with highest bunch intensities and promising combination possibilities would be the result.



6 Conclusion

In the scope of this thesis, a laser-driven proton beamline was constructed and commissioned at the GSI Helmholtz center for heavy ion research, Darmstadt. The work was performed within the laser and plasma physics group at the institute of nuclear physics of the Technical University of Darmstadt and received great support from the plasma and accelerator physics departments at GSI. The laser-driven beamline represents the central experimental test-bed for the LIGHT collaboration (Laser Ion Generation, Handling and Transport). The main goal of LIGHT is to demonstrate the feasibility of merging novel laser-based ion sources with conventional accelerator infrastructure and therefore provide the essential technological interface necessary for many possible applications.

The beamline was constructed at the Z6 area in the experimental hall of GSI. Z6 is a versatile experimental area with an ion beamline and two laser systems available. The construction of a new laser beamline (PHELIX 100 TW) was finalized at the beginning of this thesis to enable short pulse laser experiments (at $\lambda = 1053$ nm) with PHELIX at Z6 with currently up to 15 Joules of laser energy on target in 650 fs and a focal spot size of $3.5 \times 3.5 \mu\text{m}^2$ (FWHM). Laser-driven ion acceleration via the TNSA mechanism became possible with this beamline at Z6.

The commissioning experiments of the PHELIX 100 TW beamline and the characterization of the TNSA proton source represent the first part of this thesis. The experiments showed the expected continuous exponential proton spectrum and large (energy-dependent) full envelope divergence. Maximum proton energies of 28.4 MeV could be reached at a laser intensity of $6 \times 10^{19} \text{ W/cm}^2$. The energy of interest for the beamline is $E_0 = 10$ MeV and particle numbers of $1.3 \times 10^{10} (\pm 15\%)$ protons were measured in the interval $\Delta E = (10 \pm 0.5)$ MeV. However, the beamline was typically operated below these maximum parameters, thus providing lower particle numbers around 3×10^9 in this energy interval and showing shot-to-shot fluctuations of up to a factor of 3 from source routinely.

A solenoid and the necessary pulsed power system were integrated to collimate the beam and select a specific energy via chromatic focusing. A full characterization of the solenoid and its transport properties concerning the laser accelerated proton beam was performed. 34% of the initial particle numbers in the selected energy interval $\Delta E = (10 \pm 0.5)$ MeV could be captured and beam transport up to 3 m behind the source was demonstrated. The beam was characterized spatially, spectrally and temporally by complementary diagnostics, that had to be improved, adapted or even fully developed within the scope of this thesis to match the experimental conditions at hand: A precise time-of-flight measurement using a thin diamond detector was successfully used for the first time in such an experiment, giving access to high temporal resolution measurements. Furthermore, a compact magnetic dipole spectrometer was specially designed and the *radiochromic imaging spectroscopy* (RIS) - a well known and often used technique in the field of laser-based proton acceleration - was significantly improved with respect to the energy resolution at a high sensitivity level.

Collimated proton bunches with a peaked energy spectrum (with an energy spread of $(18 \pm 3)\%$ at FWHM) around the selected energy (typically $E_0 = 9.6$ MeV) were propagated through the beamline with a measured bunch duration of 8.6 ns and a transverse beam size of $15 \times 15 \text{ mm}^2$ (FWHM) at a position of 3 m to the source.

The fact that the proton beam is expanding within a quasi-neutral plasma had to be addressed, as the co-propagating electrons are getting focused tightly within the solenoid field and influence the proton

transport in such, that axis-near protons of all energies experience an attractive negative on-axis potential. As a consequence, a central focal feature is observed behind the solenoid for other energies than the focal energy, too. This leads to a broadening of the observed energy spectrum. First direct measurements of these co-moving electrons and their spectral shape have been performed within this thesis to quantify their influence on the proton beam and provide a solid basis for further simulation studies.

Finally, the radiofrequency (rf) cavity, running at 108.4 MHz and connected to the UNILAC rf system, was added at a distance of 2 m from the source to perform a rotation in longitudinal phase space and minimize the energy spread of the bunch. Synchronization of the PHELIX laser to the rf could be achieved at a general precision of $\Delta t = \pm 0.3$ ns ($\Delta\Phi_s = \pm 12$ deg) in advance and on-shot a high precision measurement is possible with $\Delta t = \pm 0.05$ ns ($\Delta\Phi_s = \pm 2$ deg). Bunch injection at $\Phi_s = -90$ deg synchronous phase provides for optimum energy compression. In this way, the energy spread of the proton bunch at a central energy of $E_0 = (9.7 \pm 0.1)$ MeV could be reduced from $(18 \pm 3)\%$ to $(2.7 \pm 1.7)\%$ (FWHM), containing 1.7×10^9 ($\pm 15\%$) protons (within FWHM), which is 1/3 of the initial proton numbers in a ± 0.5 MeV interval around the focal energy. The qualitative result of the beam shaping is illustrated in figure 6.1.

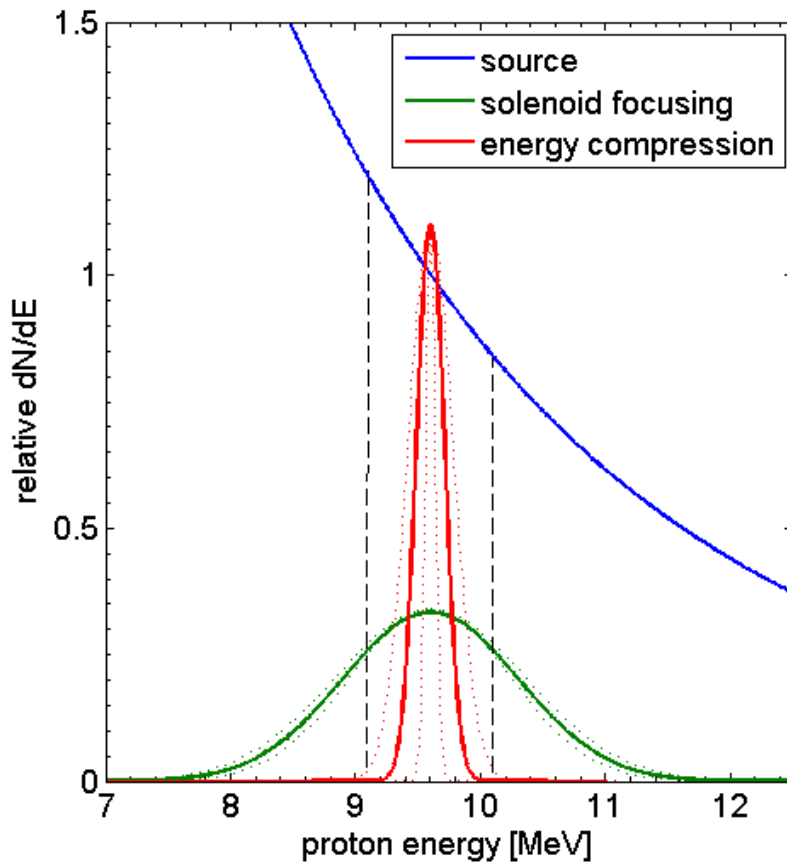


Figure 6.1: The TNSA source provides a highly divergent and continuous (exponentially decaying) proton spectrum (blue). Collimation of a certain (adjustable) energy interval and transportation of the beam is done by the pulsed solenoid, resulting in a broad peaked spectrum (green). Finally, phase rotation and energy compression of the bunch is possible with the rf cavity and a narrow peaked spectrum obtained (red).

Furthermore, the possibility of phase focusing of the bunch could be demonstrated with the current setup by increasing the rf power at an injection phase of $\Phi_s = -90$ deg. Simulations show a possible temporal compression of the bunch to the sub-nanosecond domain, thus reaching highest bunch intensities of 10^{10} protons per nanosecond at 10 MeV proton energy, which represents a particle fluence that is inaccessible today's for conventional accelerators at this energy level.

Additionally to this primary experiments, first results on improving and extending this laser-based proton beamline were obtained. Permanent magnetic quadrupoles (PMQs) represent a possible alternative to the solenoid. In first experiments, 1.7×10^9 ($\pm 6\%$) protons in the energy interval $\Delta E = (5 \pm 0.5)$ MeV energy could be focused to a $1 \times 2 \text{ mm}^2$ (FWHM) spot size at 355 mm distance to the source with a PMQ doublet. These PMQs show excellent ion optical qualities and may simplify the experimental setup drastically due to smaller size and passive operation, thus representing a promising improvement of the beamline.



Zusammenfassung

Im Rahmen der vorliegenden Arbeit, die in der AG Laser- und Plasmaphysik des Instituts für Kernphysik der TU Darmstadt mit Unterstützung der Abteilungen Plasma- und Beschleunigerphysik der GSI durchgeführt wurde, konnte eine lasergetriebene Protonenstrahlführung am GSI Helmholtzzentrum für Schwerionenforschung, Darmstadt, errichtet und charakterisiert werden. Diese neuartige Strahlführung repräsentiert das Kernexperiment der LIGHT Kollaboration (Laser Ion Generation, Handling and Transport), deren Ziel es ist, die Vereinbarkeit lasergetriebener Ionenquellen mit konventionellen Beschleunigerstrukturen zu demonstrieren. Diese technologische Zusammenführung ist essentiell für viele mögliche zukünftige Anwendungen lasergetriebener Ionenstrahlen, für die Strahlformung und Strahltransport unabdingbar sind.

Der Aufbau der Strahlführung wurde am Experimentierplatz Z6 der GSI (E-Halle) unternommen, an welchem bereits eine große Vielzahl an experimentellen Möglichkeiten zur Verfügung steht. Zu Beginn dieser Arbeit wurde zunächst eine neue Laserstrahlführung fertiggestellt (PHELIX 100 TW), um Femtosekunden-Kurzpulse an Z6 für Experimente zu nutzen. Mit ihr können derzeit in der Z6 Targetkammer bei einer zentralen Wellenlänge von $\lambda=1053$ nm bis zu 15 J Laserenergie in 650 fs Pulsdauer auf eine Fläche von $3.5 \times 3.5 \mu\text{m}^2$ (FWHM) fokussiert werden. Dies ermöglicht lasergetriebene Ionenbeschleunigung im TNSA Regime.

Eine vollständige Charakterisierung der Strahlparameter seitens der TNSA-getriebenen Protonenquelle an Z6 definierte die verfügbaren Quellparameter. Die Experimente zeigten wie erwartet ein kontinuierliches, exponentiell abfallendes Protonenspektrum mit energieabhängigem Divergenzwinkel von bis zu 25° . Bei einer Laserintensität von $6 \times 10^{19} \text{ W/cm}^2$ konnten Protonenmaximalenergien von 28.4 MeV gemessen werden und im für die Strahlführung relevanten Energieintervall $\Delta E=(10 \pm 0.5) \text{ MeV}$ betrug die Teilchenzahl 1.3×10^{10} ($\pm 15\%$). Im Routinebetrieb wurden allerdings reduzierte Laserenergien gegenüber dem technischen Maximum genutzt, sodass im selben Energieintervall stattdessen typischerweise 3×10^9 Protonen verfügbar waren. Zudem sind Schuss-zu-Schuss Fluktuationen beobachtet worden, die Abweichungen von bis zu einem Faktor 3 in der Teilchenzahl einschlossen.

Das Kernelement zu Strahlkollimierung und Energieselektion (via chromatischer Fokussierung) stellte ein gepulster Solenoid dar (inkl. nötiger Infrastruktur). Mit ihm war es möglich, 34% der von der Quelle verfügbaren Protonen im Energieintervall $\Delta E=(10 \pm 0.5) \text{ MeV}$ einzufangen und durch die gesamte Strahlführung auf eine Distanz zur Quelle von 3 m zu fokussieren. Eine räumliche, zeitliche und spektrale Untersuchung des transportierten Protonenstrahls wurde an dieser Stelle unternommen und ergab einen 8.6 ns langen, $15 \times 15 \text{ mm}^2$ großen (FWHM) Protonenstrahl mit zentraler Energie $E_0=9.6 \text{ MeV}$ und $(18 \pm 3)\%$ Energieunschärfe (FWHM). Im Rahmen der vorliegenden Arbeit wurden dazu die vorhandenen Methoden zur Strahldiagnostik erweitert: Es wurde die Möglichkeit zur präzisen Flugzeitmessung mit einem Diamantdetektor erstmalig für ein solches Experiment eingeführt, ein kompaktes Dipolspektrometer entwickelt und die *Radiochromic Imaging Spectroscopy* für eine erhöhte Energieauflösung verbessert bei gleichzeitig hoher Sensitivität.

Für den Strahltransport durch den Solenoiden muss berücksichtigt werden, dass von der lasergetriebenen Quelle ein (elektrisch) quasineutraler Teilchenstrom expandiert. Die diese Ladungsneutralität gewährleistenden Elektronen, die mit den Protonen propagieren, werden vom Magnetfeld des Solenoiden stark beeinflusst und auf die Symmetrieachse fokussiert. Hier bilden sie ein negatives Potenzial,

welches achsnahe Protonen anzieht. Dies bewirkt eine zusätzliche Fokussierung der Protonen und führt hinter dem Solenoiden zu einer beobachteten erhöhten Protonenzahl nahe der Symmetrieachse für alle Protonenenergien. Zur Quantifizierung des Effekts wurden erste Messungen des Spektrums und der Absolutzahlen dieser mitpropagierenden Elektronen durchgeführt, welche nun als Grundlage für weitere Simulationsstudien dienen.

Die Vervollständigung der neuen Strahlführung bestand schließlich in der Implementierung einer Radiofrequenz-(RF)-Kavität zur Durchführung einer (longitudinalen) Phasenraumrotation. Sie befindet sich in einem Abstand von 2 m zur Quelle und ist mit der RF-Versorgung des UNILAC verbunden (108.4 MHz). Eine Synchronisation mit dem PHELIX Laser ist derzeit mit einer Genauigkeit von $\Delta t = \pm 0.3$ ns ($\Delta \Phi_s = \pm 12$ deg) möglich. Eine genauere relative Phasenlage kann während des Experimentschusses bestimmt werden ($\Delta t = \pm 0.05$ ns bzw. $\Delta \Phi_s = \pm 2$ deg). Die Injektion des Protonenstrahls in die Kavität bei einer synchronen Phase von $\Phi_s = -90$ deg bewirkt eine Minimierung der Energieunschärfe und ist der geplante Arbeitspunkt der neuen Strahlführung. Dadurch war es möglich, Protonenstrahlen mit einer zentralen Energie von $E_0 = (9.7 \pm 0.1)$ MeV zu erzeugen, welche eine deutlich reduzierte Energieunschärfe von $(18 \pm 3)\%$ auf $(2.7 \pm 1.7)\%$ (FWHM) zeigen. Die Teilchenzahl innerhalb des FWHM betrug 1.7×10^9 ($\pm 15\%$), was etwa einem Drittel der Anzahl entspricht, die von der Quelle in einem Energiebereich von ± 0.5 MeV um die selektierte Energie inertial verfügbar ist. Das Ergebnis der gesamten vorgenommenen Strahlformung ist in 6.2 skizziert.

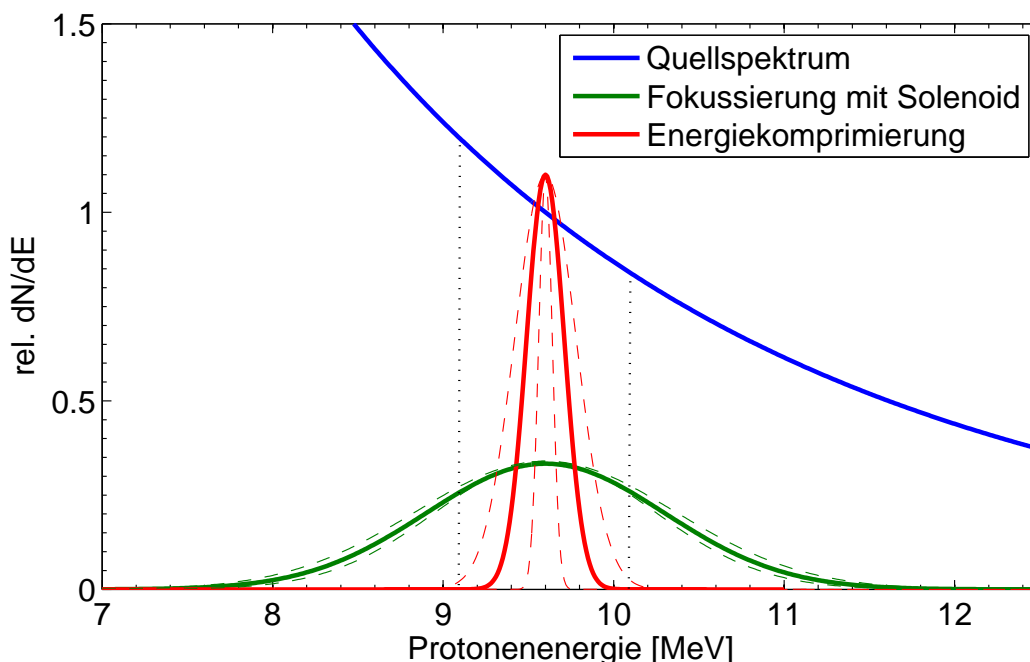


Abbildung 6.2: Die TNSA Quelle liefert ein divergentes, kontinuierliches Protonenspektrum (blau). Mit dem Solenoiden wird ein (wählbares) Energieintervall selektiert, kollimiert und durch die Strahlführung transportiert. Durch diesen chromatischen Filter erhält man in 3 m Entfernung zur Quelle ein um die selektierte Energie zentriertes breites Spektrum (grün), welches durch die Kavität mittels Energiekompression zu einem schmalen und intensiven Spektrum verringert werden kann (rot).

Desweiteren konnte mit dem aktuellen Aufbau gezeigt werden, dass eine *Überrotation* im Phasenraum möglich ist und damit eine Phasenfokussierung. Simulationen sagen Pulslängen im Bereich von weniger als einer Nanosekunde voraus und damit erreichbare Protonenflüsse von 10^{10} Protonen pro Nanosekunde (bei einer zentralen Energie von 10 MeV). Diese hohen Teilchenflüsse können mit derzeitigen konventionellen Beschleunigerstrukturen in diesem Energiebereich nicht erreicht werden und bieten damit einmalige Experimentierparameter.

Neben diesem Hauptexperiment konnten auch erste Untersuchungen mit Permanentmagnet-Quadrupolen (PMQs) als Alternative zum gepulsten Solenoiden durchgeführt werden. Mit Hilfe eines PMQ Doublets wurden Protonen im Energieintervall (5 ± 0.5) MeV von der TNSA Quelle selektiert und in einer Entfernung von 355 mm fokussiert. Die Fokusgröße betrug $1 \times 2 \text{ mm}^2$ (FWHM) und es waren 1.7×10^9 ($\pm 6\%$) Protonen in diesem Energieintervall vorhanden. Ihre passive Arbeitsweise und besseren ionenoptischen Eigenschaften machen den Einsatz von PMQs zu einer vielversprechenden Alternative für die LIGHT Strahlführung.



I References

- [Almomani et al., 2012] Almomani, A., Droba, M., Ratzinger, U., and Hofmann, I. (2012). Matching the laser generated p bunch into a crossbar- h drift tube linac. *Phys. Rev. ST Accel. Beams*, 15:051302.
- [Aurand et al., 2013] Aurand, B., Kuschel, S., Jäckel, O., Rödel, C., Zhao, H., Herzer, S., Paz, A. E., Bierbach, J., Polz, J., Elkin, B., Paulus, G. G., Karmakar, A., Gibbon, P., Kuehl, T., and Kaluza, M. C. (2013). Radiation pressure-assisted acceleration of ions using multi-component foils in high-intensity laser-matter interactions. *New Journal of Physics*, 15(3):033031.
- [Bagnoud et al., 2010] Bagnoud, V., Aurand, B., Blazevic, A., Borneis, S., Bruske, C., Ecker, B., Eisenbarth, U., Fils, J., Frank, A., Gaul, E., Goette, S., Haefner, C., Hahn, T., Harres, K., Heuck, H.-M., Hochhaus, D., Hoffmann, D., Javorkova, D., Kluge, H.-J., Kuehl, T., Kunzer, S., Kreutz, M., Merz-Mantwill, T., Neumayer, P., Onkels, E., Reemts, D., Rosmej, O., Roth, M., Stoehlker, T., Tauschwitz, A., Zielbauer, B., Zimmer, D., and Witte, K. (2010). Commissioning and early experiments of the phelix facility. *Applied Physics B: Lasers and Optics*, 100:137–150. 10.1007/s00340-009-3855-7.
- [Bartal et al., 2012] Bartal, T., Foord, M. E., Bellei, C., Key, M. H., Flippo, K. A., Gaillard, S. A., Offermann, D. T., Patel, P. K., Jarrott, L. C., Higginson, D. P., Roth, M., Otten, A., Kraus, D., Stephens, R. B., McLean, H. S., Giraldez, E. M., Wei, M. S., Gautier, D. C., and Beg, F. N. (2012). Focusing of short-pulse high-intensity laser-accelerated proton beams. *Nat Phys*, 8(2):139–142.
- [Bauer et al., 1995] Bauer, D., Mulser, P., and Steeb, W. H. (1995). Relativistic ponderomotive force, uphill acceleration, and transition to chaos. *Phys. Rev. Lett.*, 75:4622–4625.
- [Borghesi et al., 2001] Borghesi, M., Schiavi, A., Campbell, D. H., Haines, M. G., Willi, O., MacKinnon, A. J., Gizzi, L. A., Galimberti, M., Clarke, R. J., and Ruhl, H. (2001). Proton imaging: a diagnostic for inertial confinement fusion/fast ignitor studies. *Plasma Physics and Controlled Fusion*, 43(12A):A267.
- [Brabetz et al., 2012] Brabetz, C., Eisenbarth, U., Kester, O., Stöhlker, T., Cowan, T., Zielbauer, B., and Bagnoud, V. (2012). Hollow beam creation with continuous diffractive phase mask at phelix. In *Conference on Lasers and Electro-Optics 2012*, page JTU1K.5. Optical Society of America.
- [Burriss-Mog, 2012] Burriss-Mog, T. (2012). *Capture and Transport of Laser Accelerated Protons by Pulsed Magnetic Fields: Advancements Toward Laser-Based Proton Therapy*. PhD thesis, University of Nevada, Reno.
- [Burriss-Mog et al., 2011] Burriss-Mog, T., Harres, K., Nürnberg, F., Busold, S., Bussmann, M., Deppert, O., Hoffmeister, G., Joost, M., Sobiella, M., Tauschwitz, A., Zielbauer, B., Bagnoud, V., Herrmannsdoerfer, T., Roth, M., and Cowan, T. E. (2011). Laser accelerated protons captured and transported by a pulse power solenoid. *Phys. Rev. ST Accel. Beams*, 14:121301.
- [Busold, 2010] Busold, S. (2010). Konstruktion und einatz eines magnetspektrometers zur untersuchung des niederenergetischen elektronenteils [1...30kev] bei der laser-protonenbeschleunigung. Master's thesis, TU Darmstadt.
- [Busold et al., 2014a] Busold, S., Almomani, A., Bagnoud, V., Barth, W., Bedacht, S., Blazevic, A., Boine-Frankenheim, O., Brabetz, C., Burriss-Mog, T., Cowan, T., Deppert, O., Droba, M., Eickhoff, H., Eisenbarth, U., Harres, K., Hoffmeister, G., Hofmann, I., Jaeckel, O., Jaeger, R., Joost, M., Kraft, S., Kroll, F., Kaluza, M., Kester, O., Lecz, Z., Merz, T., Nürnberg, F., Al-Omari, H., Orzhekhovskaya, A., Paulus, G., Polz, J., Ratzinger, U., Roth, M., Schaumann, G., Schmidt, P., Schramm, U., Schreiber, G., Schumacher, D., Stoehlker, T., Tauschwitz, A., Vinzenz, W., Wagner, F., Yaramyshev, S., and Zielbauer, B. (2014a). Shaping laser accelerated ions for future applications - the light collaboration. *Nuclear Instruments*

and Methods in Physics Research Section A: Accelerators, Spectrometers, Detectors and Associated Equipment, 740(0):94 – 98. Proceedings of the first European Advanced Accelerator Concepts Workshop 2013.

- [Busold et al., 2013] Busold, S., Schumacher, D., Deppert, O., Brabetz, C., Frydrych, S., Kroll, F., Joost, M., Al-Omari, H., Blažević, A., Zielbauer, B., Hofmann, I., Bagnoud, V., Cowan, T. E., and Roth, M. (2013). Focusing and transport of high-intensity multi-mev proton bunches from a compact laser-driven source. *Phys. Rev. ST Accel. Beams*, 16:101302.
- [Busold et al., 2014b] Busold, S., Schumacher, D., Deppert, O., Brabetz, C., Kroll, F., Blažević, A., Bagnoud, V., and Roth, M. (2014b). Commissioning of a compact laser-based proton beam line for high intensity bunches around 10¹⁴mev. *Phys. Rev. ST Accel. Beams*, 17:031302.
- [Carroll et al., 2010] Carroll, D., Brummitt, P., Neely, D., Lindau, F., Lundh, O., Wahlström, C.-G., and McKenna, P. (2010). A modified thomson parabola spectrometer for high resolution multi-mev ion measurements—application to laser-driven ion acceleration. *Nuclear Instruments and Methods in Physics Research Section A: Accelerators, Spectrometers, Detectors and Associated Equipment*, 620(1):23 – 27. COULOMB09 - Ions Acceleration with high Power Lasers: Physics and Applications.
- [Carroll et al., 2009] Carroll, D. C., Batani, D., Evans, R. G., Glinec, Y., Homann, C., Jafer, R., Kar, S., Lindau, F., Lundh, O., Markey, K., Neely, D., Nürnberg, F., Persson, A., Quinn, M. N., Robinson, A. P., Roth, M., Wahlström, C.-G., Yuan, X., Zepf, M., and McKenna, P. (2009). Dynamic control and enhancement of laser-accelerated protons using multiple laser pulses. *Comptes Rendus Physique*, 10(2-3):188 – 196. Laser acceleration of particles in plasma.
- [Cayzac, 2009] Cayzac, W. (2009). Entwicklung eines cvd-diamant-spektrometers zur messung von ladungszuständen von schwerionen in lasererzeugtem plasma. Master’s thesis, TU Darmstadt.
- [Cayzac et al., 2013] Cayzac, W., Frank, A., Schumacher, D., Roth, M., Blazevic, A., Wamers, F., Trager, M., Berdermann, E., Voss, B., and Hessling, T. (2013). A spectrometer on chemical vapour deposition-diamond basis for the measurement of the charge-state distribution of heavy ions in a laser-generated plasma. *Review of Scientific Instruments*, 84(4):043301.
- [cea, 2013] cea (2013). Tracewin, <http://irfu.cea.fr/sacm/logiciels/index3.php>.
- [Ceccotti et al., 2007] Ceccotti, T., Lévy, A., Popescu, H., Réau, F., D’Oliveira, P., Monot, P., Geindre, J. P., Lefebvre, E., and Martin, P. (2007). Proton acceleration with high-intensity ultrahigh-contrast laser pulses. *Phys. Rev. Lett.*, 99:185002.
- [Chen et al., 2008] Chen, H., Back, N. L., Bartal, T., Beg, F. N., Eder, D. C., Link, A. J., MacPhee, A. G., Ping, Y., Song, P. M., Throop, A., and Van Woerkom, L. (2008). Absolute calibration of image plates for electrons at energy between 100kev and 4mev. *Review of Scientific Instruments*, 79(3):–.
- [Clark et al., 2000] Clark, E. L., Krushelnick, K., Davies, J. R., Zepf, M., Tatarakis, M., Beg, F. N., Machacek, A., Norreys, P. A., Santala, M. I. K., Watts, I., and Dangor, A. E. (2000). Measurements of energetic proton transport through magnetized plasma from intense laser interactions with solids. *Phys. Rev. Lett.*, 84:670–673.
- [Cowan et al., 2004] Cowan, T. E., Fuchs, J., Ruhl, H., Kemp, A., Audebert, P., Roth, M., Stephens, R., Barton, I., Blazevic, A., Brambrink, E., Cobble, J., Fernández, J., Gauthier, J.-C., Geissel, M., Hegelich, M., Kaae, J., Karsch, S., Le Sage, G. P., Letzring, S., Manclossi, M., Meyroneinc, S., Newkirk, A., Pépin, H., and Renard-LeGalloudec, N. (2004). Ultralow emittance, multi-mev proton beams from a laser virtual-cathode plasma accelerator. *Phys. Rev. Lett.*, 92:204801.

-
- [Crow et al., 1975] Crow, J. E., Auer, P. L., and Allen, J. E. (1975). The expansion of a plasma into a vacuum. *Journal of Plasma Physics*, 14(01):65–76.
- [CST, 2013] CST (2013). Cst, <https://www.cst.com/>.
- [Daido et al., 2012] Daido, H., Nishiuchi, M., and Pirozhkov, A. S. (2012). Review of laser-driven ion sources and their applications. *Reports on Progress in Physics*, 75(5):056401.
- [Davies, 2006] Davies, J. R. (2006). The alfvén limit revisited and its relevance to laser-plasma interactions. *Laser and Particle Beams*, 24:299–310.
- [Diaw and Mora, 2011] Diaw, A. and Mora, P. (2011). Rarefaction shock in plasma with a bi-maxwellian electron distribution function. *Phys. Rev. E*, 84:036402.
- [Diaw and Mora, 2012] Diaw, A. and Mora, P. (2012). Thin-foil expansion into a vacuum with a two-temperature electron distribution function. *Phys. Rev. E*, 86:026403.
- [Drude, 1897] Drude, P. (1897). Ueber fernwirkungen. *Annalen der Physik*, 298(12):I–XLIX.
- [Dyer et al., 2008] Dyer, G. M., Bernstein, A. C., Cho, B. I., Osterholz, J., Grigsby, W., Dalton, A., Shepherd, R., Ping, Y., Chen, H., Widmann, K., and Ditmire, T. (2008). Equation-of-state measurement of dense plasmas heated with fast protons. *Phys. Rev. Lett.*, 101:015002.
- [Ellison and Fuchs, 2010] Ellison, C. L. and Fuchs, J. (2010). Optimizing laser-accelerated ion beams for a collimated neutron source. *Physics of Plasmas*, 17(11):113105.
- [Esarey et al., 1995] Esarey, E., Sprangle, P., and Krall, J. (1995). Laser acceleration of electrons in vacuum. *Phys. Rev. E*, 52:5443–5453.
- [Esirkepov et al., 2004] Esirkepov, T., Borghesi, M., Bulanov, S. V., Mourou, G., and Tajima, T. (2004). Highly efficient relativistic-ion generation in the laser-piston regime. *Phys. Rev. Lett.*, 92:175003.
- [Flippo et al., 2006] Flippo, K., Hegelich, B., Schmitt, M., Meserole, C., Fisher, G., Gautier, D., Cobble, J., Johnson, R., Letzring, S., Schreiber, J., Schollmeier, M., and Fernández, J. (2006). Ultrashort-laser-produced heavy ion generation via target laser-ablation cleaning. *J. Phys. IV France*, 133:1117–1122.
- [Fuchs et al., 2006] Fuchs, J., Antici, P., d’Humieres, E., Lefebvre, E., Borghesi, M., Brambrink, E., Cecchetti, C. A., Kaluza, M., Malka, V., Manclossi, M., Meyroneinc, S., Mora, P., Schreiber, J., Toncian, T., Pepin, H., and Audebert, P. (2006). Laser-driven proton scaling laws and new paths towards energy increase. *Nat Phys*, 2(1):48–54.
- [Fuchs et al., 2007] Fuchs, J., Sentoku, Y., d’Humieres, E., Cowan, T. E., Cobble, J., Audebert, P., Kemp, A., Nikroo, A., Antici, P., Brambrink, E., Blazevic, A., Campbell, E. M., Fernandez, J. C., Gauthier, J.-C., Geissel, M., Hegelich, M., Karsch, S., Popescu, H., Renard-LeGalloudec, N., Roth, M., Schreiber, J., Stephens, R., and Pépin, H. (2007). Comparative spectra and efficiencies of ions laser-accelerated forward from the front and rear surfaces of thin solid foils. *Physics of Plasmas (1994-present)*, 14(5):–.
- [Fuchs et al., 2005] Fuchs, J., Sentoku, Y., Karsch, S., Cobble, J., Audebert, P., Kemp, A., Nikroo, A., Antici, P., Brambrink, E., Blazevic, A., Campbell, E. M., Fernández, J. C., Gauthier, J.-C., Geissel, M., Hegelich, M., Pépin, H., Popescu, H., Renard-LeGalloudec, N., Roth, M., Schreiber, J., Stephens, R., and Cowan, T. E. (2005). Comparison of laser ion acceleration from the front and rear surfaces of thin foils. *Phys. Rev. Lett.*, 94(4):045004.
- [Fujioka et al., 2013] Fujioka, S., Zhang, Z., Ishihara, K., Shigemori, K., Hironaka, Y., Johzaki, T., Sunahara, A., Yamamoto, N., Nakashima, H., Watanabe, T., Shiraga, H., Nishimura, H., and Azechi, H. (2013). KiloTesla magnetic field due to a capacitor-coil target driven by high power laser. *Sci. Rep.*, 3:–.

-
- [Gibbon, 2005] Gibbon, P. (2005). *Short Pulse Laser Interactions with Matter*. Imperial College Press.
- [Gitomer et al., 1986] Gitomer, S. J., Jones, R. D., Begay, F., Ehler, A. W., Kephart, J. F., and Kristal, R. (1986). Fast ions and hot electrons in the laser-plasma interaction. *Physics of Fluids*, 29(8):2679–2688.
- [Gunther et al., 2013] Gunther, M. M., Britz, A., Clarke, R. J., Harres, K., Hoffmeister, G., Nurnberg, F., Otten, A., Pelka, A., Roth, M., and Vogt, K. (2013). Nais: Nuclear activation-based imaging spectroscopy. *Review of Scientific Instruments*, 84(7):073305.
- [Haberberger et al., 2012] Haberberger, D., Tochitsky, S., Fiuza, F., Gong, C., Fonseca, R. A., Silva, L. O., Mori, W. B., and Joshi, C. (2012). Collisionless shocks in laser-produced plasma generate monoenergetic high-energy proton beams. *Nat Phys*, 8(1):95–99.
- [Hargrove et al., 1964] Hargrove, L. E., Fork, R. L., and Pollack, M. A. (1964). Locking of he-ne laser modes induced by synchronous intracavity modulation. *Applied Physics Letters*, 5(1):4–5.
- [Harres, 2010] Harres, K. (2010). *Strahltransport laserbeschleunigter Ionen*. PhD thesis, TU Darmstadt.
- [Harres et al., 2010] Harres, K., Alber, I., Tauschwitz, A., Bagnoud, V., Daido, H., Gunther, M., Nurnberg, F., Otten, A., Schollmeier, M., Schutrumpf, J., Tampo, M., and Roth, M. (2010). Beam collimation and transport of quasineutral laser-accelerated protons by a solenoid field. *Physics of Plasmas*, 17(2):023107.
- [Harres et al., 2008] Harres, K., Schollmeier, M., Brambrink, E., Audebert, P., Blazevic, A., Flippo, K., Gautier, D. C., Geissel, M., Hegelich, B. M., Nurnberg, F., Schreiber, J., Wahl, H., and Roth, M. (2008). Development and calibration of a thomson parabola with microchannel plate for the detection of laser-accelerated mev ions. *Review of Scientific Instruments*, 79(9):093306.
- [Hatchett et al., 2000] Hatchett, S. P., Brown, C. G., Cowan, T. E., Henry, E. A., Johnson, J. S., Key, M. H., Koch, J. A., Langdon, A. B., Lasinski, B. F., Lee, R. W., Mackinnon, A. J., Pennington, D. M., Perry, M. D., Phillips, T. W., Roth, M., Sangster, T. C., Singh, M. S., Snavely, R. A., Stoyer, M. A., Wilks, S. C., and Yasuike, K. (2000). Electron, photon, and ion beams from the relativistic interaction of petawatt laser pulses with solid targets. *Physics of Plasmas*, 7(5):2076–2082.
- [Häuser, 1989] Häuser, J. (1989). *Eigenschaften von Spiralresonatoren*. PhD thesis, Universität Frankfurt.
- [Hegelich et al., 2006] Hegelich, B. M., Albright, B. J., Cobble, J., Flippo, K., Letzring, S., Paffett, M., Ruhl, H., Schreiber, J., Schulze, R. K., and Fernandez, J. C. (2006). Laser acceleration of quasi-monoenergetic mev ion beams. *Nature*, 439(7075):441–444.
- [Hegelich et al., 2002] Hegelich, M., Karsch, S., Pretzler, G., Habs, D., Witte, K., Guenther, W., Allen, M., Blazevic, A., Fuchs, J., Gauthier, J. C., Geissel, M., Audebert, P., Cowan, T., and Roth, M. (2002). Mev ion jets from short-pulse-laser interaction with thin foils. *Phys. Rev. Lett.*, 89:085002.
- [Hinterberger, 2008] Hinterberger, F. (2008). *Physik der Teilchenbeschleuniger und Ionenoptik, 2. Auflage*. Springer.
- [Hoffmeister et al., 2013] Hoffmeister, G., Bellei, C., Harres, K., Ivanov, D., Kraus, D., Pelka, A., Rethfeld, B., Schaumann, G., and Roth, M. (2013). Influence of fs-laser desorption on target normal sheath accelerated ions. *Phys. Rev. ST Accel. Beams*, 16:041304.
- [Hofmann, 2013] Hofmann, I. (2013). Performance of solenoids versus quadrupoles in focusing and energy selection of laser accelerated protons. *Phys. Rev. ST Accel. Beams*, 16:041302.

-
- [Hofmann et al., 2012] Hofmann, I., ter Vehn, J. M., Yan, X., and Al-Omari, H. (2012). Chromatic energy filter and characterization of laser-accelerated proton beams for particle therapy. *Nuclear Instruments and Methods in Physics Research Section A: Accelerators, Spectrometers, Detectors and Associated Equipment*, 681(0):44 – 54.
- [Ikegami et al., 2009] Ikegami, M., Nakamura, S., Iwashita, Y., Shirai, T., Souda, H., Tajima, Y., Tanabe, M., Tongu, H., Itoh, H., Shintaku, H., Yamazaki, A., Daido, H., Yogo, A., Orimo, S., Mori, M., Nishiuchi, M., Ogura, K., Sagisaka, A., Pirozhkov, A. S., Kiriyama, H., Kanazawa, S., Kondo, S., Yamamoto, Y., Shimomura, T., Tanoue, M., Nakai, Y., Akutsu, A., Bulanov, S. V., Kimura, T., Oishi, Y., Nemoto, K., Tajima, T., and Noda, A. (2009). Radial focusing and energy compression of a laser-produced proton beam by a synchronous rf field. *Phys. Rev. ST Accel. Beams*, 12:063501.
- [Izumi et al., 2006] Izumi, N., Snavely, R., Gregori, G., Koch, J. A., Park, H.-S., and Remington, B. A. (2006). Application of imaging plates to x-ray imaging and spectroscopy in laser plasma experiments (invited). *Review of Scientific Instruments*, 77(10):10E325.
- [Jahn, 2013] Jahn, D. (2013). Spektrale untersuchung der heissen elektronen bei der laser-teilchenbeschleunigung. Bachelor thesis.
- [Jung et al., 2013] Jung, D., Falk, K., Guler, N., Deppert, O., Devlin, M., Favalli, A., Fernandez, J. C., Gautier, D. C., Geissel, M., Haight, R., Hamilton, C. E., Hegelich, B. M., Johnson, R. P., Merrill, F., Schaumann, G., Schoenberg, K., Schollmeier, M., Shimada, T., Taddeucci, T., Tybo, J. L., Wender, S. A., Wilde, C. H., Wurden, G. A., and Roth, M. (2013). Characterization of a novel, short pulse laser-driven neutron source. *Physics of Plasmas (1994-present)*, 20(5):-.
- [Jung et al., 2011] Jung, D., Hörlein, R., Gautier, D. C., Letzring, S., Kiefer, D., Allinger, K., Albright, B. J., Shah, R., Palaniyappan, S., Yin, L., Fernández, J. C., Habs, D., and Hegelich, B. M. (2011). A novel high resolution ion wide angle spectrometer. *Review of Scientific Instruments*, 82(4):-.
- [Karsch et al., 2003] Karsch, S., Düsterer, S., Schwoerer, H., Ewald, F., Habs, D., Hegelich, M., Pretzler, G., Pukhov, A., Witte, K., and Sauerbrey, R. (2003). High-intensity laser induced ion acceleration from heavy-water droplets. *Phys. Rev. Lett.*, 91(1):015001.
- [Key et al., 1998] Key, M. H., Cable, M. D., Cowan, T. E., Estabrook, K. G., Hammel, B. A., Hatchett, S. P., Henry, E. A., Hinkel, D. E., Kilkenny, J. D., Koch, J. A., Kruer, W. L., Langdon, A. B., Lasinski, B. F., Lee, R. W., MacGowan, B. J., MacKinnon, A., Moody, J. D., Moran, M. J., Offenberger, A. A., Pennington, D. M., Perry, M. D., Phillips, T. J., Sangster, T. C., Singh, M. S., Stoyer, M. A., Tabak, M., Tietbohl, G. L., Tsukamoto, M., Wharton, K., and Wilks, S. C. (1998). Hot electron production and heating by hot electrons in fast ignitor research. *Physics of Plasmas (1994-present)*, 5(5):1966–1972.
- [Kluge et al., 2010] Kluge, T., Enghardt, W., Kraft, S. D., Schramm, U., Zeil, K., Cowan, T. E., and Bussmann, M. (2010). Enhanced laser ion acceleration from mass-limited foils. *Physics of Plasmas (1994-present)*, 17(12):-.
- [Kroll et al., 2013] Kroll, F., Pawelke, J., and Karsch, L. (2013). Preliminary investigations on the determination of three-dimensional dose distributions using scintillator blocks and optical tomography. *Medical Physics*, 40(8):-.
- [Kumar, 2009] Kumar, V. (2009). Understanding the focusing of charged particle beams in a solenoid magnetic field. *American Journal of Physics*, 77(8):737–741.
- [Lecz, 2013] Lecz, Z. (2013). *Laser ion acceleration from a double-layer metal foil*. PhD thesis, TU Darmstadt.

-
- [Lecz et al., 2013] Lecz, Z., Boine-Frankenheim, O., and Kornilov, V. (2013). Target normal sheath acceleration for arbitrary proton layer thickness. *Nuclear Instruments and Methods in Physics Research Section A: Accelerators, Spectrometers, Detectors and Associated Equipment*, 727(0):51 – 58.
- [Ledingham et al., 2004] Ledingham, K. W. D., McKenna, P., McCanny, T., Shimizu, S., Yang, J. M., Robson, L., Zweit, J., Gillies, J. M., Bailey, J., Chimon, G. N., Clarke, R. J., Neely, D., Norreys, P. A., Collier, J. L., Singhal, R. P., Wei, M. S., Mangles, S. P. D., Nilson, P., Krushelnick, K., and Zepf, M. (2004). High power laser production of short-lived isotopes for positron emission tomography. *Journal of Physics D: Applied Physics*, 37(16):2341.
- [Li et al., 2005] Li, Z., Nakamura, S., Fukumi, A., Hayashi, Y., Orimo, S., Nishiuchi, M., Sagisaka, A., Mori, M., Shirai, T., Iwashita, Y., Noda, A., and Daido, H. (2005). Electron energy spectrometer for laser-driven energetic electron generation. *Japanese Journal of Applied Physics*, 44(9A):6796–6800.
- [Linz and Alonso, 2007] Linz, U. and Alonso, J. (2007). What will it take for laser driven proton accelerators to be applied to tumor therapy? *Phys. Rev. ST Accel. Beams*, 10:094801.
- [Macchi, 2013] Macchi, A. (2013). *A Superintense Laser-Plasma Interaction Theory Primer*. Springer-Briefs in Physics.
- [Mackinnon et al., 2001] Mackinnon, A. J., Borghesi, M., Hatchett, S., Key, M. H., Patel, P. K., Campbell, H., Schiavi, A., Snavely, R., Wilks, S. C., and Willi, O. (2001). Effect of plasma scale length on multi-mev proton production by intense laser pulses. *Phys. Rev. Lett.*, 86:1769–1772.
- [Mackinnon et al., 2006] Mackinnon, A. J., Patel, P. K., Borghesi, M., Clarke, R. C., Freeman, R. R., Habara, H., Hatchett, S. P., Hey, D., Hicks, D. G., Kar, S., Key, M. H., King, J. A., Lancaster, K., Neely, D., Nikkro, A., Norreys, P. A., Notley, M. M., Phillips, T. W., Romagnani, L., Snavely, R. A., Stephens, R. B., and Town, R. P. J. (2006). Proton radiography of a laser-driven implosion. *Phys. Rev. Lett.*, 97:045001.
- [Mackinnon et al., 2004] Mackinnon, A. J., Patel, P. K., Town, R. P., Edwards, M. J., Phillips, T., Lerner, S. C., Price, D. W., Hicks, D., Key, M. H., Hatchett, S., Wilks, S. C., Borghesi, M., Romagnani, L., Kar, S., Toncian, T., Pretzler, G., Willi, O., Koenig, M., Martinolli, E., Lepape, S., Benuzzi-Mounaix, A., Audebert, P., Gauthier, J. C., King, J., Snavely, R., Freeman, R. R., and Boehlly, T. (2004). Proton radiography as an electromagnetic field and density perturbation diagnostic (invited). *Review of Scientific Instruments*, 75(10):3531–3536.
- [Mackinnon et al., 2002] Mackinnon, A. J., Sentoku, Y., Patel, P. K., Price, D. W., Hatchett, S., Key, M. H., Andersen, C., Snavely, R., and Freeman, R. R. (2002). Enhancement of proton acceleration by hot-electron recirculation in thin foils irradiated by ultraintense laser pulses. *Phys. Rev. Lett.*, 88:215006.
- [Maiman, 1960] Maiman, T. H. (1960). Stimulated optical radiation in ruby. *Nature*, 187(4736):493–494.
- [Maksimchuk et al., 2000] Maksimchuk, A., Gu, S., Flippo, K., Umstadter, D., and Bychenkov, V. Y. (2000). Forward ion acceleration in thin films driven by a high-intensity laser. *Phys. Rev. Lett.*, 84:4108–4111.
- [Malka and Miquel, 1996] Malka, G. and Miquel, J. L. (1996). Experimental confirmation of ponderomotive-force electrons produced by an ultrarelativistic laser pulse on a solid target. *Phys. Rev. Lett.*, 77(1):75–78.
- [Margarone et al., 2012] Margarone, D., Klimo, O., Kim, I. J., Prokūpek, J., Limpouch, J., Jeong, T. M., Mocek, T., Pšikal, J., Kim, H. T., Proška, J., Nam, K. H., Štolcová, L., Choi, I. W., Lee, S. K., Sung, J. H., Yu, T. J., and Korn, G. (2012). Laser-driven proton acceleration enhancement by nanostructured foils. *Phys. Rev. Lett.*, 109:234801.

-
- [Marjoribanks et al., 2008] Marjoribanks, R., Servol, M., Lecherbourg, L., Forrester, P., Levy, H., McKinney, L., Teeple, B., Candela, Y., Kieffer, J.-C., Moal, S. L., Kulcsár, G., Sipe, J., Audebert, P., Geindre, J.-P., Héron, A., and Adam, J.-C. (2008). Theory and experiment in ultraintense laser-matter interaction in nanostructured ni-nanowire target. In *Conference on Lasers and Electro-Optics/Quantum Electronics and Laser Science Conference and Photonic Applications Systems Technologies*, page JWB6. Optical Society of America.
- [McClung and Hellwarth, 1962] McClung, F. J. and Hellwarth, R. W. (1962). Giant optical pulsations from ruby. *Journal of Applied Physics*, 33(3):828–829.
- [Meadowcroft et al., 2008] Meadowcroft, A. L., Bentley, C. D., and Stott, E. N. (2008). Evaluation of the sensitivity and fading characteristics of an image plate system for x-ray diagnostics. *Review of Scientific Instruments*, 79(11):113102.
- [Metzkes et al., 2011] Metzkes, J., Cowan, T., Karsch, L., Kraft, S., Pawelke, J., Richter, C., Richter, T., Zeil, K., and Schramm, U. (2011). Preparation of laser-accelerated proton beams for radiobiological applications. *Nuclear Instruments and Methods in Physics Research Section A: Accelerators, Spectrometers, Detectors and Associated Equipment*, 653(1):172 – 175.
- [Metzkes et al., 2012] Metzkes, J., Karsch, L., Kraft, S. D., Pawelke, J., Richter, C., Schürer, M., Sobiella, M., Stiller, N., Zeil, K., and Schramm, U. (2012). A scintillator-based online detector for the angularly resolved measurement of laser-accelerated proton spectra. *Review of Scientific Instruments*, 83(12):–.
- [Mora, 2003] Mora, P. (2003). Plasma expansion into a vacuum. *Phys. Rev. Lett.*, 90:185002.
- [Mora, 2005] Mora, P. (2005). Thin-foil expansion into a vacuum. *Phys. Rev. E*, 72:056401.
- [Mori et al., 2006] Mori, M., Kando, M., Pirozhkov, A. S., Hayashi, Y., Yogo, A., Yoshimura, N., Ogura, K., Nishiuchi, M., Sagisaka, A., Orimo, S., Kado, M., Fukumi, A., Li, Z., Nakamura, S., Noda, A., and Daido, H. (2006). New detection device for thomson parabola spectrometer for diagnosis of the laser-plasma ion beam. *Plasma and Fusion Research*, 1:042–042.
- [Mulser and Bauer, 2010] Mulser, P. and Bauer, D. (2010). *High Power Laser-Matter Interaction*. Springer.
- [Murakami and Tanaka, 2013] Murakami, M. and Tanaka, M. (2013). Generation of high-quality mega-electron volt proton beams with intense-laser-driven nanotube accelerator. *Applied Physics Letters*, 102(16):–.
- [Nemoto et al., 2001] Nemoto, K., Maksimchuk, A., Banerjee, S., Flippo, K., Mourou, G., Umstadter, D., and Bychenkov, V. Y. (2001). Laser-triggered ion acceleration and table top isotope production. *Applied Physics Letters*, 78(5):595–597.
- [Nishiuchi et al., 2009] Nishiuchi, M., Daito, I., Ikegami, M., Daido, H., Mori, M., Orimo, S., Ogura, K., Sagisaka, A., Yogo, A., Pirozhkov, A. S., Sugiyama, H., Kiriya, H., Okada, H., Kanazawa, S., Kondo, S., Shimomura, T., Tanoue, M., Nakai, Y., Sasao, H., Wakai, D., Sakaki, H., Bolton, P., Choi, I. W., Sung, J. H., Lee, J., Oishi, Y., Fujii, T., Nemoto, K., Souda, H., Noda, A., Iseki, Y., and Yoshiyuki, T. (2009). Focusing and spectral enhancement of a repetition-rated, laser-driven, divergent multi-mev proton beam using permanent quadrupole magnets. *Applied Physics Letters*, 94(6):061107.
- [Nürnberg, 2010] Nürnberg, F. (2010). *Laser-Accelerated Proton Beams as a New Particle Source*. PhD thesis, TU Darmstadt.
- [Nürnberg et al., 2009] Nürnberg, F., Schollmeier, M., Brambrink, E., Blazevic, A., Carroll, D. C., Flippo, K., Gautier, D. C., Geissel, M., Harres, K., Hegelich, B. M., Lundh, O., Markey, K., McKenna, P., Neely, D., Schreiber, J., and Roth, M. (2009). Radiochromic film imaging spectroscopy of laser-accelerated proton beams. *Review of Scientific Instruments*, 80(3):033301.

-
- [Otten, 2007] Otten, A. (2007). Modellierung des ausleseprozesses von cr-bildplatten. Master's thesis, TU Darmstadt.
- [Palmer et al., 2011] Palmer, C. A. J., Dover, N. P., Pogorelsky, I., Babzien, M., Dudnikova, G. I., Ispiriyan, M., Polyanskiy, M. N., Schreiber, J., Shkolnikov, P., Yakimenko, V., and Najmudin, Z. (2011). Monoenergetic proton beams accelerated by a radiation pressure driven shock. *Phys. Rev. Lett.*, 106(1):014801.
- [Passoni et al., 2010] Passoni, M., Bertagna, L., and Zani, A. (2010). Target normal sheath acceleration: theory, comparison with experiments and future perspectives. *New Journal of Physics*, 12(4):045012.
- [Passoni and Lontano, 2004] Passoni, M. and Lontano, M. (2004). One-dimensional model of the electrostatic ion acceleration in the ultraintense laser-solid interaction. *Laser and Particle Beams*, 22:163–169.
- [Patel et al., 2003] Patel, P. K., Mackinnon, A. J., Key, M. H., Cowan, T. E., Foord, M. E., Allen, M., Price, D. F., Ruhl, H., Springer, P. T., and Stephens, R. (2003). Isochoric heating of solid-density matter with an ultrafast proton beam. *Phys. Rev. Lett.*, 91:125004.
- [Pelka et al., 2010] Pelka, A., Gregori, G., Gericke, D. O., Vorberger, J., Glenzer, S. H., Günther, M. M., Harres, K., Heathcote, R., Kritcher, A. L., Kugland, N. L., Li, B., Makita, M., Mithen, J., Neely, D., Niemann, C., Otten, A., Riley, D., Schaumann, G., Schollmeier, M., Tauschwitz, A., and Roth, M. (2010). Ultrafast melting of carbon induced by intense proton beams. *Phys. Rev. Lett.*, 105(26):265701.
- [Perego et al., 2011] Perego, C., Zani, A., Batani, D., and Passoni, M. (2011). Extensive comparison among target normal sheath acceleration theoretical models. *Nuclear Instruments and Methods in Physics Research Section A: Accelerators, Spectrometers, Detectors and Associated Equipment*, 653(1):89–93.
- [Reiser, 2008] Reiser, M. (2008). *Theory and Design of Charged Particle Beams, Second Edition*. WILEY-VCH Verlag.
- [Rödel et al., 2011] Rödel, C., Heyer, M., Behmke, M., Kübel, M., Jäckel, O., Ziegler, W., Ehrt, D., Kaluza, M., and Paulus, G. (2011). High repetition rate plasma mirror for temporal contrast enhancement of terawatt femtosecond laser pulses by three orders of magnitude. *Applied Physics B*, 103(2):295–302.
- [Romagnani et al., 2005] Romagnani, L., Fuchs, J., Borghesi, M., Antici, P., Audebert, P., Ceccherini, F., Cowan, T., Grismayer, T., Kar, S., Macchi, A., Mora, P., Pretzler, G., Schiavi, A., Toncian, T., and Willi, O. (2005). Dynamics of electric fields driving the laser acceleration of multi-mev protons. *Phys. Rev. Lett.*, 95:195001.
- [Roth et al., 2005] Roth, M., Blazevic, A., Brambrink, E., Geissel, M., Cowan, T., Fuchs, J., Kemp, A., Ruhl, H., Audebert, P., Cobble, J., Fernandez, J., Hegelich, M., Letzring, S., Ledingham, K., McKenna, P., Clarke, R., Neely, D., Karsch, S., Habs, D., and Schreiber, J. (2005). Laser accelerated, high quality ion beams. *Hyperfine Interactions*, 162:45–53. 10.1007/s10751-005-9202-4.
- [Roth et al., 2001] Roth, M., Cowan, T. E., Key, M. H., Hatchett, S. P., Brown, C., Fountain, W., Johnson, J., Pennington, D. M., Snavely, R. A., Wilks, S. C., Yasuike, K., Ruhl, H., Pegoraro, F., Bulanov, S. V., Campbell, E. M., Perry, M. D., and Powell, H. (2001). Fast ignition by intense laser-accelerated proton beams. *Phys. Rev. Lett.*, 86(3):436–439.
- [Roth et al., 2013] Roth, M., Jung, D., Falk, K., Guler, N., Deppert, O., Devlin, M., Favalli, A., Fernandez, J., Gautier, D., Geissel, M., Haight, R., Hamilton, C. E., Hegelich, B. M., Johnson, R. P., Merrill, F., Schaumann, G., Schoenberg, K., Schollmeier, M., Shimada, T., Taddeucci, T., Tybo, J. L., Wagner, F., Wender, S. A., Wilde, C. H., and Wurden, G. A. (2013). Bright laser-driven neutron source based on the relativistic transparency of solids. *Phys. Rev. Lett.*, 110:044802.

-
- [Ruhl et al., 2006] Ruhl, H., Cowan, T., and Pegoraro, F. (2006). The generation of images of surface structures by laser-accelerated protons. *Laser and Particle Beams*, 24(01):181–184.
- [Schaumann et al., 2005] Schaumann, G., SCHOLLMIEIER, M., RODRIGUEZ-PRIETO, G., BLAZEVIC, A., BRAMBRINK, E., GEISSEL, M., KOROSTIY, S., PIRZADEH, P., ROTH, M., ROSMEJ, F., FAENOV, A., PIKUZ, T., TSIGUTKIN, K., MARON, Y., TAHIR, N., and HOFFMANN, D. (2005). High energy heavy ion jets emerging from laser plasma generated by long pulse laser beams from the nhelix laser system at gsi. *Laser and Particle Beams*, 23:503–512.
- [Schollmeier, 2008] Schollmeier, M. (2008). *Optimization and control of laser-accelerated proton beams*. PhD thesis, TU Darmstadt.
- [Schollmeier et al., 2008] Schollmeier, M., Becker, S., Geißel, M., Flippo, K. A., Blažević, A., Gaillard, S. A., Gautier, D. C., Grüner, F., Harres, K., Kimmel, M., Nürnberg, F., Rambo, P., Schramm, U., Schreiber, J., Schüttrumpf, J., Schwarz, J., Tahir, N. A., Atherton, B., Habs, D., Hegelich, B. M., and Roth, M. (2008). Controlled transport and focusing of laser-accelerated protons with miniature magnetic devices. *Phys. Rev. Lett.*, 101(5):055004.
- [Schreiber, 2012] Schreiber, A. (2012). Rgb-kalibrierung von radiochromatischen filmen. Bachelor thesis.
- [Schreiber, 2006] Schreiber, J. (2006). *Ion Acceleration driven by High-Intensity Laser Pulses*. PhD thesis, LMU München.
- [Schwoerer et al., 2006] Schwoerer, H., Pfoth, S., Jackel, O., Amthor, K.-U., Liesfeld, B., Ziegler, W., Sauerbrey, R., Ledingham, K. W. D., and Esirkepov, T. (2006). Laser-plasma acceleration of quasi-monoenergetic protons from microstructured targets. *Nature*, 439(7075):445–448.
- [Scott et al., 2012] Scott, G. G., Green, J. S., Bagnoud, V., Brabetz, C., Brenner, C. M., Carroll, D. C., MacLellan, D. A., Robinson, A. P. L., Roth, M., Spindloe, C., Wagner, F., Zielbauer, B., McKenna, P., and Neely, D. (2012). Multi-pulse enhanced laser ion acceleration using plasma half cavity targets. *Applied Physics Letters*, 101(2):–.
- [Sinigardi et al., 2013] Sinigardi, S., Turchetti, G., Londrillo, P., Rossi, F., Giove, D., De Martinis, C., and Sumini, M. (2013). Transport and energy selection of laser generated protons for postacceleration with a compact linac. *Phys. Rev. ST Accel. Beams*, 16:031301.
- [Snavely et al., 2000] Snavely, R. A., Key, M. H., Hatchett, S. P., Cowan, T. E., Roth, M., Phillips, T. W., Stoyer, M. A., Henry, E. A., Sangster, T. C., Singh, M. S., Wilks, S. C., MacKinnon, A., Offenberger, A., Pennington, D. M., Yasuike, K., Langdon, A. B., Lasinski, B. F., Johnson, J., Perry, M. D., and Campbell, E. M. (2000). Intense high-energy proton beams from petawatt-laser irradiation of solids. *Phys. Rev. Lett.*, 85(14):2945–2948.
- [Snavely et al., 2007] Snavely, R. A., Zhang, B., Akli, K., Chen, Z., Freeman, R. R., Gu, P., Hatchett, S. P., Hey, D., Hill, J., Key, M. H., Izawa, Y., King, J., Kitagawa, Y., Kodama, R., Langdon, A. B., Lasinski, B. F., Lei, A., MacKinnon, A. J., Patel, P., Stephens, R., Tampo, M., Tanaka, K. A., Town, R., Toyama, Y., Tsutsumi, T., Wilks, S. C., Yabuuchi, T., and Zheng, J. (2007). Laser generated proton beam focusing and high temperature isochoric heating of solid matter. *Physics of Plasmas*, 14(9):092703.
- [Strickland and Mourou, 1985] Strickland, D. and Mourou, G. (1985). Compression of amplified chirped optical pulses. *Optics Communications*, 56(3):219 – 221.
- [Tajima and Dawson, 1979] Tajima, T. and Dawson, J. M. (1979). Laser electron accelerator. *Phys. Rev. Lett.*, 43:267–270.

-
- [Tampo et al., 2010] Tampo, M., Awano, S., Bolton, P. R., Kondo, K., Mima, K., Mori, Y., Nakamura, H., Nakatsutsumi, M., Stephens, R. B., Tanaka, K. A., Tanimoto, T., Yabuuchi, T., and Kodama, R. (2010). Correlation between laser accelerated mev proton and electron beams using simple fluid model for target normal sheath acceleration. *Physics of Plasmas*, 17(7):073110.
- [Teng et al., 2013] Teng, J., Gu, Y., Zhu, B., Hong, W., Zhao, Z., Zhou, W., and Cao, L. (2013). Beam collimation and energy spectrum compression of laser-accelerated proton beams using solenoid field and {RF} cavity. *Nuclear Instruments and Methods in Physics Research Section A: Accelerators, Spectrometers, Detectors and Associated Equipment*, 729(0):399 – 403.
- [Toncian et al., 2006] Toncian, T., Borghesi, M., Fuchs, J., d’Humières, E., Antici, P., Audebert, P., Brambrink, E., Cecchetti, C. A., Pipahl, A., Romagnani, L., and Willi, O. (2006). Ultrafast laser-driven microlens to focus and energy-select mega-electron volt protons. *Science*, 312(5772):410–413.
- [Wagner et al., 2013] Wagner, F., Joao, C., Fils, J., Gottschall, T., Hein, J., Körner, J., Limpert, J., Roth, M., Stöhlker, T., and Bagnoud, V. (2013). Temporal contrast control at the phelix petawatt laser facility by means of tunable sub-picosecond optical parametric amplification. *Applied Physics B*, pages 1–7.
- [Wilks et al., 1992] Wilks, S. C., Kruer, W. L., Tabak, M., and Langdon, A. B. (1992). Absorption of ultra-intense laser pulses. *Phys. Rev. Lett.*, 69:1383–1386.
- [Wilks et al., 2001] Wilks, S. C., Langdon, A. B., Cowan, T. E., Roth, M., Singh, M., Hatchett, S., Key, M. H., Pennington, D., MacKinnon, A., and Snavely, R. A. (2001). Energetic proton generation in ultra-intense laser–solid interactions. *Physics of Plasmas*, 8(2):542–549.
- [Wille, 1996] Wille, K. (1996). *Physik der Teilchenbeschleuniger und Synchrotronstrahlungsquellen, 2., überarbeitete und erweiterte Auflage*. B. G. Teubner.
- [Yin et al., 2011] Yin, L., Albright, B. J., Bowers, K. J., Jung, D., Fernández, J. C., and Hegelich, B. M. (2011). Three-dimensional dynamics of breakout afterburner ion acceleration using high-contrast short-pulse laser and nanoscale targets. *Phys. Rev. Lett.*, 107:045003.
- [Yin et al., 2006] Yin, L., Albright, B. J., Hegelich, B. M., and Fernandez, J. C. (2006). GeV laser ion acceleration from ultrathin targets: The laser break-out afterburner. *Laser and Particle Beams*, 24(02):291–298.
- [Yogo et al., 2007] Yogo, A., Daido, H., Fukumi, A., Li, Z., Ogura, K., Sagisaka, A., Pirozhkov, A. S., Nakamura, S., Iwashita, Y., Shirai, T., Noda, A., Oishi, Y., Nayuki, T., Fujii, T., Nemoto, K., Woo Choi, I., Hee Sung, J., Ko, D.-K., Lee, J., Kaneda, M., and Itoh, A. (2007). Laser prepulse dependency of proton-energy distributions in ultraintense laser-foil interactions with an online time-of-flight technique. *Physics of Plasmas (1994-present)*, 14(4):–.
- [Ziegler, 2013] Ziegler, J. F. (2013). Srim, <http://www.srim.org>.

II Publications

The results of this PhD thesis lead to several publications and numerous contributions to conferences, workshops and works as well as publications of others. A list of published articles and given talks is itemized below.

First author publications (reviewed):

- S. Busold *et al.*, *Focusing and transport of high-intensity multi-MeV proton bunches from a compact laser-driven source*, PR-STAB **16**, 101302 (2013)
- S. Busold *et al.*, *Shaping laser accelerated ions for future applications - The LIGHT collaboration*, NIM-A **740**, 94-98 (2014)
- S. Busold *et al.*, *Commissioning of a compact laser-based proton beamline for high intensity bunches around 10MeV*, PR-STAB **17**, 031302 (2014)

First author publications (non-reviewed):

- S. Busold *et al.*, *Laser proton acceleration as compact ion source*, proceedings of 2011 Particle Accelerator Conference, New York, NY, USA
- S. Busold *et al.*, *Investigation of co-moving electrons in laser ion acceleration experiments with a magnetic electron spectrometer*, GSI scientific report 2010, GSI Darmstadt (2011)
- S. Busold *et al.*, *First experiments with the new PHELIX 100 TW beamline: Towards new applications for laser ion sources*, GSI scientific report 2011, GSI Darmstadt (2012)
- S. Busold *et al.*, *Transport and focusing of laser-accelerated protons at Z6*, GSI scientific report 2012, GSI Darmstadt (2013)
- S. Busold *et al.*, *A laser-driven proton beamline at GSI*, GSI scientific report 2013, GSI Darmstadt (-)

Co-author publications (reviewed):

- T. Burris-Mog *et al.*, *Laser accelerated protons captured and transported by a pulse power solenoid*, PR-STAB **14**, 121301 (2011)
- J. Prokupek *et al.*, *Development and First Experimental Tests of Faraday cup array*, RSI **85**, 013302 (2014)

Talks:

- 32nd International Workshop on Physics of High Energy Density in Matter, 29 January - 3 February 2012, Hirschegg, Austria
- Helmholtz center Dresden-Rossendorf (seminar talk), 9 February 2012, Dresden-Rossendorf, Germany
- DPG Frühjahrstagung, 12-16 March 2012, Stuttgart, Germany

-
- 44. Arbeitstreffen Kernphysik, 21-28 February 2013, Schleching, Germany
 - DPG Frühjahrstagung, 4-8 March 2013, Dresden, Germany
 - 1st European Advanced Accelerator Concepts Workshop, 2-7 June 2013, La Biodola, Isola d'Elba, Italy
 - EMMI workshop on high energy density plasma diagnostics at FAIR: novel laser based photon and particle sources, 30 September - 2 October 2013, GSI Darmstadt, Germany
 - 11th Microbeam Workshop, 3-4 October 2013, Bordeaux, France
 - GSI Helmholtz center for heavy ion research (seminar talk), 5 November 2013, Darmstadt, Germany

III Acknowledgments

This work would not have been possible without the support and contribution of many other people.

- First I want to thank my supervisor Markus Roth, who gave me the possibility to work on this exciting field within his research group and always supported and valued my efforts.
- Also, I want to thank my second supervisor, Oliver Boine-Frankenheim, and others from the scientific staff - especially Abel Blazevic, Ingo Hofmann, Bernhard Zielbauer and Vincent Bagnoud - who were always available for helpful discussions and good advice.
- Many thanks also to the two working groups, the laser and plasma physics group of TU Darmstadt and the plasma physics group of GSI, that I had the pleasure to be part of during my time as a PhD student (and also during my Master's thesis).
- Very special thanks I owe to my co-workers Dennis Schumacher, Oliver Deppert and Christian Brabetz. They also represented the core experimental team during the campaigns that contributed to this thesis. We worked together during several experimental campaigns, discussed our results, improved our detection and analysis methods and all in all spent a lot of time together in always a great and supportive atmosphere.
- Besides the dominating experimental part of my work, debating the underlying theoretical principles has never come too short. In this context, much credit has to be given to Peter Mulser, who patiently discussed with us our physics on the theoretical levels in regular meetings, which represent an established place for discussions today.
- Nearly all experimental campaigns within this thesis were performed at the PHELIX laser. The operating crew of PHELIX has always been great to work with and I want to thank for their continuous commitment to our experiments during the last years.
- Furthermore, the accelerator and HF department of GSI were substantially contributing through their help on the characterization of the cavity, the installation of the rf infrastructure and the operation during the experimental campaign.
- Similarly essential is the presence of a scientific-technical infrastructure in general. Many a time the machine shops and target laboratories at GSI and TU Darmstadt provided the necessary components and targets for the experiments.
- A central part of the LIGHT beamline, the solenoid and pulsed power equipment, was provided by our collaborators from HZDR. Many thanks for their contribution, too; especially for the continuous support in man power before and during the experiments, provided by Trevor Burris-Mog, Martin Joost and Florian Kroll.
- In general, I want to thank all the LIGHT collaborators for their support whenever necessary and their ongoing commitment to the project.

-
- Finally, my last three and a half years haven't only been work on my PhD. I am grateful for all the support and positive distraction that I could always find with my family, my friends and especially my beloved companion in life, Steffi.

Curriculum vitae

Personal

Name	Simon Busold
Date of birth	01 March 1985
Place of birth	Fulda, Germany
Nationality	German

Education

since 11/2010	PhD at Technical University Darmstadt (HGS-HiRe stipendship) title: <i>Construction and characterization of a laser-driven proton beamline at GSI</i>
09/2010	MSc at Technical University Darmstadt title: <i>Construction and application of a magnetic spectrometer for investigation of low energy electrons [1...30 keV] in laser-proton-acceleration experiments</i>
09/2008	BSc at Technical University Darmstadt title: <i>Investigation of ^1H-NMR spin-lattice relaxation of benzene in zeolite-NaX</i>
07/2004	university-entrance diploma at Wigbergtschule Hünfeld

Work

10/2004	civilian service at <i>caritas</i> , Fulda
2010-2012	student assistant at TU Darmstadt

Languages

German	mother tongue
English	fluent



Erklärung zur Dissertation

Hiermit versichere ich, die vorliegende Dissertation ohne Hilfe Dritter nur mit den angegebenen Quellen und Hilfsmitteln angefertigt zu haben. Alle Stellen, die aus Quellen entnommen wurden, sind als solche kenntlich gemacht. Diese Arbeit hat in gleicher oder ähnlicher Form noch keiner Prüfungsbehörde vorgelegen.

Darmstadt, den May 12, 2014

(S. Busold)
